NUMERICAL AND EXPERIMENT STUDIES ON CONVECTIVE PHENOMENA IN MATERIALS PROCESSING SYSTEMS

By

BING XU

A dissertation submitted in partial fulfillment of
the requirements for the degree of

DOCTOR OF PHILOSOPHY
(Mechanical Engineering)

WASHINGTON STATE UNIVERSITY
The School of Mechanical and Materials Engineering

DECEMBER 2005

To the Faculty of Washington State University:

The members of the Committee appointed to examine the dissertation of BING XU find it satisfactory and recommend that it be accepted.

_____
Chair

_____

_____

_____

ACKNOWLEDGMENTS

I would like to express my gratitude to my advisor, Dr. Ben Q. Li, for his continuous support, patience, and encouragement during the course of this work. His advice was essential to the completion of this dissertation. My thanks go to my committee members, Dr. David Stock, Dr. David Wollkind, and Dr. Hong-Ming Yin. Their valuable suggestions have led to significant improvement of this dissertation.

I am fortunate to have the opportunity to work with a group of energetic and knowledgeable people at Dr. Li's Lab. Their friendship is much appreciated and has led to many interesting and good-spirited discussions relating to this research. I am also grateful to Mr. Robert Lentz for helping with experimental setup.

Financial supports of this work from US National Aeronautics and Space Administration (Grant #: NAG8-NNM04AA17G) and US Department of Energy (Grant #: DEFC3601ID14189) are gratefully acknowledged.

I would like to thank my wife, MengMeng, for her understanding and love. My parents receive my deepest gratitude and love. Their support and encouragement were in the end what made this dissertation possible. This dissertation is dedicated to my parents.

NUMERICAL AND EXPERIMENT STUDIES ON CONVECTIVE PHENOMENA IN MATERIALS PROCESSING SYSTEMS

Abstract

by Bing Xu, Ph.D.
Washington State University
December 2005

Chair: Ben Q. Li

A fundamental study on convective transportation phenomena in material processing systems is presented. The study is focused on two aspects of the convection, Rayleigh-Bénard-Marangoni instability of convective flow in Czochralski crucibles and magnetic damping of natural convection in rectangular boxes.

Changes in melt flow patterns, such as transition from steady state flow to time dependent flow and breaking up from axisymmetric base flow, have a strong effect on the crystal structure. A linear stability analysis of the convective flow in Czochralski crystal growth systems is carried out to investigate the changes in the flow patterns. A numerical model of the melts flow in the Czochralski crucible is developed using high order finite difference method. The stability analysis is based on the solution of linearized governing equations in a cylindrical coordinates system. The perturbation equations are discretized using the high order finite difference scheme and the resulting eigenvalue problem is solved by linear fractional transformation. Both radiation participating and non-participating fluids are considered in the stability analysis to reveal how the internal

radiation may affect the stability of the melt flow. The radiative transfer equation is solved using discontinuous finite element method. The discontinuous finite element model is coupled with the high order finite difference model via the heat source term resulting from the internal radiation. The results suggest that the internal radiation changes the temperature field and therefore the convective flow structure significantly.

The damping effect of a magnetic field on the thermally-induced convection in a rectangular box is investigated experimentally using molten gallium as working fluid. The velocity and temperature fields are measured using constant-temperature hot-film anemometry and a thermocouple. The hot-film anemometer is calibrated over a narrow temperature range using a rotating container filled with gallium following the technique outlined by Sajben. The velocity and temperature profiles are measured with and without the magnetic field. Numerical simulations are also performed and found to be in good agreement with the experimental results. The damping effect of the magnetic field occurs in both the temperature and the velocity profiles and increases as the strength of the magnetic field is increased.

TABLE OF CONTENTS

LIST OF TABLES

LIST OF FIGURES

NOMENCLATURE

A	aspect ratio
B	strength of magnetic field
Bi	Biot number
c_p	specific heat
d	diameter of the hot-film probe
E	anemometer bridge output
f	body force
Gr	Grashof number
F	force matrix
g	gravity acceleration
H	height of crucible
h	heat transfer coefficient
I	radiative intensity
K	stiffness matrix
L	length of the hot-film probe
M	Mach number
Ma	Marangoni number
m	azimuthal wave number
n	out normal of boundary

Pe	Péclet number
Pr	Prandtl number
p	pressure
Q	volumetric heat source
	Heat dissipation from the hot-film probe
q	heat flux
R	cylinder radius
	resistance
r	position vector
R_d	seeding crystal radius
Ra	Rayleigh number
Rad	radiation number
Re_γ	Marangoni Reynolds number
s	direction vector
T	temperature
T_{amb}	ambient temperature
T_d	temperature of seeding crystal
T_m	reference temperature
t	time
U	velocity component
u	velocity vector

Greek letters

α	thermal diffusivity
β	thermal expansion coefficient
	extinction coefficient
γ	negative rate of change of surface tension with temperature
δ	Stefan-Boltzmann constant
ε	emissivity
θ	azimuthal angle
σ	surface tension
	scattering coefficient
σ_s	Stefan-Boltzmann constant
ϕ	shape function
φ	polar angle
κ	thermal conductivity
	absorption coefficient
μ	viscosity
v	kinematic viscosity
ρ	density
Ω	radiation control angle
ω	complex wave speed

Subscriptions

amb	ambient
c	conduction

d	seeding crystal
P	probe
r	r direction
	radiation
T	total
ref	reference state
w	wall
z	z direction
θ	θ direction

CHAPTER ONE

INTRODUCTION

1.1 Background

Due to the fast development in electronic industrial over the past several decades, significant research interests and efforts have been drawn to the design of advanced material processing systems for high quality crystals with high level of solute uniformity. It is reported that over 80 percent of the commercially available crystal materials are grown from molten state [Pimputkar and Ostrach, 1981]. The solidification process is inevitably associated with certain temperature gradient that may induce convective flow in melt pool. Previous studies have shown that the combined effects of the imposed temperature gradient and gravity result in improper convective flow patterns, which causes macroscopic structural defects, known as segregations or striations, in the solid crystals produced [Fleming, 1974; Tiller, 1991; Langlois, 1985; Glicksman *et al*., 1986]. During the solidification process, the bulk convective flow changes the microscopic flow, heat and/or mass transfer within the dendritic structures near the solidification front significantly. This gives rise to unsteady temperature distributions in the molten zone, which causes striation and non-homogeneity in the crystal produced [Hamacher *et al.* 1987; Nelson, 1994; Pimputkar and Ostrach, 1981; Coriell and Sekerka, 1981]. Figure 1.1 shows the inhomogeneous distribution of "swirl" defects, which occur in both Czochralski (CZ) and float-zone (FZ) crystal growth systems irrespective of their crystallographic orientation. Therefore, development of effective convection control

mechanism is desirable in efforts to produce high quality crystal under either terrestrial or microgravity environment. Deep insights of the physics underlying the convective flow in material processing systems are crucial in the development of the convection damping mechanism.

1.2 Literature Review

Convection is one of the most omnipresent phenomena in engineering practice. It may be driven by several mechanisms such as, buoyancy, surface tension, electromagnetic force, etc. In material processing systems, the melt is subjected to certain temperature gradients. The temperature differences cause density gradients in the melts, and hence results in convective flow. The buoyancy-driven convection practically presents in every crystal growth system in terrestrial condition. Another important convection driving force is surface tension. It is well known that surface tension of liquid is a function of fluid temperature. When free surface of the melt is subjected to temperature gradient, convective flow is driven from high temperature to low temperature. The surface tension is the dominating driven force of convective flow in microgravity or thin layers of liquid. A Czochralski crystal growth system is shown schematically in Figure 1.2. In this system, the melt is heated by the RF coil through the vertical wall. The crystal is pulled from the melt pool slowly and the melt is cooled at the solid-liquid interface. The free surface between the solid-liquid interface and the crucible wall is cooled by the ambient air. The convection may be driven by either the buoyancy due to the density gradient caused by the laterally heating or the surface tension gradient due to the temperature gradient along the free surface. A recent review of the convection in the crystal growth melt was given by Schwabe [1988].

The ever-growing demands for high quality crystal materials have resulted in substantial research focused on understanding and eventually controlling the convection in the material processing systems.

1.2.1 Rayleigh-Bénard instability

Stability of natural convection has been a classic topic of fluid mechanics. Systematic investigation of the topic began in the early last century with the experiment of Bénard [1900], who observed the formation of convective cells in a horizontal layer of fluid heated from below, Figure 1.3. Rayleigh was the first one studied the stability of equilibrium in a horizontal layer of fluid theoretically and determined the threshold point for the natural convection [Rayleigh, 1916]. Though later shown by Block [1956] and Pearson [1958] that the convective cells observed by Bénard were driven by variation of surface tension, Rayleigh's model is in accord with experiments on thicker layers of fluid with rigid boundaries [Drazin and Reid, 1981]. Since then, extensive studies have been carried out on convective stability due to various factors, such as, magnetic field, rotation, diffusion, penetration of permeable boundaries, surface tension, etc. Several reviews on the stability of the convective flow are available [Chandrasekhar, 1961; Gershuni and Zhukhovitskii, 1976; Drazin and Reid, 1981; Koschmieder, 1993].

Most of the previous studies were concerned with liquid layers with infinite horizontal extent. Investigations on thermal convection in laterally bounded layer of fluid are relatively rare due to the complexity introduced by the sidewall effects. For vertical cylinders heated from below, Charlson and Sani [1970a, 1970b], Stork and Müller [1975], Rosenblat [1982], Buell and Catton [1983] and Rubinov *et al.*, [2004] have shown that the critical Rayleigh number depends on aspect ratio (height/diameter)

of the cylinder. The most dangerous azimuthal wave number varies between 0 and 1 when aspect ratio (height/diameter) is between 0.55 and 0.72.

Three-dimensional numerical simulations of the natural convection in cylindrical configuration were conducted by Neumann [1990] and Wanschura *et al*. [1996]. They found that the convective flow pattern beyond the critical points is related to the disturbance applied to the initial static condition. Touihri *et al.* [1999] carried out 3-D simulation of steady convective flow in a vertical cylinder heated from below. Both axisymmetric and non-axisymmetric flow pattern were observed in their simulations.

1.2.2 Marangoni instability

In terrestrial environment, both Rayleigh-Bénard effect and the Marangoni effect present and often the Marangoni convection is overshadowed by the Rayleigh-Bénard convection. However, for thin layers of fluid or in microgravity environment, the thermocapillary effect dominates the flow. First stability analysis of surface tension driven flow was conduct by Pearson [1958]. Since then, numerous efforts have been made to understand the Marangoni convection. Reviews on the topic can be found by Levich and Krylov [1969], Davis [1987], and Schatz and Neitzel [2001]. When the applied temperature gradient is perpendicular to the free surface, and is small enough, a pure conducting basic state is possible. The convective flow sets in when the applied temperature gradient exceeds certain threshold. When the temperature gradient is imposed parallel to the free surface, the convective flow occurs at any value of the temperature gradient and no static base flow is possible. However, when the temperature gradient is small enough, the induced convection is either one- or two-dimensional and at certain threshold the flow becomes three-dimensional [Schatz and Neitzel, 2001].

Same as those for Rayleigh-Bénard convection, most of the previous investigations were focused on thermocapillary convection in liquid layers with infinite horizontal extent. Previous studies on thermocapillary convection in laterally bounded fluid layer are limited. For flow layers with free surface in rectangular cavities, stability analyses are given by Peltier and Biringen [1993], Sab *et al.*, [1996], and Xu and Zebib [1998].

In cylindrical configurations, Vrentas *et al.* [1981] investigated the stabilities convective flow driven only by buoyant or thermal-capillary effects. Critical Rayleigh numbers and Marangoni numbers are reported for various aspect ratios using a fluid with infinite Prandtl number.

Wagner *et al.* [1994] conducted 3-D numerical simulations of natural convection in an open vertical cylinder with various boundary conditions imposed at the top surface. Both 2-D and 3-D perturbations were applied to the flow. They have shown that axisymmetric perturbation may lead to non-axisymmetric 3-D flow.

Dauby *et al*. [1997] presented a linear stability analysis of coupled Bénard-Marangoni convection in a vertical cylinder. They have presented results over a wide range of aspect ratio and found that conducting lateral walls are more stable than insulating boundaries.

For thermocapillary convection driven by horizontal temperature gradient, extensive experimental observations have been reported [Schwabe, *et al.*, 1992; Ezersky, *et al.*, 1993; Favre *et al.*, 1997; Garnier and Chiffaudel, 2001]. Hoyas *et al.* [2002] studied the stability of large Prandtl number fluid contained in a laterally heated

cylindrical annulus. Two base flow patterns, co-rotating rolls and return flow pattern, were observed in their results.

1.2.3 Internal radiation

In most of the previous investigations on convective heat transfer, it is a common practice that the contribution of thermal radiation is neglected, in other words, the fluid is assumed transparent to radiative energy transfer. However, there are many engineering applications in which the radiation can significantly interacts with the convection and change the heat transfer mechanism [Siegel and Howell, 1992; Modest, 1993]. In materials processing systems, the fact that the melt is absorbing, emitting and scattering in thermal radiation frequency range makes it important to understand the interaction between the convective heat transfer and the thermal radiation [Shu *et al.*, 2004]. The changes in thermal field caused by the radiation may change the convective flow field and furthermore, change the crystal structure of the materials produced.

Several previous works are found on the problem of combined radiation and convection [Larson, 1981; Chang *et al.*, 1983; Desreyaud and Lauriat, 1985; Webb and Viskanta, 1987]. A review on this problem is given by Yang [1986].

More recently, Tan and Howell [1991] presented a numerical study on combined thermal radiation and convection in a square enclosure. The radiative transport equation is discretized using product-integral method while the equations of momentum and energy conservations are discretized using finite difference method. Simulations were carried out at various Rayleigh numbers. It was found that the presence of internal radiation changes the temperature and flow fields significantly.

Kassemi and Naraghi [1993] investigated the combined radiation and convection in a square box in both terrestrial and microgravity environment using discrete exchange factor method. Their results have shown that the radiation significantly changes the flow and temperature fields in both terrestrial and microgravity applications. In microgravity environment, convection is weak and radiation can easily become the dominant heat transfer mode.

The effect of internal radiation on oxide melts was discussed by Tsukada *et al.*, [1995]. The P-1 method was used to approximate the radiative heat transfer. They also found that the flow and temperature fields are strongly affected by internal radiation. The solid-liquid interface shape becomes more convex to the melt as the optical absorption coefficients of both the crystal and the melt decreases.

A numerical model for transport and solidification phenomena in oxide melts with and without the presence of an applied magnetic field was proposed by Shu *et al.* [2004]. The model is base finite element solution of Navier-Stokes equations with the induced Lorentz force serving as the damping source. The radiative transfer equation was solved by discontinuous finite-element method. Their results suggested that the internal radiation have significant effect on solidification behavior.

1.2.4 Magnetic damping

Since the convective flow is the major cause of some macroscopic defects in the crystal produced, it is desirable to remove this deleterious flow. The ultimate goal of all the efforts made on the convection in material processing systems is to control the flow. One of the effective means practiced in industry for thermally-induced melt flow control is magnetic damping, which derived from the interaction between an electrically

conducting melt flow and an applied magnetic field to generate a Lorentz force to damp the convective flow in the melt. The damping effect depends on the strength of the applied magnetic field and its orientation with respect to the convective flow direction. Substantial theoretical and numerical work thus far has appeared on magnetic damping for natural convection as reviewed by Hunt and Shercliff [1971] and Moreau [1990].

Ozoe and Okada [1989] investigated the magnetic damping effect in a cubic cavity with two vertical opposite walls holding at different temperatures numerically. They found that the strongest damping effect is achieved with the magnetic field applied perpendicular to the hot wall.

Their results are consistent with the work of Alboussière *et al.* [1996] who used an asymptotic approach to investigate the magnetic damping effect, and found that for a rectangular box the damping effect is the weakest when the applied magnetic field is horizontal and parallel to the hot wall.

BenHadid and Henry [1997] studied the damping of steady convection induced by temperature gradients using a $4 \times 1 \times 1$ cavity with the magnetic field applied in different directions. Their results are in good agreement with the analytical predictions from Alboussière *et al.* [1996] and Garandet *et al.* [1992].

Recent research on the subject has been on exploring the possibility of applying magnetic damping concept to control the g-jitter induced natural convection in microgravity environment [Baumgartl and Müller, 1996; Ma and Walker, 1996; Pan *et al.*, 2002; Shu *et al.*, 2002].

1.2.5 Measurement of melt flow

Despite the extensive analytic and numerical work, there appears to have been very limited experimental investigations on the natural convection in the melt, in particular the direct measurement of convective flows in a thermal gradient. Much of the limited experimental work has been on the temperature measurements and the direct flow measurements are very scarce for such a system.

Among the earliest experimental work on the magnetic damping of the thermally induced convection are the papers by Hurle [1966] and Hurle, *et al.* [1974]. They observed temperature oscillation in molten gallium contained in an open rectangular container. The oscillation is suppressed when a magnetic field is applied perpendicular to the main convective flow.

Okada and Ozoe [1992] measured temperature profile in the molten gallium contained in a cubic cavity. The measurements validated their modeling results that the damping effect is weakest when the magnetic field is horizontal and parallel to the hot wall [Ozoe and Okada, 1989].

Koster et al. [1997] measured temperature field induced by natural convection of molten gallium in a rectangular box using a radioscopic technique. The radioscopic technique deduces the temperature field from density variation and is only applicable to thin layers of fluid. Because the temperature in low Prandtl number fluid is a week function of density, the resolution of the radioscopic system is limited.

Davoust *et al.* [1999] experimentally studied, through thermal measurements, the effect of magnetic damping on a horizontal cylinder filled with mercury subjected to a vertical magnetic field. The data collected were used to verify the numerical predictions of Alboussière *et al.* [1993] and BenHadid *et al.* [1996].

Juel *et al.* [1999] conducted a combined numerical and experimental investigation on magnetic damping of the temperature gradient induced natural convection. They measured vertical temperature difference in molten gallium contained in a rectangular channel with an applied horizontal temperature gradient. Their experimental results agree with their numerical predictions well. It is found that with the increase of the Hartmann number, flow becomes 2-D. A similar experimental system was later used by Hof *et al.* [2003] for additional measurements.

All of the experimental work appeared in literature thus far has been on the temperature measurements from which magnetic damping effects are deduced. There appears to have been little work, if not at all, on the direct measurement of the thermally-induced melt convection in the presence of an external magnetic field. An experimental study of this type should be of crucial importance in providing a database to directly validate the numerical predictions from the numerical models in existence and under development. It should also be of great value in direct interpreting the physics governing the magnetic damping effects on convective flows in solidification systems.

Though the measurement of flow velocity is appealing to researchers working on material processing and energy conversion systems, to the best of our knowledge, no directly measured velocity profiles of the thermal convection are available in the literature. This is due to the lack of instrumentation suitable for melt flow. Velocity mapping in melt flow is plagued by the peculiarities of the liquid metal like opaque and chemically aggressive. The optic methods such as PIV and LDA are not applicable to the opaque liquid metal flow.

Incorporated magnetic probes have been used in liquid metal flows [Ricou and Vives, 1982; Kapulla *et al.*, 2000], and it was found that the accuracy of the measurement is impaired severely due to the Ohmic losses. The size of the probe is considered a major limiting factor for the experimental study of natural convection in a typical cavity.

Brito *et al.* [2001] used the Ultrasonic Doppler method to measure the local velocity of liquid gallium generated by a rotating disc; the main problem they encountered is the signal noise that comes from the gallium oxides. They reported that velocity signals could not be clearly identified from noises several minutes after measurements have started.

Eckert and Gerbeth [2002] applied the Ultrasound Doppler method to sodium flow in a square duct at 145 ˚C, which was exposed to a traverse magnetic field. They reported a velocity resolution of 9 mm/sec.

Eckert *et al.* [2001] proposed a mechano-optical technique for opaque fluid measurements, by which successful measurements have been made in the InGaSn eutectic melt driven by a rotating magnetic field. The calibration curves they reported showed that the technique is sensitive to the fluid density and therefore, extra uncertainties may be introduced when it is used to measure non-isothermal flow. It was also demonstrated that the calibration curves were sensitive to the flow directions. For low velocity melt flow measurements, the signals can be weak and some times a sphere is attached at the tip to increase the probe response to the flow. The lowest velocity level reported by the researchers was around 2 cm/s.

Prasad *et al*. [1994] used a solid-state electrochemical method to study convection in liquid tin with atomic oxygen as the tracer species. The convection effect is deduced

from the detection of the convection on the species transport using electrochemical cells as sensors. For a given set of experimental observations, however, more than one flow pattern may be derived and therefore, the electrochemical method needs to be accompanied by numerical simulations in order to generate any acceptable results.

Davoust et al. [1999] presented an experimental study of the magnetic damping effect using a horizontal cylinder filled with mercury under the presence of a vertical magnetic field. Two ends of the cylinder were kept at different temperatures and measurement was carried out using a platinum–constantan thermocouple and an electric potential sensors. They deduced the velocity from electric potential measurements.

In the present study, the steady convective flow in molten gallium that is induced by horizontal temperature gradients is investigated. The induced velocity and temperature fields are mapped simultaneously. Hot-film anemometry is used to measure local velocity in the liquid gallium. The application of the hot-film anemometry in liquid metal was made possible by the pioneer work of Sajben [1965], who presented a calibration technique that can used to eliminate the effect the impurity layer surrounding the hot-film probe. This technique has been used in liquid metal flow by several other researchers and consistent results have been demonstrated [Malcolm, 1969; Gardner and Lykoudis, 1971; Robinson and Larsson, 1973].

Gardner and Lykoudis [1971] studied the effects that a transverse magnetic has on mercury pipe flow. Several different types of hot-film probes were used. The probes were kept in the mercury during the experiment and it was found that the results were reproducible after near 300 hours of use.

Robinson and Larsson [1973] investigate the mercury flow driven by a 50 Hz rotating magnetic field using a conical hot-film probe. The platinum probe was coated with quartz and a thin layer of vanadium was deposit on the quartz layer to reduce the fouling effects. By this means, the changes in heat transfer due to the fouling effects were reported never exceeded ± 2.5 %.

1.3 Research Objectives

The present study has two major objectives.

Firstly, a numerical model is developed to simulate the melt flow contained in a Czochralski crucible and a linear stability analysis of the axisymmetric base flow based on the numerical simulation is carried out. The intention is to provide a basic understanding of the stability of the flows and its relation to the internal radiation. The high order finite difference method with compact scheme is used to obtain the axisymmetric flow and temperature fields. The radiative transfer equation for melt participating radiation problems is solved using discontinuous Galerkin method [Cui and Li, 2004]. The radiative heat flux is coupled with the axisymmetric base flow as a source term through iterative process. The stability analyses are performed by studying the eigenvalue spectrum using the large-scale eigenvalue solvers. Using the numerical model, the critical Grashof numbers for the melt flow instability is calculated as a function of Marangoni number and azimuthal wave number. The mechanism of the flow instability is discussed.

Secondly, an experimental study of natural convection in molten gallium with and without an imposed magnetic field is presented. The experimental system consists of a rectangular cell with a prescribed thermal gradient controlled by two water baths. The

temperature is measured using a thermocouples and the melt flow velocity field is determined using a hot film probes. The measured velocity and temperature profiles are used to compare with the predictions from numerical models developed in early studies [Shu *et al.*, 2002]. There exists good agreement between the numerical predictions and experimental measurements. Magnetic damping effects are observed in both the temperature and the velocity profiles when an external magnetic field is applied. The measured velocity and temperature fields should provide a valuable experimental database against which other numerical models developed for natural convection with and without an imposed magnetic field can be validated.

1.4 Dissertation Organization

This dissertation is organized as following.

Detailed mathematical descriptions, including the governing equations and the boundary conditions for the flow and temperature fields and radiative transfer calculations, of the melt flow in a Czochralski crucible are given in Chapter 2. Also presented in the chapter is a description of the experimental setup of the natural convection measurement.

In Chapter 3, the governing equations presented in Chapter 2 are solved for axisymmetric base flow using high order finite difference method. Infinitesimal disturbance is applied to the obtained axisymmetric base flow and linear stability analysis is carried out. The numerical simulation results were compared with previous theoretical and numerical studies of pure Rayleigh-Bénard convection and Marangoni convection in vertical cylinders. The stability analysis is carried out at various Grashof numbers and Marangoni-Reynolds numbers to reveal how the two effects interact with each other in

the coupled Rayleigh-Bénard-Marangoni flow. Stability of the fluid at various boundary conditions is also studied to investigate how the boundary conditions affect the stability of the flow.

Chapter 4 extends the numerical model to the melt flow by taking the internal radiation effect into account. A discontinuous finite element model for the radiative transfer equation is presented and coupled with the high order finite difference model. Stability analysis of the flow is conducted to reveal how the internal radiation changes the stability of the melt flow.

Chapter 5 presents the details, which includes calibration of the probe, measurement process, data processing, and measurement results, of the hot-film measurement of the natural convection in a rectangular cavity. The measured velocity and temperature fields are compared with the numerical predictions from a previous numerical model.

Finally, conclusions drawn from the present work and suggestions for future work are given in Chapter 6.

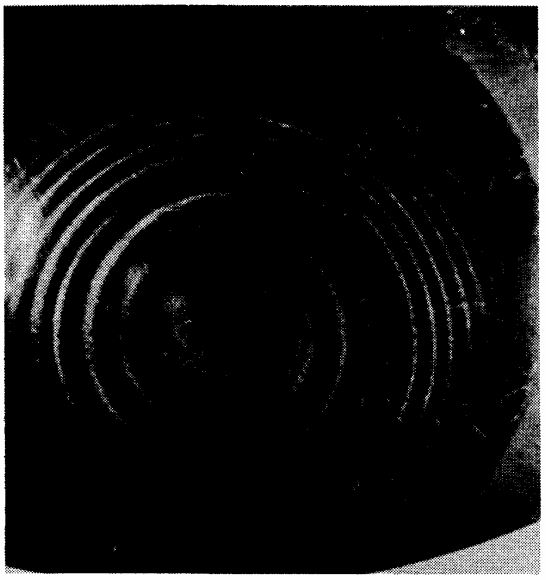

(a)

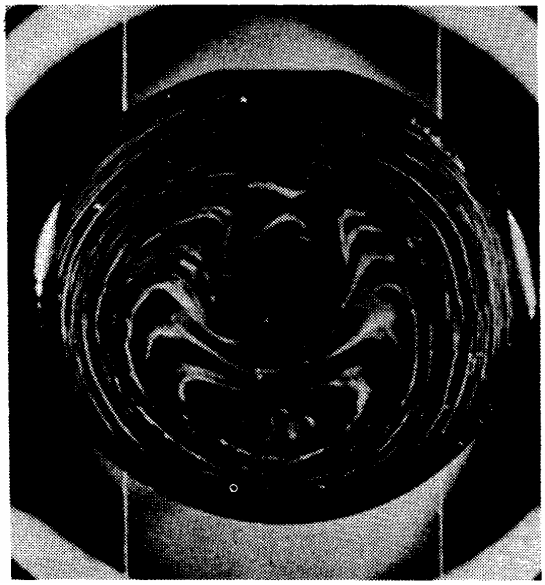

(b)

Figure 1.1 Inhomogeneous distributions of "swirl" defects in the preferentially etched Si surfaces. (a) CZ crystal and (b) float zone crystal. (From Tiller, 1992)

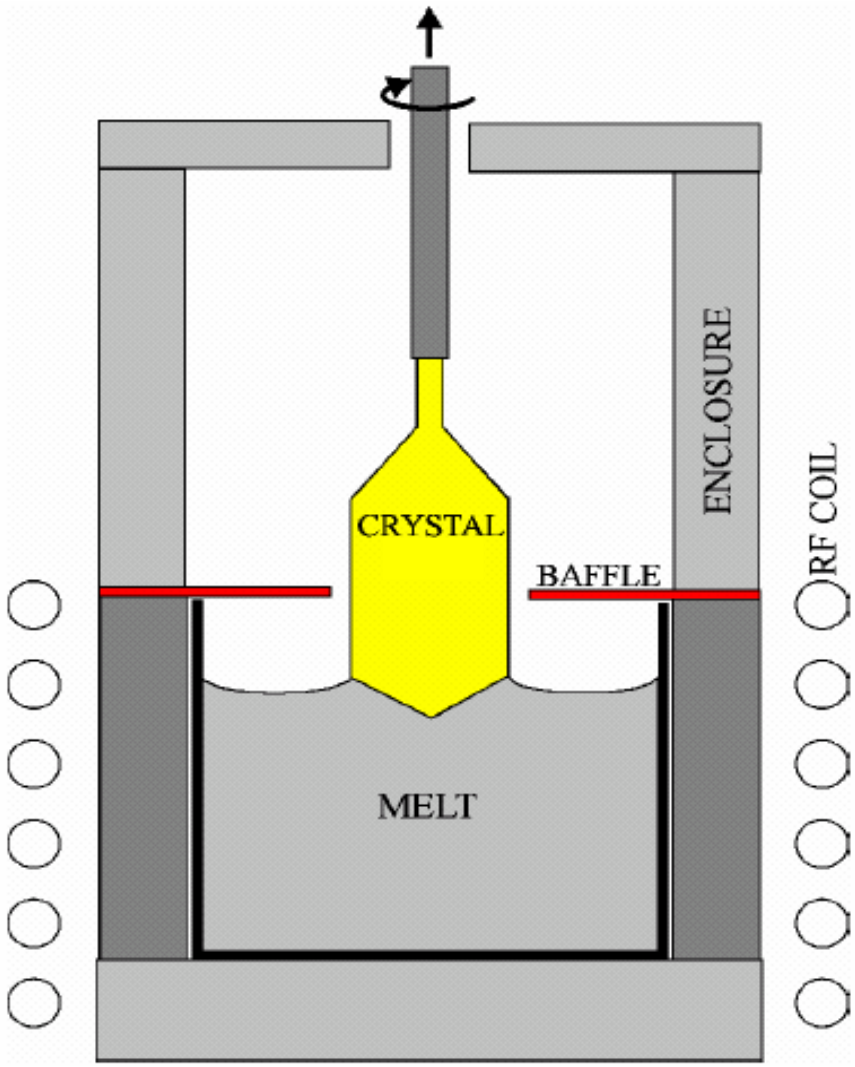

Figure 1.2 Schematics of Czochralski crystal growth system. (From Galazka, *et al.*, 2003)

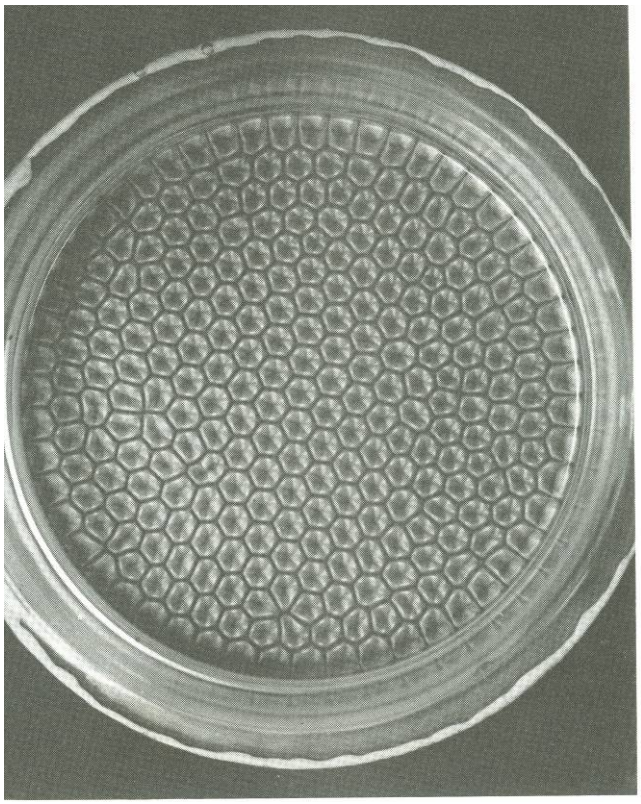

Figure 1.3 Bénard cells under an air surface. (From Koschmieder and Pallar, 1974)

CHAPTER TWO

PROBLEM STATEMENTS

2.1 Czochralski Crucible

In Czochralski crystal growth systems, the melt is contained in a vertical cylindrical crucible, which is shown in Figure 2.1. The cylindrical coordinate system used in the present study is also shown in the figure. The crucible is similar to that used by Jing [1999]. It is a vertical cylinder with height of H and radius of R. A constant heat flux q is applied at the vertical wall to heat the melt inside the crucible. The center part of the top surface is in contact with a crystal of radius R_d at constant temperature T_d. Radiative cooling condition is assumed at the free surface. The bottom wall is adiabatic. The top surface is non-deformable free surface.

2.2 Governing Equations

The melt is an incompressible fluid, to which the Boussinesq approximation applies. This means that the variation of density is neglected everywhere except in buoyancy [Drazin and Reid, 1981]. On the basis of this approximation, density of the melt is a function of temperature that can be written as

$$\rho = \rho_{ref}\left[1 - \beta\left(\Theta - \Theta_{ref}\right)\right], \tag{2.1}$$

where ρ is the density, Θ the temperature, and β the thermal expansion coefficient of the melt. The subscript *ref* denotes the properties at a reference state.

The surface tension of the melt varies with the temperature of the fluid. The equation of state of the surface tension is approximated by

$$\sigma = \sigma_{ref} - \gamma(\Theta - \Theta_{ref}), \tag{2.2}$$

where σ is the surface tension and γ=-dσ/dΘ is the negative rate of change of surface tension with temperature [Davis, 1987]. Equation 2.2 implies that the spot with higher temperature has lower surface tension and therefore, flow is driven from high temperature to low temperature along the free surface due the so called Marangoni or thermocapillary effect.

The melt flow inside the crucible are described by the conservation laws of mass, momentum, and energy, of which governing equations are written as

$$\nabla \cdot \dot{\mathbf{u}} = 0, \tag{2.3}$$

$$\rho \frac{\partial \dot{\mathbf{u}}}{\partial \dot{t}} + \rho(\dot{\mathbf{u}} \cdot \nabla)\dot{\mathbf{u}} = -\nabla \dot{p} + \mu \nabla^2 \dot{\mathbf{u}} + \mathbf{f}, \tag{2.4}$$

$$\rho c_p \frac{\partial \Theta}{\partial \dot{t}} + \rho c_p (\dot{\mathbf{u}} \cdot \nabla)\Theta = k \nabla^2 \Theta + \dot{Q}, \tag{2.5}$$

where $\dot{\mathbf{u}}$ is the velocity vector, $\dot{t}$ the time, $\dot{p}$ the pressure, μ the dynamic viscosity, $\mathbf{f}$ the body force, C_p the specific heat of the melt, k the thermal conductivity of the melt and $\dot{Q}$ the volumetric heat source.

2.3 Dimensionless Governing Equations in Cylindrical Coordinate System

In the cylindrical coordinate system (r, z, θ), the governing equations given in Equations 2.3-2.5 can be written in terms of dimensionless flow field $\mathbf{u}(u_r, u_z, u_\theta)$, temperature field T and pressure p as,

$$\frac{1}{r}\frac{\partial(ru_r)}{\partial r}+\frac{1}{r}\frac{\partial u_\theta}{\partial \theta}+\frac{\partial u_z}{\partial z}=0\,, \tag{2.6}$$

$$\begin{aligned}&\frac{\partial u_r}{\partial t}+u_r\frac{\partial u_r}{\partial r}+u_z\frac{\partial u_r}{\partial z}+\frac{u_\theta}{r}\frac{\partial u_r}{\partial \theta}-\frac{u_\theta^2}{r}\\&=-\frac{\partial p}{\partial r}+\left(\frac{\partial^2 u_r}{\partial r^2}+\frac{\partial^2 u_r}{\partial z^2}+\frac{1}{r^2}\frac{\partial^2 u_r}{\partial \theta^2}+\frac{1}{r}\frac{\partial u_r}{\partial r}-\frac{u_r}{r^2}-\frac{2}{r^2}\frac{\partial u_\theta}{\partial \theta}\right)\end{aligned}\,, \tag{2.7}$$

$$\begin{aligned}&\frac{\partial u_z}{\partial t}+u_r\frac{\partial u_z}{\partial r}+u_z\frac{\partial u_z}{\partial z}+\frac{u_\theta}{r}\frac{\partial u_z}{\partial \theta}\\&=-\frac{\partial p}{\partial z}+\left(\frac{\partial^2 u_z}{\partial r^2}+\frac{\partial^2 u_z}{\partial z^2}+\frac{1}{r^2}\frac{\partial^2 u_z}{\partial \theta^2}+\frac{1}{r}\frac{\partial u_z}{\partial r}\right)-\mathrm{Gr}(T-1)\end{aligned}\,, \tag{2.8}$$

$$\begin{aligned}&\frac{\partial u_\theta}{\partial t}+u_r\frac{\partial u_\theta}{\partial r}+u_z\frac{\partial u_\theta}{\partial z}+\frac{u_\theta}{r}\frac{\partial u_\theta}{\partial \theta}+\frac{u_r u_\theta}{r}\\&=-\frac{1}{r}\frac{\partial p}{\partial \theta}+\left(\frac{\partial^2 u_\theta}{\partial r^2}+\frac{\partial^2 u_\theta}{\partial z^2}+\frac{1}{r^2}\frac{\partial^2 u_\theta}{\partial \theta^2}+\frac{1}{r}\frac{\partial u_\theta}{\partial r}-\frac{u_\theta}{r^2}+\frac{2}{r^2}\frac{\partial u_r}{\partial \theta}\right)\end{aligned}\,, \tag{2.9}$$

$$\begin{aligned}&\frac{\partial T}{\partial t}+u_r\frac{\partial T}{\partial r}+u_z\frac{\partial T}{\partial z}+\frac{u_\theta}{r}\frac{\partial T}{\partial \theta}\\&=\frac{1}{\mathrm{Pr}}\left(\frac{\partial^2 T}{\partial r^2}+\frac{\partial^2 T}{\partial z^2}+\frac{1}{r^2}\frac{\partial^2 T}{\partial \theta^2}+\frac{1}{r}\frac{\partial T}{\partial r}\right)-Q\end{aligned}\,, \tag{2.10}$$

where Gr is the Grashof number which is given by

$$\mathrm{Gr}=\frac{g\beta T_{ref}H^3}{\nu^2}\,, \tag{2.11}$$

where g is the gravity acceleration, ν is kinematic viscosity and Pr is the Prandtl number which is defined as

$$\mathrm{Pr} = \frac{\nu}{\alpha}, \tag{2.12}$$

where α the thermal diffusivity which is defined as,

$$\alpha = \frac{k}{\rho c_p}. \tag{2.13}$$

The Grashof number characterizes the strength of the Rayleigh effect.

Equations 2.6-2.10 were obtained using the following scaling factors,

$$\mathbf{x} = \frac{\dot{\mathbf{x}}}{H}; \quad \mathbf{u} = \frac{H}{\nu}\dot{\mathbf{u}}; \quad p = \frac{H^2}{\rho\nu^2}\dot{p};$$

$$t = \frac{\nu}{H^2}\dot{t}; \quad T = \frac{\Theta}{\Theta_{ref}}; \quad Q = \frac{H^2}{\nu\Theta_{ref}\rho C_p}\dot{Q}.$$

2.4 Boundary Conditions

To solve the melt flow in the Czochralski crucible, the following constraints are applied at the system boundaries. At the free surface (R_d<r<R, z=H)

$$\frac{\partial u_r}{\partial z} = \mathrm{Re}_\gamma \frac{\partial T}{\partial r}, \tag{2.14}$$

$$\frac{\partial u_\theta}{\partial z} = \mathrm{Re}_\gamma \frac{\partial T}{r\partial \theta}, \tag{2.15}$$

$$u_z = 0, \tag{2.16}$$

$$\frac{\partial T}{\partial z} = -\mathrm{Rad}\left(T^4 - T_{amb}^4\right), \tag{2.17}$$

where T_{amb} is the temperature of the ambient air, $\mathrm{Rad} = \dfrac{\delta \varepsilon T_{ref}^3 H}{\kappa}$ is the radiation number and Re_γ is the Marangoni-Reynolds number given by

$$\mathrm{Re}_\gamma = \frac{\gamma T_{ref} H}{\mu \nu}. \tag{2.18}$$

The Marangoni-Reynolds number characterizes the strength of the Marangoni effect. It is worth noting that Equations 2.14 and 2.15 indicate that the surface tension gradient is balanced by the shear stress. Equation 2.16 means that the free surface is flat and non-deformable.

At the crystal interface ($r \le R_d$ and $z=H$), the melt is at constant temperature T_d and the interface is considered rigid wall,

$$u_r = u_z = u_\theta = 0, \tag{2.19}$$

$$T = T_d. \tag{2.20}$$

At the vertical wall ($r=R,\ 0<z<H$), a constant heat flux is supplied to the melt and the vertical wall is rigid,

$$u_r = u_z = u_\theta = 0\,, \tag{2.21}$$

$$\frac{\partial T}{\partial r} = q\,, \tag{2.22}$$

where q is the constant heat flux at the vertical wall. The heat flux is non-dimensionalized using

$$q = \frac{H}{kT_{ref}}\dot{q}\,, \tag{2.23}$$

where $\dot{q}$ is the primitive heat flux.

The bottom wall ($0<r<R$, $z=0$) of the crucible is adiabatic and rigid,

$$u_r = u_z = u_\theta = \frac{\partial T}{\partial z} = 0\,. \tag{2.24}$$

2.5 Magnetic Damping of Natural Convection in a Rectangular Box

Magnetic damping effect on natural convection is investigated by direct measurements of the induced flow and temperature fields. The molten gallium is used as working fluid and is contained in a rectangular box. A horizontal temperature gradient is

applied across the gallium by holding two opposite vertical walls at different temperatures. In this case, convective flow is induced by the density gradient caused by the temperature difference with the melt flow upwards near the hot wall and downwards near the cold wall, as shown in Figure 2.2.

A static horizontal magnetic field is applied to damp the natural convection. The applied magnetic field induces a non-uniform electromotive field in the melt. The electromotive field causes electrical currents which interact with the applied magnetic field to damp the convective flow in the melt.

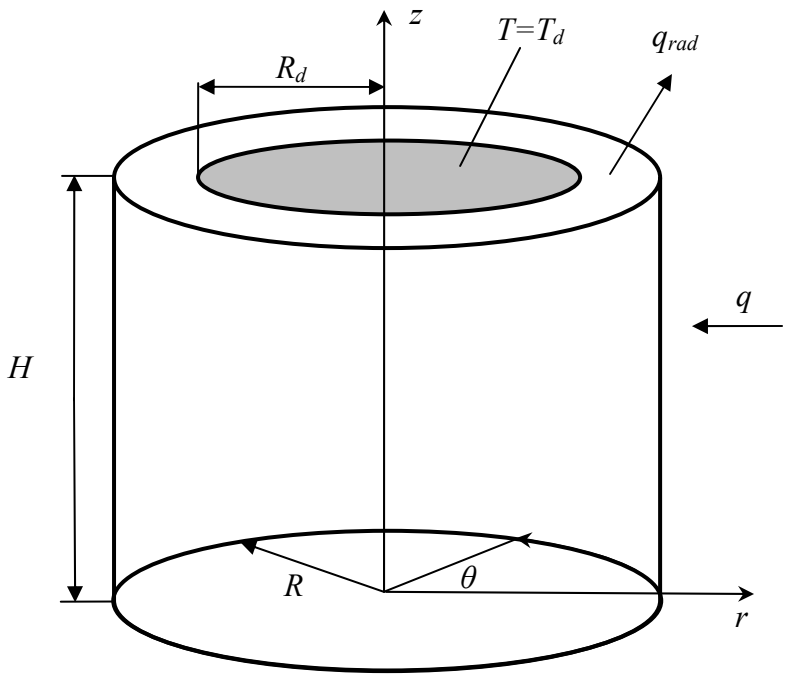

Figure 2.1 Schematics of the Czochralski crucible under investigation.

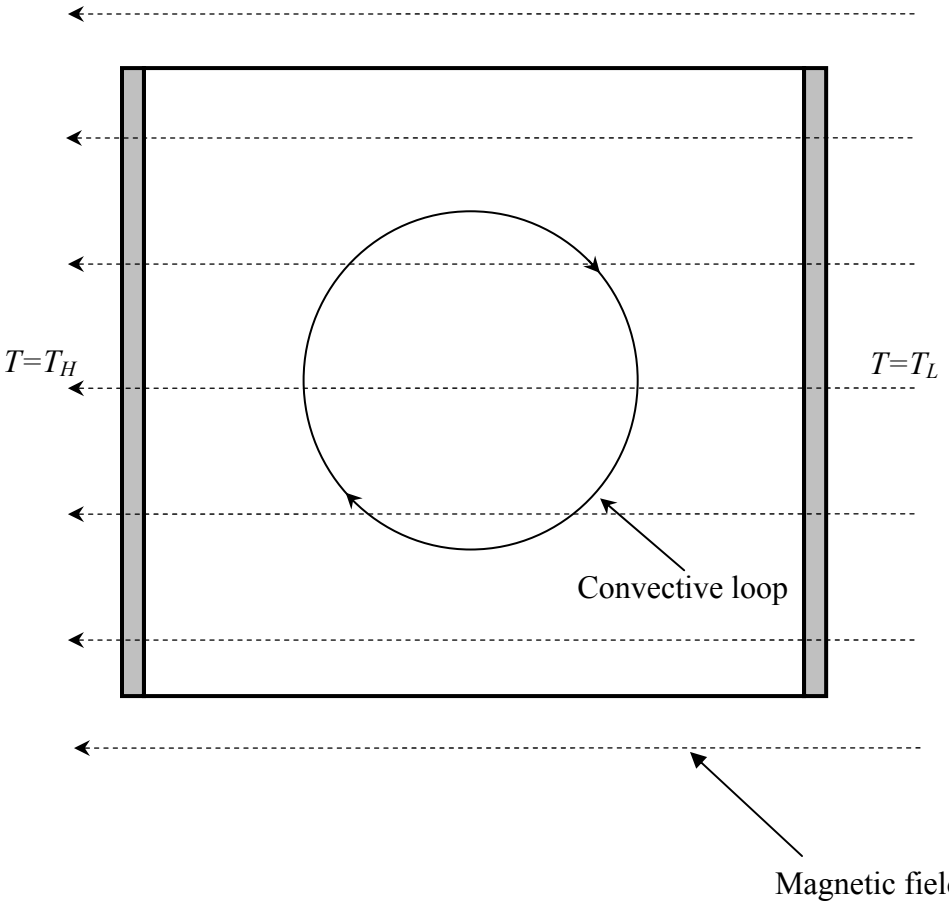

Figure 2.2 Magnetic damping of natural convection in a rectangular box (T_H>T_L).

CHAPTER THREE

NUMERICAL SIMULATION AND STABILITY OF RAYLEIGH-BÉNARD-MARANGONI CONVECTION IN CRYSTAL GROWTH SYSTEMS

This chapter presents a numerical model of melt flow in Czochralski crystal growth systems. The numerical model uses high order finite difference model to solve the governing equations given in Chapter 2 along with the boundary conditions for axisymmetric flow in the crucibles. A linear stability analysis is carried out based on the axisymmetric base flow. Small perturbation is applied to the calculated base flow to determine the critical Marangoni numbers and Grashof numbers at which the axisymmetry is broken. The eigenvalue matrix equation is solved using linear fractional transformation with banded matrix structure taken into account. The objectives of this chapter are to provide a basic understanding of the physics underlying the melt flow, the stability of the axisymmetric flow and its relations to the crucible configurations.

3.1 Governing Equations for Axisymmetric Base Flow in Czochralski Crucible

In the last chapter, mathematical descriptions of the melts flow in the Czochralski crucibles were presented. It is well known that when the lateral heat flux, i.e., the temperature gradient along the free surface is small enough, the melt flow is axisymmetric [Vrentas *et al.*, 1981; Rubinov *et al.*, 2004]. In the cylindrical coordinate system, the axisymmetric velocity field $\overline{\mathbf{U}}\left(\overline{U}_r, \overline{U}_z, 0\right)$, temperature field $\overline{T}$ and pressure flied $\overline{P}$ are governed by

$$\frac{1}{r}\frac{\partial(ru_r)}{\partial r}+\frac{\partial u_z}{\partial z}=0\,, \tag{3.1}$$

$$\frac{\partial u_r}{\partial t}+u_r\frac{\partial u_r}{\partial r}+u_z\frac{\partial u_r}{\partial z}=-\frac{\partial p}{\partial r}+(\frac{\partial^2 u_r}{\partial r^2}+\frac{\partial^2 u_r}{\partial z^2}+\frac{1}{r}\frac{\partial u_r}{\partial r}-\frac{u_r}{r^2})\,, \tag{3.2}$$

$$\frac{\partial u_z}{\partial t}+u_r\frac{\partial u_z}{\partial r}+u_z\frac{\partial u_z}{\partial z}=-\frac{\partial p}{\partial z}+(\frac{\partial^2 u_z}{\partial r^2}+\frac{\partial^2 u_z}{\partial z^2}+\frac{1}{r}\frac{\partial u_z}{\partial r})-\mathrm{Gr}(T-1)\,, \tag{3.3}$$

$$\frac{\partial T}{\partial t}+u_r\frac{\partial T}{\partial r}+u_z\frac{\partial T}{\partial z}=\frac{1}{\mathrm{Pr}}\left(\frac{\partial^2 T}{\partial r^2}+\frac{\partial^2 T}{\partial z^2}+\frac{1}{r}\frac{\partial T}{\partial r}\right)-Q\,, \tag{3.4}$$

The corresponding boundary conditions for the axisymmetric base flow are the same as those given in the last chapter except that the Marangoni force in θ direction given in Equation 2.15 vanishes.

3.2 Linear Stability Analysis of the Axisymmetric Base Flow

3.2.1 Hydrodynamic stability theory

The problem of hydrodynamic stability was introduced to study the transit in flow patterns, such as from laminar flow to turbulence. The basic idea of the hydrodynamic stability theory is given as following.

For steady state solution of the governing equations presented in the last section, $\overline{\mathbf{U}}(\overline{U}_x,\overline{U}_y,\overline{U}_z)$, $\overline{P}$ and $\overline{T}$, infinitesimal perturbations are applied as

$$\begin{pmatrix} U_x \\ U_y \\ U_z \\ P \\ T \end{pmatrix} = \begin{pmatrix} \overline{U}_x \\ \overline{U}_y \\ \overline{U}_z \\ \overline{P} \\ \overline{T} \end{pmatrix} + \begin{pmatrix} U'_x \\ U'_y \\ U'_z \\ P' \\ T' \end{pmatrix} \tag{3.5}$$

where the primed variables are the small perturbations have the form of

$$\mathbf{U}' = \sum_{k=1}^{\infty} \varepsilon^{(k)} \mathbf{u}^{(k)} \tag{3.6}$$

$$P' = \sum_{k=1}^{\infty} \varepsilon^{(k)} p^{(k)} \tag{3.7}$$

$$T' = \sum_{k=1}^{\infty} \varepsilon^{(k)} T^{(k)} \tag{3.8}$$

where ε is a small constant number, $\mathbf{u}^{(k)}$, $p^{(k)}$ and $T^{(k)}$ are the k^{th} order disturbances deviated from the steady state solutions. If the given disturbances vanish as time increases, in other words the perturbations die out eventually, the flow is stable. The flow is considered unstable if the perturbations remain constant or grow with time. In case of unstable flow, the flow pattern changes either from laminar flow to turbulence or from one laminar flow pattern to another as time increases.

Direct solution of the Navier-Stokes equations is notoriously difficult, if not impossible, due to their high non-linearity. With the assumption of small perturbation, the Navier-Stokes equations can be linearized. By inserting the small perturbations given

in Equations 3.6-3.8 into the governing equations and neglecting the higher order perturbations and their derivatives, the following linearized equations are obtained

$$\nabla \cdot \mathbf{u}^{(1)} = 0, \tag{3.9}$$

$$\rho \frac{\partial \mathbf{u}^{(1)}}{\partial t} + \rho \overline{\mathbf{U}} \cdot \nabla \mathbf{u}^{(1)} + \rho \mathbf{u}^{(1)} \cdot \nabla \overline{\mathbf{U}} = -\nabla p^{(1)} + \mu \nabla^2 \mathbf{u}^{(1)}, \tag{3.10}$$

$$\rho \frac{\partial T^{(1)}}{\partial t} + \rho \overline{\mathbf{U}} \cdot \nabla T^{(1)} + \rho \mathbf{u}^{(1)} \cdot \nabla T = \frac{1}{\mathrm{Pr}} \nabla^2 T^{(1)} \tag{3.11}$$

For a given steady state solution of the base flow, the first order perturbations $\mathbf{u}^{(1)}$, $T^{(1)}$ and $p^{(1)}$ can be solved from the linear equation system given in Equations 3. 9-3.11.

According to the principle of separation of variables, the solutions of the linear equations system have an exponential time factor

$$\mathbf{u}^{(1)} = \phi_{\mathbf{u}}(\mathbf{x}) \exp(\varpi_{\mathbf{u}} t), \tag{3.12}$$

$$T^{(1)} = \phi_T(\mathbf{x}) \exp(\varpi_T t), \tag{3.13}$$

$$p^{(1)} = \phi_p(\mathbf{x}) \exp(\varpi_p t), \tag{3.14}$$

where $\mathbf{x}$ is the direction vector. It is worth noting that ω is the complex wave speed that can be written as

$$\varpi = \varpi_r + i\varpi_i \tag{3.15}$$

Here ω_i is the azimuthal frequency of oscillation, and ω_r determines the degree of amplification or damping. According to the linear stability theory, when $\omega_i = 0$, the disturbance grows or decays monotonically. When $\omega_i \neq 0$, the perturbation is oscillatory with wave speed of ω_i. The perturbation decays and the base flow is stable if $\omega_r < 0$. When $\omega_r > 0$ the perturbation grows with time and the base flow loses its axisymmetry. The neutral state is determined by $\omega_r = 0$.

Extensive previous efforts have been made to the linear stability analysis of fluid flow in bounded configurations with and without heat transfer. The most widely studied wall-bounded cases include Couette, Poiseuille and channel flows. The methodologies for the hydrodynamic stability have been well established, starting from the early days' singular perturbation method to the more recently developed spectral based numerical method. The linear stability analysis theory presented in this section has been widely used as a first step to study the flow stability problems, and interests in these problems is still growing because of its fundamental and practical importance [Ding and Kawahara, 1999; Priede and Gerbeth, 1999; Shatrov, *et al.*, 2001].

3.2.2 Linear stability analysis of melt flow in Czochralski crucible

Stability of the axisymmetric convective flow in the Czochralski crucible is studied in this section by solving the linearized governing equations. Small perturbations are applied to the axisymmetric base flow. To carried out the stability analysis, the governing equations given in Section 3.1 are rewritten with assumption of slight compressibility as [Ding and Kawahara, 1998]

$$\frac{\partial p}{\partial t} + (\mathbf{u} \cdot \nabla) p + \frac{1}{\mathrm{M}} \nabla \cdot \mathbf{u} = 0, \tag{3.16}$$

$$\frac{\partial \mathbf{u}}{\partial t} + (\mathbf{u} \cdot \nabla)\mathbf{u} = -\frac{1}{\mathrm{M}} \nabla p + \left[\nabla^2 \mathbf{u} + \frac{1}{3} \nabla (\nabla \cdot \mathbf{u}) \right] + \mathbf{f}, \tag{3.17}$$

$$\frac{\partial \Theta}{\partial t} + (\mathbf{u} \cdot \nabla)\Theta = \frac{1}{\mathrm{Pr}} \nabla^2 \Theta + Q, \tag{3.18}$$

where M is the Mach number defined by

$$\mathrm{M} = \frac{U}{C} \tag{3.19}$$

where C is the acoustic speed of the fluid.

The axisymmetric base flow velocity field $\overline{\mathbf{U}}(\overline{U}_r, \overline{U}_z, 0)$, pressure $\overline{P}$ and temperature $\overline{T}$ obtained using the governing equations in Section 3.1 are perturbed by three-dimensional infinitesimal perturbations as

$$U_r = \overline{U}_r + U_r' \tag{3.20}$$

$$U_z = \overline{U}_z + U_z' \tag{3.21}$$

$$U_\theta = 0 + U_\theta' \tag{3.22}$$

$$P = \overline{P} + P' \tag{3.23}$$

$$T = \overline{T} + T'. \tag{3.24}$$

The last terms on the right-hand side of Equations 3.20-3.24 are the small perturbations applied to the base flow which can be written in the cylindrical coordinate system in terms of the normal mode as

$$U_r' = \hat{U}_r(r,z)\exp(im\theta + \varpi t), \tag{3.25}$$

$$U_z' = \hat{U}_z(r,z)\exp(im\theta + \varpi t), \tag{3.26}$$

$$U_\theta' = \hat{U}_\theta(r,z)\exp(im\theta + \varpi t), \tag{3.27}$$

$$P' = \hat{P}(r,z)\exp(im\theta + \varpi t), \tag{3.28}$$

$$T' = \hat{T}(r,z)\exp(im\theta + \varpi t), \tag{3.29}$$

where $i = \sqrt{-1}$ is the imaginary unit and m is the azimuthal wave number.

Inserting Equations 3.20-3.29 into the governing equations given in Equations 3.16-3.18 and subtracting the base flow from it, the final perturbation equations are obtained as

$$\begin{aligned} &\varpi\,\hat{P} + \hat{U}_r\frac{\partial P}{\partial r} + \hat{U}_z\frac{\partial P}{\partial z} + U_r\frac{\partial \hat{P}}{\partial r} + \frac{imU_\theta\hat{P}}{r} + \\ &U_z\frac{\partial \hat{P}}{\partial z} + \frac{1}{\mathrm{M}}\left[\frac{\hat{U}_r}{r} + \frac{\partial \hat{U}_r}{\partial r} + \frac{im\hat{U}_\theta}{r} + \frac{\partial \hat{U}_z}{\partial z}\right] = 0 \end{aligned}, \tag{3.30}$$

$$
\begin{aligned}
&\varpi\hat{U}_r + U_r\frac{\partial\hat{U}_r}{\partial r} + \hat{U}_r\frac{\partial U_r}{\partial r} + U_z\frac{\partial\hat{U}_r}{\partial z} \\
&+ \hat{U}_z\frac{\partial U_r}{\partial z} + \frac{imU_\theta\hat{U}_r}{r} - \frac{2\hat{U}_\theta U_\theta}{r} \\
&= -\frac{1}{\mathrm{M}}\frac{\partial\hat{P}}{\partial r} + \frac{4}{3}\frac{\partial^2\hat{U}_r}{\partial r^2} + \frac{\partial^2\hat{U}_r}{\partial z^2} - \left(\frac{\delta^2}{r^2} + \frac{4}{3r^2}\right)\hat{U}_r + \frac{im}{3r}\frac{\partial\hat{U}_\theta}{\partial r} \\
&+ \frac{1}{3}\frac{\partial^2\hat{U}_z}{\partial r\partial z} - \frac{7im}{3r^2}\hat{U}_\theta + \frac{4}{3r}\frac{\partial\hat{U}_r}{\partial r}
\end{aligned}
\quad , \tag{3.31}
$$

$$
\begin{aligned}
&\varpi\hat{U}_z + U_r\frac{\partial\hat{U}_z}{\partial r} + \hat{U}_r\frac{\partial U_z}{\partial r} + U_z\frac{\partial\hat{U}_z}{\partial z} + \hat{U}_z\frac{\partial U_z}{\partial z} + \frac{imU_\theta}{r}\hat{U}_z \\
&= -\frac{1}{\mathrm{M}}\frac{\partial\hat{P}}{\partial z} + \frac{\partial^2\hat{U}_z}{\partial r^2} + \frac{4}{3}\frac{\partial^2\hat{U}_z}{\partial z^2} + \frac{1}{3}\frac{\partial^2\hat{U}_r}{\partial r\partial z} + \frac{im}{3r}\frac{\partial\hat{U}_\theta}{\partial z} + \frac{1}{r}\frac{\partial\hat{U}_z}{\partial r} \\
&+ \frac{1}{3r}\frac{\partial\hat{U}_r}{\partial z} - \frac{m^2}{r^2}\hat{U}_z + \mathrm{Gr}\cdot\hat{T}
\end{aligned}
\quad , \tag{3.32}
$$

$$
\begin{aligned}
&\varpi\hat{U}_\theta + U_r\frac{\partial\hat{U}_\theta}{\partial r} + \hat{U}_r\frac{\partial U_\theta}{\partial r} + U_z\frac{\partial\hat{U}_\theta}{\partial z} + \hat{U}_z\frac{\partial U_\theta}{\partial r} \\
&+ im\frac{U_\theta}{r}\hat{U}_\theta + \frac{U_r\hat{U}_\theta + \hat{U}_rU_\theta}{r} = -\frac{im}{r\mathrm{M}}\hat{P} + \frac{\partial^2\hat{U}_\theta}{\partial r^2} + \frac{\partial^2\hat{U}_\theta}{\partial z^2} \\
&+ \frac{im}{3r}\frac{\partial\hat{U}_r}{\partial r} + \frac{im}{3r}\frac{\partial\hat{U}_z}{\partial z} + \frac{1}{r}\frac{\partial\hat{U}_\theta}{\partial r} + \frac{7im}{3r^2}\hat{U}_r - \frac{1}{r^2}\left(\frac{4m^2}{3} + 1\right)\hat{U}_\theta
\end{aligned}
\quad , \tag{3.33}
$$

$$
\begin{aligned}
&\varpi\hat{T} + U_r\frac{\partial\hat{T}}{\partial r} + \hat{U}_r\frac{\partial T}{\partial r} + U_z\frac{\partial\hat{T}}{\partial z} + \hat{U}_z\frac{\partial T}{\partial r} + \frac{imU_\theta}{r}\hat{T} \\
&= \frac{1}{\mathrm{Pr}}\left[\frac{\partial^2\hat{T}}{\partial r^2} + \frac{\partial^2\hat{T}}{\partial z^2} + \frac{1}{r}\frac{\partial\hat{T}}{\partial r} - \frac{m^2}{r^2}\hat{T}\right]
\end{aligned}
\quad , \tag{3.34}
$$

The perturbation equations form an eigenvalue problem with the growth rate being the eigenvalue.

The final perturbation equations are subject to the following boundary conditions. At the free surface (R_d<r<R, z=H)

$$\frac{\partial \hat{U}_r}{\partial z} = \mathrm{Re}_\gamma \frac{\partial \hat{T}}{\partial r}, \tag{3.35}$$

$$\frac{\partial \hat{U}_\theta}{\partial z} = \mathrm{Re}_\gamma \frac{im\hat{T}}{r}, \tag{3.36}$$

$$\hat{U}_z = 0, \tag{3.37}$$

$$\frac{\partial \hat{T}}{\partial z} = -4\mathrm{Rad}T^3\hat{T}, \tag{3.38}$$

At the crystal interface ($r \le R_d$ and $z=H$),

$$\hat{U}_r = \hat{U}_z = \hat{U}_\theta = \hat{T} = 0, \tag{3.39}$$

At the vertical wall ($r=R$, $0<z<H$),

$$\hat{U}_r = \hat{U}_z = \hat{U}_\theta = \frac{\partial \hat{T}}{\partial z} = 0, \tag{3.40}$$

At the bottom wall ($0<r<R$, $z=0$),

$$\hat{U}_r = \hat{U}_z = \hat{U}_\theta = \frac{\partial \hat{T}}{\partial z} = 0. \tag{3.41}$$

The periodic boundary condition in azimuthal (θ) direction is automatically satisfied when the wave number m is a set of discrete numbers, i.e., m=0, 1, 2,….

3.3 Numerical Scheme

In the present study, the high order finite difference method is used to solve the governing equations. The spatial derivatives are discretized by the compact method. The method of fractional steps or project method is applied to carry out the time integration. The fourth-order compact approximation derived by means of 5-point Legendre interpolation is adopted here [Ai, 2004].

3.3.1 High order finite different scheme

Various numerical techniques are available for the simulation of fluid flow and/or heat transfer phenomena in the materials processing systems. Spectral method provides perhaps the highest order of accuracy among all the available numerical techniques. However, it is time-consuming and lack of flexibility in handling complex geometry [Pruett and Zang, 1992; Rai and Moin, 1993; Rist and Fasel, 1995; Adams and Kleiser, 1996]. Recently, high order difference methods [Christie, 1985; Lele, 1992; Sabau, and Raad, 1999] have emerged as one of the promising alternative for the spectral method. It has spectral-like accuracy. The high order finite difference method is also well known for its computational efficiency and outstanding flexibility in dealing with irregular geometry and various boundary conditions. In this section, the high order finite difference method is used to simulate the axisymmetric melt flow in the Czochralski crucibles.

As one of most widely used high order finite difference methods, the compact difference schemes have spectral-like resolution and high order of accuracy [Lele, 1992]. Previous investigations have shown that the central compact difference schemes are

successful in numerical simulation of diffusion dominated flows and the upwinding central difference schemes are excellent for solution of the convection dominated problems [Christie, 1985; Zhong, 1998]. A brief description of the basic ideas of the compact difference schemes used in the present work will be given in the following paragraphs.

In the present work, the high order finite difference model is developed using compact central difference scheme, for which approximation of n^{th} order derivative of variable u with respect to x at the i^{th} grid point is generally written as

$$\sum_{k=-M_0}^{M_0} b_{i+k} u_{i+k}^{(n)} = \frac{1}{h^n} \sum_{k=-N_0}^{N_0} a_{i+k} u_{i+k} \tag{3.42}$$

where $u_{i+k}^{(n)} = \partial^n u / \partial x^n$ denotes the n^{th} order derivative of variable u with respect to x at the i^{th} grid point. The simulation is carried out on a uniform mesh with grid spacing of h. M_0 and N_0 are the number of points biased with respect to the point i. If M_0=0, the finite difference scheme is explicit, otherwise, the method is implicit and also called compact difference scheme. The compact difference scheme has been favored for direct numerical simulation of transitional and turbulent flow because of its smaller truncation errors and narrow local grid stencils. The stability analyses have shown that the stability properties of compact and explicit finite difference schemes of the same order are similar. However, more boundary closures are need for the explicit finite difference method to achieve the same order of accuracy as the compact difference scheme. The explicit finite difference method is more efficient in derivative approximations and easier to be

incorporated with implicit time-integration schemes. Between these two schemes, the compact difference scheme is more efficient in dealing with periodic boundary conditions while the explicit finite difference method is more suitable for non-periodic boundary conditions. However, for the discretization in the directions with non-periodic boundary conditions, the accuracy of the approximations is often limited by the accuracy of the boundary discretizations. In this case, both the explicit and the compact finite difference schemes can be used.

Equation 3.42 presents the compact difference scheme central grid stencils used in the present study. The accuracy of the compact difference is determined by the number of the points biased with respect to the point i, M_0 and N_0. There are total of $2(M_0+N_0+1)$ coefficients (a_i and b_i) need to be determined in order to achieve the desired accuracy. Christie [1985] has shown that for an upwinding scheme, the maximum approximation order for $\partial^n u / \partial x^n$ is $p=2(M_0+N_0)-n$ and for a central scheme, the maximum approximation order is $p+1$.

In this chapter, the first order derivatives in the governing equations are approximated by a fourth order central compact difference scheme, which can be written in terms of three grid points as

$$\begin{bmatrix} 1 & 2 & & & \\ & \ddots & & & \\ & 1 & 4 & 1 & \\ & & & \ddots & \\ & & & 2 & 1 \end{bmatrix} \begin{bmatrix} u'_1 \\ \vdots \\ u'_i \\ \vdots \\ u'_N \end{bmatrix} = \frac{1}{h} \begin{bmatrix} -2.5u_1 + 2u_2 + 0.5u_3 \\ \vdots \\ 3u_{i+1} - 3u_{i-1} \\ \vdots \\ -0.5u_{N-2} - 2u_{N-1} + 2.5u_N \end{bmatrix}, \tag{3.43}$$

where N is the total number of grids. The second order spatial derivatives are approximated by

$$\begin{bmatrix} 1 & 11 & & & & \\ & \ddots & & & & \\ & 1 & 10 & 1 & & \\ & & & \ddots & & \\ & & & 2 & 1 \end{bmatrix} \begin{bmatrix} u_1'' \\ \vdots \\ u_i'' \\ \vdots \\ u_N'' \end{bmatrix} = \frac{1}{h^2} \begin{bmatrix} 13u_1 - 27u_2 + 15u_3 - u_4 \\ \vdots \\ 12u_{i+1} - 24u_i + 12u_{i-1} \\ \vdots \\ -u_{N-3} + 15u_{N-2} - 27u_{N-1} + 13u_N \end{bmatrix} \tag{3.44}$$

It is worth noting that as an implicit method, the compact difference method involves the solutions of linear equations, which may affect the computational efficiency. Generally speaking, the efficiency of solving a linear equations system **AX**=**B** depends of the structure of the coefficient matrix A, such as its bandwidth, sparsity and stiffness. Numerical experiments have shown that the computational efficiency is improved significantly for the tri-diagonal coefficient matrices in Equations 3.43 and 3.44 [Ai, 2004].

3.3.2 Combined Runge-Kutta and fractional step method

It has been described in the last section that the high order finite difference scheme is used to discretize the governing equations spatially. In the present numerical model, time integration is carried out by using the method of the combined Runge-Kutta and fractional step, as presented by Le and Moin [1991]. The method is based on the predictor-corrector algorithm, which is one of the Runge-Kutta methods. In this method, each time step is divided into three sub-steps. At each sub-step, the KM time-splitting scheme developed by Kim and Moin [1985] is used.

The three-step time advancing techniques for the governing equations given in Equations 3.1-3.4 are written as

$$\frac{\delta u_i^k}{\delta x_i} = 0, \tag{3.45}$$

$$\frac{u_i^k - u_i^{k-1}}{\Delta t} = \alpha_k \left(\frac{\delta^2 u_i^{k-1}}{\delta x_j \delta x_j} - u_j^{k-1} \frac{\delta u_i^{k-1}}{\delta x_j} - \frac{\delta p^{k-1}}{\delta x_i} + f_i^{k-1} \right), \tag{3.46}$$

$$\frac{T^k - T^{k-1}}{\Delta t} = \beta_k \left(\frac{1}{\mathrm{Pr}} \frac{\delta^2 T^{k-1}}{\delta x_j \delta x_j} - u_j \frac{\delta T^{k-1}}{\delta x_j} + Q^{k-1} \right), \tag{3.47}$$

where k=1, 2, 3 denotes the three sub-step, and $\frac{\delta(\cdot)}{\delta(\cdot)}$ represents the finite difference operator that obtained using the high order compact difference method presented in the last section. The coefficients α_k and β_k are selected so that the accuracy of the time integration scheme is of third order. The following values are used in the present numerical model [Ai, 2004]:

$$\alpha_1 = \beta_1 = \frac{1}{3} \tag{3.48}$$

$$\alpha_2 = \beta_2 = \frac{1}{2} \tag{3.49}$$

$$\alpha_3 = \beta_3 = 1 \tag{3.50}$$

At each sub-step, the time integrations are carried out explicitly and the overall time scheme has a third order accuracy. The numerical stability limit of this scheme is determined by [Le and Moin, 1991]

$$\Delta t\left(\frac{\max|u_i|}{\Delta x_i}\right)\leq\sqrt{3}\,. \tag{3.51}$$

Applying the KM fractional step to Equation 3.46, the following equations are obtained

$$\frac{u_i^k-\widetilde{u}_i^k}{\Delta t}=-\frac{\delta p^k}{\delta x_i}\,, \tag{3.52}$$

$$\frac{\widetilde{u}_i^k-u_i^{k-1}}{\Delta t}=\frac{\delta^2 u_i^{k-1}}{\delta x_j\delta x_j}-u_j^{k-1}\frac{\delta u_i^{k-1}}{\delta x_j}+f_i^{k-1}\,, \tag{3.53}$$

where $\widetilde{u}_i^k$ is intermediate velocity field.

Equations 3.45 and 3.52 are combined to obtain the Poisson equation

$$\frac{1}{\Delta t}\frac{\delta\widetilde{u}_i^k}{\delta x_i}=\frac{\delta^2 p^k}{\delta x_i\delta x_i}\,. \tag{3.54}$$

Finally, the procedures of numerical solution of the governing equations presented in this section are summarized as following:

a) Given velocity field u_i^{k-1} and temperature field T^{k-1}, Equation 3.53 is solved for $\widetilde{u}_i^k$;

b) The Poisson equation (Equation 3.54) is solved for p^k;

c) The velocity field at sub-step *k* is updated using Equation 3.52;

d) If k=3, u_i^k is updated as the velocity field at time step *n*+1. Otherwise, the sub-step time is advanced with *k*=*k*+1;

e) Temperature field is updated using Equation 3.47;

f) Go to a) until the calculation is complete.

3.3.3 Eigenvalue problem for linear stability analysis

The final perturbation equations given by Equations 3.30-3.34 can be discretized, along with the corresponding boundary conditions given in Equations 3.35-3.41, using the high order compact difference method. The obtained system of algebra equations is cast in the form of an eigenvalue matrix equation as

$$\mathbf{AX} = \varpi \mathbf{BX} \tag{3.55}$$

where **A** and **B** are the coefficient matrices, **X** is an assembling vector the eigenfunction defined as

$$\mathbf{X} = \begin{bmatrix} \hat{U}_r \\ \hat{U}_\theta \\ \hat{U}_z \\ \hat{T} \\ \hat{P} \end{bmatrix}, \tag{3.56}$$

and ω is the eigenvalue need to be solved.

In general, the eigenvalue ω of the eigenvalue problem may be either real values or complex conjugate pairs. To locate the threshold at which the flow becomes unstable, the most dangerous mode, which is the eigenvalue with the maximum real part, needs to be identified.

In the present study, the Arnoldi's method with linear fractional transformation is used to solve the eigenvalue problem given by Equation 3.55. It is well known that the Arnordi's method can only be used for the eigenvalue problems with a large module [Arnodi, 1951; Saad, 1980]. In order to find the eigenvalues with large real parts, where at least the leading eigenvalue with a largest real part included, Nayar and Ortega [1993] have shown that a simple eigenspectrum transformation technique can be used to transfer the eigenspectrum into the proper one. The linear fractional transformation is one of the most widely used spectrum transformation technique in engineering computations and is used in the present model as

$$\varpi = \frac{\tau - 1}{\tau + 1}. \tag{3.57}$$

Using Equation 3.57, the ω spectrum is mapped into the τ spectrum with the eigenvalues in the ω plane are transformed into a unit circle in the τ plane. Therefore, it is much easier to use the Arnoldi's method to find the leading eigenvalues with the transformed eigenspectrum.

Applying the fractional transformation given in Equation 3.57 to the eigenvalue problem defined by Equation 3.55, we obtain the following transformed eigenvalue problem,

$$-(\mathbf{A}+\mathbf{B})\mathbf{X} = \tau(\mathbf{A}-\mathbf{B})\mathbf{X}\,. \tag{3.58}$$

Equation 3.58 is further simplified to the following eigenvalue problem to facilitate the application of the Arnoldi's method,

$$(\mathbf{A}-\mathbf{B})\varpi_j = \mathbf{B}\nu_j \tag{3.59}$$

where ϖ_j (j=1, 2, 3…) is the eigenvalue and ϖ_j is the orthogonal basis, which is used in the Arnoldi's iterative method to calculate the eigenvalues and eigenfunctions. In the present numerical model, an LU decomposition of (**A**-**B**) with partial pivoting is used in the Arnoldi iteration.

3.4 Validation of the Numerical Model

In this section, the presented numerical model is validated against previous theoretic and numerical studies on the stability of convective flows in laterally bounded

horizontal liquid layers. Two ideal cases, pure Rayleigh-Bénard convection and pure Marangoni convection induced by vertical temperature gradients in liquid layers confined by cylindrical walls are studied as benchmark tests.

3.4.1 Rayleigh-Bénard convection

Rayleigh-Bénard convection in a vertical cylinder is a classic topic in fluid mechanics. Consider a horizontal layer of fluid confined by a vertical cylindrical wall shown in Figure 3.1. The top and bottom surfaces of the liquid layer are in contact with rigid walls that are kept at different temperatures. The top surface is kept at dimensionless temperature of 0 and the bottom at dimensionless temperature of 1. The sidewall is adiabatic. All solid walls are no-slip.

It is well known that for this case, the stability of the flow is characterized by Rayleigh number defined as

$$\mathrm{Ra} = \frac{\rho g \beta \Delta T}{\mu \kappa}, \tag{3.60}$$

where ΔT is the temperature difference between the top can the bottom. When Ra is small enough, pure conductive and no flow state is possible. When the Rayleigh number reaches certain critical value, convective flow sets in and induced convection becomes the primary heat transfer mechanism between the hot and the cold surfaces. The thermal convection in a vertical cylinder has been studied extensively [Charlson and Sani, 1970a; Charlson and Sani, 1970b; Wanschuar *et al.*, 1996]. Its neutral curves have been well

established. It has been found that the critical Rayleigh number depends on the aspect ratios of the cylinders. The aspect ratio in the present work is defined as

$$\mathrm{A} = \frac{R}{H}. \tag{3.61}$$

One of most widely studied cases is thermal convection in a cylinder with dimensions of R=H=1. The critical Rayleigh number at various azimuthal wave numbers from the present numerical model are compared with those from the Charlson and Sani [1970a, 1970b] and Wanschura *et al.* [1996]'s work in Table 3.1. The most dangerous mode is found to be m=2 by all of the three models. The critical Rayleigh numbers obtained from the present model are with in ± 2% of those of Wanschura *et al.* [1996] and ± 10% of those of Charlson and Sani [1970a and 1970b].

The critical Rayleigh numbers are also obtained at various aspect ratios for azimuthal wave number of 1 and 2, which is plotted in Figure 3.2. As expected, the critical Ra decreases as the aspect ratio of the cylinder is increased because the lager aspect ratio decreases the stabilizing effect of the sidewall. As the aspect ratio increases, the critical Ra for both azimuthal wave numbers approach the critical Rayleigh number for an infinite liquid layer, which is 1708 [Drazin and Reid, 1981].

3.4.2 Marangoni convection

The second benchmark test used to validate the present numerical model is the pure Marangoni convection in a vertical cylinder, as shown in Figure 3.3, the geometry is similar to that of Rayleigh-Bénard case except that the top surface is an open free surface

cooled by ambient air according to Newton's cooling law. The effect of the buoyancy is ignored (Ra=0), which means the change of density with temperature is ignored.

For this case, the stability of the surface tension driven flow is characterized by the Marangoni number

$$\mathrm{Ma} = \frac{\gamma \Delta T H}{\mu \kappa}. \tag{3.62}$$

Here ΔT is the temperature difference between the bottom temperature and the average temperature at the top surface. It is assumed that the small perturbation applied to the temperature field does not change the heat loss at the top surface (Bi=0), where Bi is the Biot number at the free surface given by

$$\mathrm{Bi} = \frac{hR}{\kappa}, \tag{3.63}$$

where h is the rate of change of heat transfer coefficient per unit temperature change. For this case, since the imposed temperature gradient is perpendicular to the free surface, a quiescent base state is possible if Marangoni number is small enough. When Marangoni number is greater than certain threshold, convective flow induced by the Marangoni effect sets in. The Critical Marangoni numbers obtained using the present model are compared with those from Dauby, *et al*. [1997] for a cylinder of aspect ratio of 1 in Table 3.2. As shown in the table, the present model is in good agreement with Dauby *et al*'s [1997] results.

The critical Marangoni numbers for m=1 and m=2 at various aspect ratios are shown in Figure 3.4. As the aspect ratio is increased, the sidewall effects decrease and therefore, the critical Marangoni number decreases and approaches the theoretic prediction of that for an unbounded layer of fluid. For an infinite horizontal layer of fluid, Pearson [0] obtained the critical Marangoni number of 79.6 when the bottom wall is conducting, i.e., kept at constant temperature. When the aspect ratio of the cylinder is 15, our numerical model gives the critical Marangoni numbers of 80 for both wave numbers. As it is indicated above, good agreement has been achieved between the present numerical model and the previous studies.

Based on the benchmark tests presented in this section, the present numerical model can be used with confident to simulate the convective flow in the material processing systems and study the stability of the flow.

3.5 Results and Discussions

The numerical model presented in the previous sections is used to investigate the Rayleigh-Bénard-Marangoni convection in the Czochralski crucibles. The geometric and physical configurations of the crucible under investigation are shown in Figure 2.1. The stability of the convective flow in the Czochralski crucibles is governed by the Grashof number given in Equation 2.11 and the Marangoni-Reynolds number given in Equation 2.18. In this section, the critical Grashof numbers are determined at various Marangoni-Reynolds numbers to reveal how the thermocapillary effect interacts with the Bénard effect under various boundary conditions.

3.5.1 Mesh dependency test

Before any simulation results are presented, a mesh dependency test is carried out to determine the mesh to be used in the present study. For the axisymmetric base flow, simulations were carried out for a cylinder of $R=H=1$ with $\mathrm{Re}_\gamma=10^4$ and $\mathrm{Gr}=2\times10^5$. The velocities at $r=z=0.6$ calculated using various uniform meshes are listed in Table 3.3. A uniform grid with 26 nodes in both r and z directions ($N_r=N_z=26$) is chosen to be used in simulation. Any further refinement will result in less than 2% error in base flow simulation.

It is worth noting that the critical state is determined by the real part of the leading eigenvalue. For the melt flow in a cylinder of $R=H=1$ with $\mathrm{Re}_\gamma=0$ and $\mathrm{Gr}=2\times10^5$ the maximum growth rates obtained using various uniform meshes are list in Table 3.4. For a tradeoff between computational accuracy and optimal computing time, a mesh with 26 uniformly spaced nodes in both r and z directions is used for the stability results presented in this chapter, which is shown in Figure 3.5. Further refinement of the mesh produces results with an uncertainty of less that 4%.

Other physical and geometrical properties used for the computation are listed in Table 3.5.

3.5.2 Base flow pattern

Typical flow patterns and isothermals for axisymmetric base flow in a cylinder of $R=H=1$ using the properties listed in Table 3.5 are presented in this section. Dimensionless time step used for the simulations is 10^{-6}, unless convergence required smaller time step. The convergence is claimed when the maximum difference of local velocity components and temperature between two time steps is less than 10^{-8}.

Figure 3.6 shows the base flow when $Re_\gamma=10^4$, $Gr=10^6$, and $R_d=0$. The fluid is heated through the sidewall and cooled at the free surface by radiation. A convective loop is formed with the fluid flowing upwards near the vertical wall and downwards at the center due to the heating at the lateral wall (Bénard effect). A small recirculation loop can be observed near the upper right corner of Figure 3.6(a). The flow pattern is similar to the first type of base flow observed by Hoyas *et al.* [2002]. Along the free surface, the fluid temperature is higher near the sidewall and lower at the center. Marangoni flow from the sidewall towards the center is driven by the temperature gradient. The fluid at the top surface is cooled only by radiation and therefore the temperature gradient imposed along it is small. As a result, the Marangoni flow induced along the free surface is weak.

Simulation is carried out at higher Marangoni-Reynolds numbers to show how the Marangoni effect may change the base flow patter. Figure 3.7 presents the isothermal and the velocity vectors for the axisymmetric base flow when $Re_\gamma=10^5$, $Gr=10^6$, and $R_d=0$. Due to the higher Re_γ, stronger Marangoni flow is induced along the free surface. However, the stronger Marangoni flow does not change the bulk flow structure. Comparing Figures 3.6(b) and 3.7(b), smaller temperature gradient along the free surface is observed at the higher Re_γ. This is caused by the higher heat transfer rate resulted from the stronger Marangoni flow.

Figure 3.8 shows the base flow structure and temperature field with the presence of a seeding crystal. When a seeding crystal of $R_d=0.5$ is in contact with the top surface, the top surface is cooled by both the radiation and conduction. A strong temperature gradient is imposed at the edge of the crystal and therefore strong Marangoni flow is

induced, see Figure 3.8(a). The strong Marangoni flow changes the flow pattern near the top surface dramatically. However, it does not have a strong effect on the bulk flow structure, of which a big convective loop similar to those in Figures 3.6 and 3.7 is observed. It is found that the temperature distributions are more uniform than those obtain for higher Prandtl number fluids [Jing, *et al.*, 1999]. This is caused by the large thermal conductivity of the low Prandtl number fluid (liquid metal) used in the present study.

3.5.3 Rayleigh-Bénard-Marangoni stability of the base flow

In this section, a linear stability analysis of the axisymmetric base flow given in the previous section is presented. As it has been demonstrated, the stability of the base flow is characterized by the Marangoni-Reynolds number and the Grashof number. The results shown in this section are focused on the interaction between the two effects and how the physical boundary conditions may change the stability of the Rayleigh-Bénard-Marangoni convection.

The stability analysis was carried out at three Re_γ values, 0, 5000, and 10000, respectively. For each given Re_γ number, the base flow is axisymmetric when the Grashof number small enough. The flow loses its axisymmetry eventually as Gr is increased. In the present stability analysis, for each given Re_γ value, simulations were conducted as different Grashof number to locate the critical Gr at which the real part of the leading eigenvalue vanishes. Gr was updated using bisection method. The critical Grashof number depends on Marangoni-Reynolds number, Re_γ, and the azimuthal wave number, m. For laterally bounded liquid layers in cylindrical configurations, the continuous wave number is replaced by discrete azimuthal modes [Johnson and

Narayanan, 1999]. The present study is focused on the axisymmetry-breaking instabilities and the critical Grashof numbers are presented for azimuthal wave number from 1 up to 10.

Figure 3.9 shows the stability curves obtained for a cylinder of R=H=1 with R_d=0. At all three Re_γ values, the most dangerous azimuthal mode is found to be 1. For Re_γ=0, the critical Gr is found to be 190215 while for Re_γ=10000 it is found to be 281224. The critical Gr increases as Re_γ is increased because of the stabilizing effect of the surface tension.

When a seeding crystal of R_d=0.5 presents, neutral curves at the three Re_γ numbers are depicted in Figure 3.10. The most dangerous azimuthal mode for this case is also found to be 1. For this case, the critical Grashof number is creased from 326957 to 571182 when Re_γ is increased from 0 to 10000. When Re_γ=10000, the critical Grashof number of 571182 is higher than that of 281224 for the R_d=0 case. This increase in critical Grashof is not surprising considering the fact that the seeding crystal imposes a solid boundary at the free surface. The solid boundaries always stabilize the convective flow.

The typical eigenvalue spectrum of the flow under investigation is shown in Figure 3.11. A *T*-shape eigenvalue spectrum is observed. The figure shows that both real and complex growth rate are possible. The complex growth rate always occurs in conjugate pairs. The first five leading eigenvalues for R=H=1, $\mathrm{Gr}_{\mathrm{cr}}$= 281224, Re_γ=10^4, m=1, and R_d=0 are listed in Table 3.6. As shown in the table, the first leading eigenvalue is a real number, which is zero, and the following four leading eigenvalues are all conjugate pairs. This indicates that the first leading eigenvalue mode is a stationary

mode and the following four modes are HOPF modes [Ding and Kawahara, 1998]. Similar structure of the leading eigenvalues spectrum is also observed for the unstable base flow at Gr=281230 in Table 3.7.

To further illustrate the instability mechanism of the convective flow, temporal evolution of the perturbation energy is analysis. In the present study, following the definition presented by Ding and Kawahara, [1998], the perturbation energy can be calculated as

$$e = \frac{1}{2}\left(U_r'^2 + U_z'^2 + U_\theta'^2\right). \tag{3.64}$$

The evolutions of the total perturbation energy in the axisymmetric plane of θ=0 for the first two leading eigenvalues are plotted for two base flows, Gr=281224 and 281230, in Figures 3.12 and 3.13, respectively. Figure 3.12 shows the transient perturbation energy for the critical state at Gr_{cr}= 281224. The perturbation energy of the first leading eigenvalue decreases monotonically as time is increased (Figure 3.12a). This monotonic profile confirms the *T*-shape eigenvalue spectrum shown in Figure 3.11, in which the leading eigenvalue appears to be a real number (ω_i=0). As listed in Table 3.6, the second leading eigenvalue is a pair of conjugate complex numbers. The perturbation energy corresponding to this eigenvalue osculates at a frequency of ω_i, which is shown in Figure 3.12(b). Figure 3.13 shows the temporal evolution the perturbation energy corresponding to the first two leading eigenvalues for an unstable base flow at Gr=281230. For this case, the perturbation energy of the leading eigenvalue increases monotonically, which confirms that the base flow is unstable. An oscillatory second leading eigenvalue

perturbation energy profile similar to that for the critical case is observed in Figure 3.13(b).

The evolution of the combined perturbation energy for the first five leading eigenvalues at the critical state and the unstable base flow are shown in Figures 3.14 and 3.15, respectively. The combined perturbation energy of the critical state shown in Figure 3.14 oscillates as the dimensionless time is increased. It is obvious that the perturbation energy decays eventually and approaches zero if given enough time. The vanishing perturbation energy implies the perturbations to all the velocity components approach zero. Therefore, the flow at the critical state is stable. For the unstable base flow at Gr=281230, the combined perturbation energy is increased while oscillating, Figure 3.15. It is obvious that the perturbation energy grows infinitely as time increases, which implies that the base flow is unstable when subjected to small perturbation. The stationary mode for the leading eigenvalue and the HOPF mode for the second leading eigenvalue combine into a HOPF mode.

Contours of the temperature and energy perturbations for the leading eigenvalue at the critical state within the free surface are shown in Figure 3.16. The perturbation pattern consists of a pair of maxima and minima along the azimuthal direction, which is corresponding to m=1 [Rubinov, *et al.*, 2004]. It is worth noting that the perturbation is asymmetric while the base flow is axisymmetric. The perturbations are plotted at two moments, $t=2.5\times10^{-8}$ and $t=5\times10^{-8}$, respectively. The perturbation contours do not change significantly as time proceeds, which confirms that the leading eigenvalue is stationary mode.

Based on linear stability theories, the three-dimensional velocity fields corresponding to the critical state can be constructed on the basis of the two-dimensional steady flow with an arbitrary number of disturbance eigenvectors [Ding and Kawahara, 1998]. In the present study, considering the fact that the eigenvalues are either real numbers or conjugate complex pairs, the three-dimensional velocity fields at the critical state are constructed using the leading eigenvalue. Figure 3.17 shows the produced 3-D flow structure and the flow pattern along the free surface. The 3-D flow consists of two co-rotating along the azimuthal directions, which is corresponding to the most dangerous mode of 1.

3.6 Summary

This chapter presents a numerical study on Rayleigh-Bénard-Marangoni stability of low Prandtl number fluid contained in the Czochralski crucibles. The fluid is heated through the sidewall at constant heat flux and cooled at the free surface via radiation. The axisymmetric base flow is solved using high order finite difference method. Small perturbations are applied to the base flow with assumption of slight compressibility. The final perturbation equations are projected into eigenvalue matrix equation and solved by linear fractional transformation. The numerical model is compared with previous numerical studies for pure Rayleigh-Bénard convection and pure Marangoni convection. Good agreements between the present model and the previous studies have been achieved. Critical Grashof numbers are determined as various Marangoni Reynolds numbers and it is found that the surface tension stabilize the buoyancy driven convection. Neutral curves are also determined at different seeding crystal size and it is found the big crystal helps to delay the occurrence of asymmetric flow. The most dangerous azimuthal

mode for all the cases is found to be 1. The instability mechanism of the convective flow is also discussed in this chapter.

m	This model	Charlson&Sani [1970a & 1970b]	Wanschura *et al.* [1996]
1	2914	3164	2875
2	2514	2687	2500
3	3342		
4	4952		

Table 3.1 Comparison of critical Rayleigh numbers at various azimuthal wave numbers between our results and those of Charlson and Sani [1970a and 1970b] and Wanschura *et al.* [1996].

m	This model	Dauby *et al.* [1997]
0	169	163.57
1	122	109.08
2	162	160.15
3	261	257.86

Table 3.2 Comparison of critical Marangoni numbers at various azimuthal wave numbers between our results and those of Dauby *et al.* [1997].

N_r	N_z	Velocity
6	6	181.6308
11	11	193.8589
16	16	205.9079
21	21	213.2608
26	26	217.0745
31	31	218.7899
36	36	219.6557
41	41	220.1121
46	46	220.3805
51	51	220.6079
56	56	220.7098

Table 3.3 Calculated velocity at r=z=0.6 calculated using different uniform meshes for a crucible of R= H=1 with Gr=2×10^5, and Re_γ=10^4.

$N_r \times N_z$	Maximum Growth Rate, ω_r
16×16	-4.0379
21×21	-3.8788
26×26	-3.8049
31×31	-3.7551
36×36	-3.7188
41×41	-3.6909
46×46	-3.6685
51×51	-3.6500

Table 3.4 Maximum growth rate obtained for R=H=1, Re_γ=0, Gr=20000, and m=1, using different meshes.

Parameter	Value
Aspect ratio (R/H)	1.0
Pr	0.02
q	1.0
Rad	1.0
T_{amb}	0.0
T_d	0.0

Table 3.5 Parameters used in calculation.

No.	ω_r	ω_i
1	$-3.157085111904772\times10^{-4}$	$-6.642212192579442\times10^{-8}$
2	-74.8454058930482	±5325219.39924455
3	-96.7482798640753	±1841190.83924748
4	-97.0663118926350	±8505315.86795420
5	-100.662323779148	±428.406090965200

Table 3.6 First five leading eigenvalues at R=H=1, Gr_{cr}= 281224, $Re_{\gamma}=10^4$, m=1, q=1.0, and R_d=0.

No.	ω_r	ω_i
1	$5.054353367751870E\times10^{-3}$	$2.848402098983551E\times10^{-7}$
2	-74.8454014070957	±5325219.39924559
3	-96.7482489277609	±1841190.83924778
4	-97.0662481989712	±8505315.86797078
5	-100.663188364045	±428.414857056436

Table 3.7 First five leading eigenvalues at R=H=1, Gr_{cr}= 281230, $Re_{\gamma}=10^4$, m=1, q=1.0, and R_d=0.

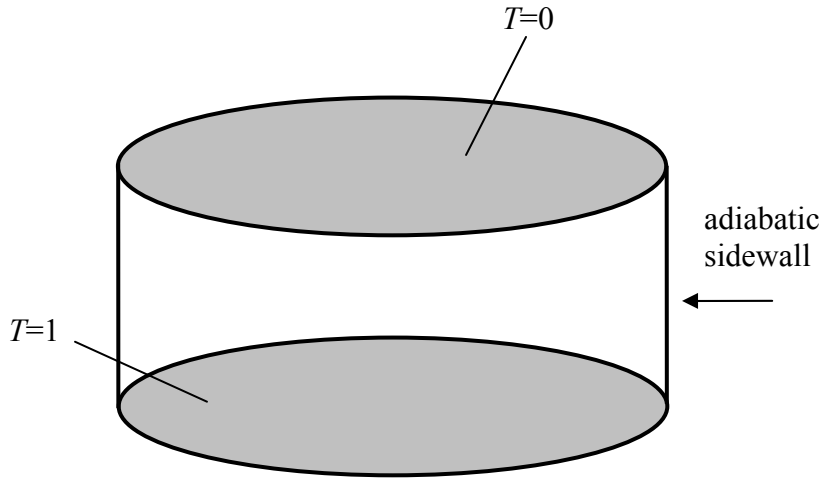

Figure 3.1 Physical configurations of Rayleigh-Bénard convection in a vertical cylinder.

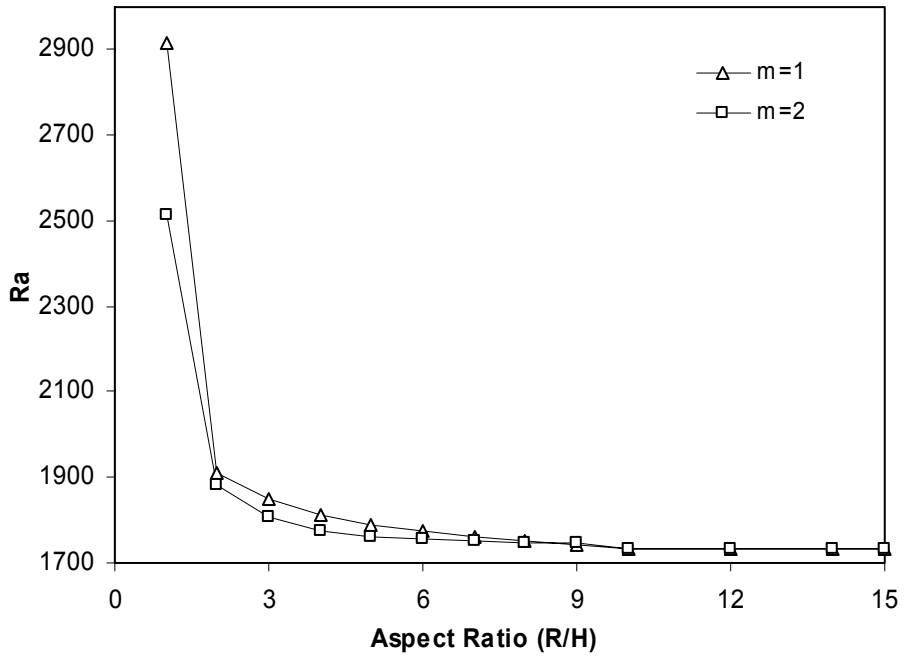

Figure 3.2 Critical Rayleigh number of Rayleigh-Bénard convection in a vertical cylinder for m=1 and m=2 at various aspect ratios.

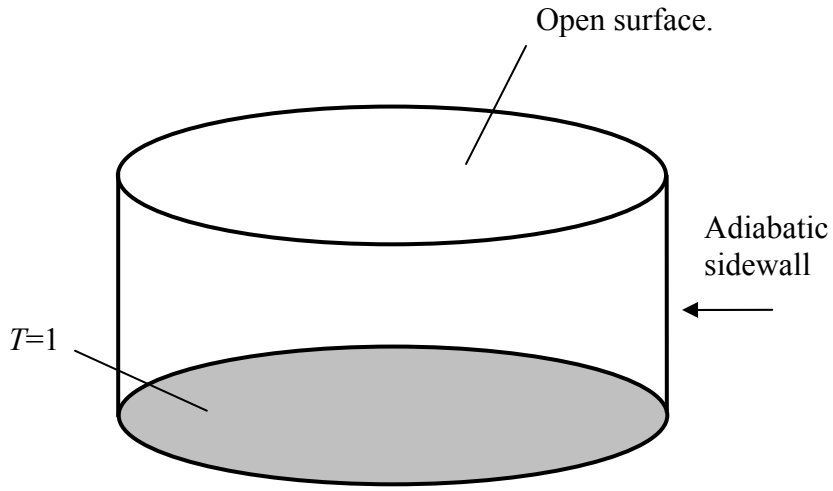

Figure 3.3 Physical configurations of Marangoni convection in vertical cylinders.

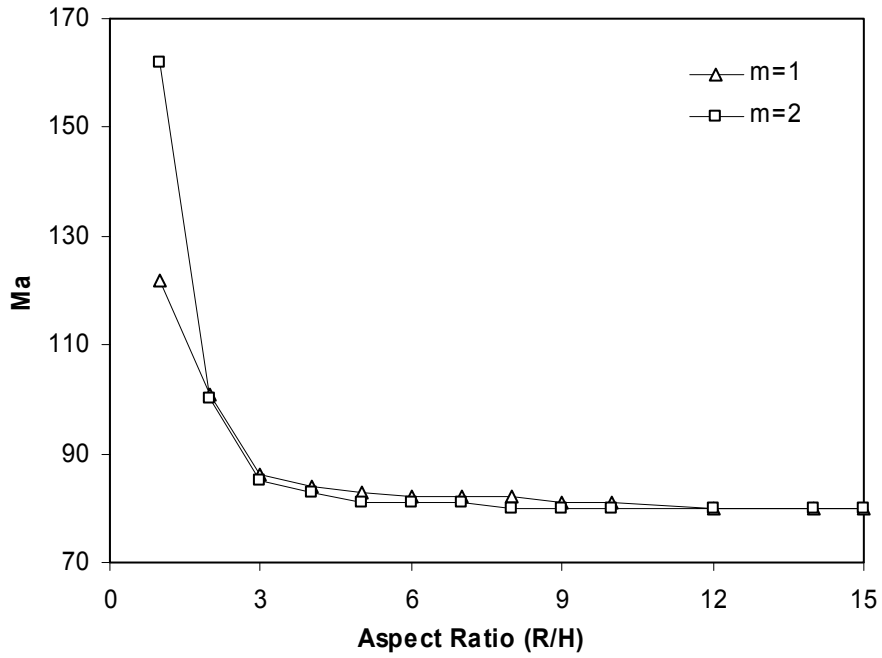

Figure 3.4 Critical Marangoni number of Marangoni convection in a vertical cylinder for m=1 and m=2 at various aspect ratios.

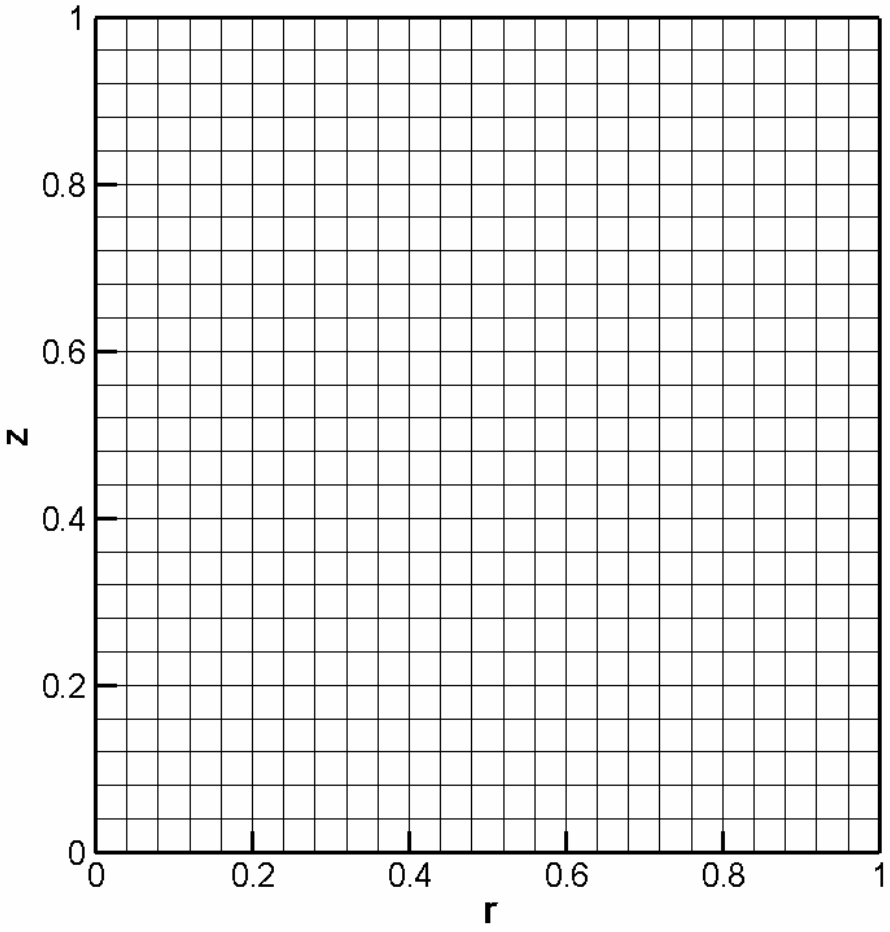

Figure 3.5 Finite difference mesh used for simulation, 26 nodes uniformly spaced along *r* and *z* directions.

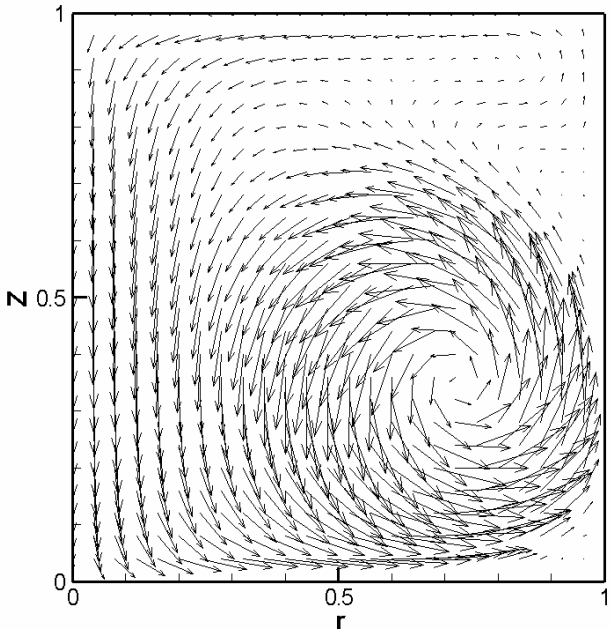

(a)

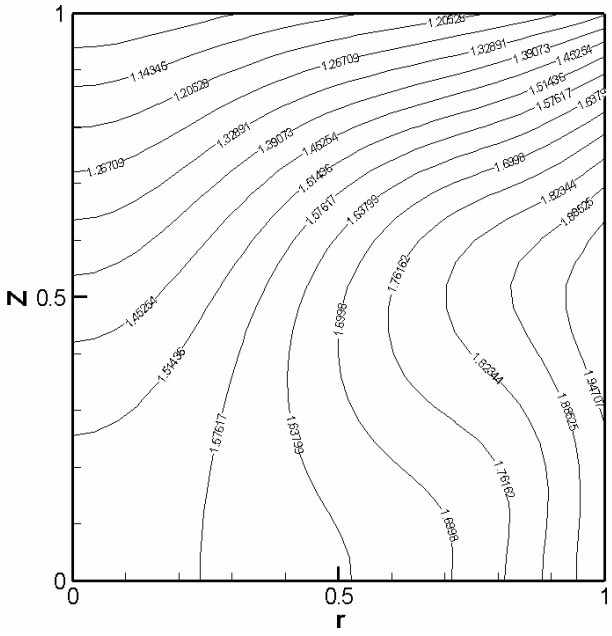

(b)

Figure 3.6 Velocity field (a) and isotherms (b) of the base flow corresponding to R=H=1, $\mathrm{Re}_\gamma=10^4$, $\mathrm{Gr}=10^6$, and R_d=0.

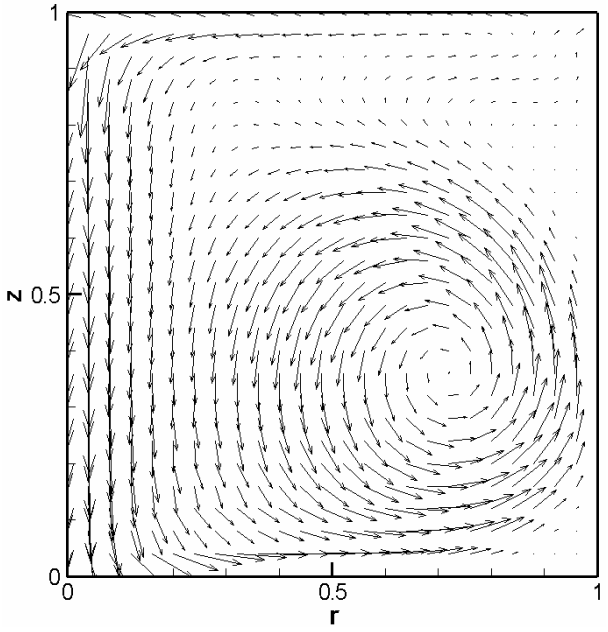

(a)

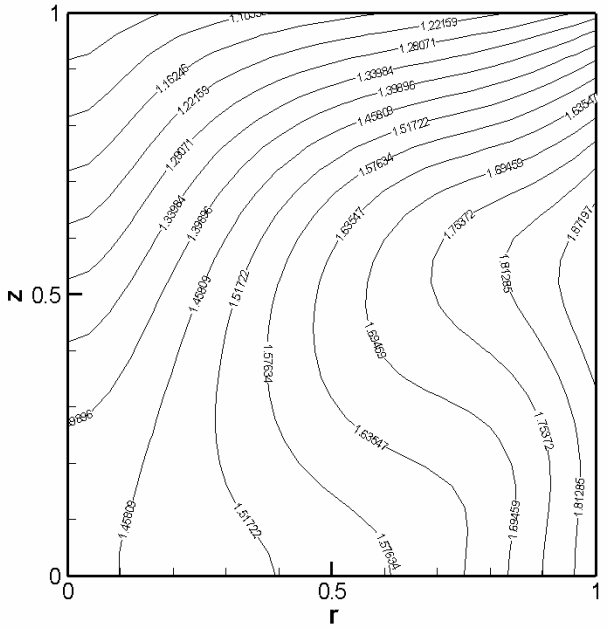

(b)

Figure 3.7 Velocity field (a) and isotherms (b) of the base flow corresponding to R=H=1, $\mathrm{Re}_\gamma=10^5$, $\mathrm{Gr}=10^6$, and R_d=0.

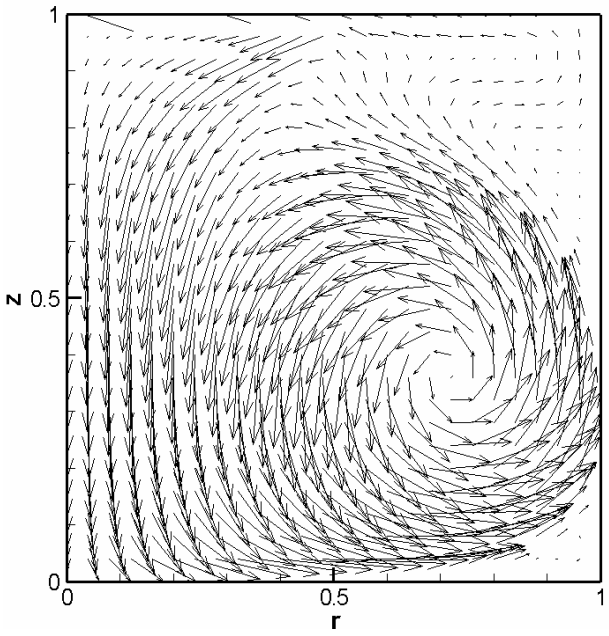

(a)

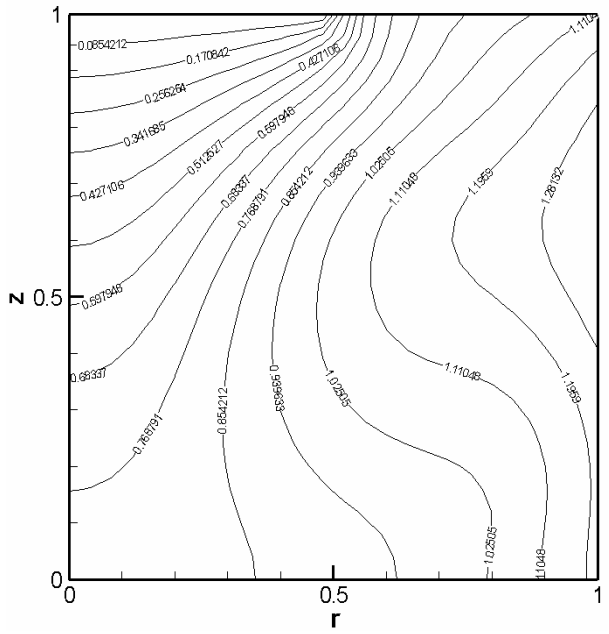

(b)

Figure 3.8 Velocity field (a) and isotherms (b) of the base flow corresponding to R=H=1, $\mathrm{Re}_{\gamma}=10^4$, $\mathrm{Gr}=10^6$, and R_d=0.5.

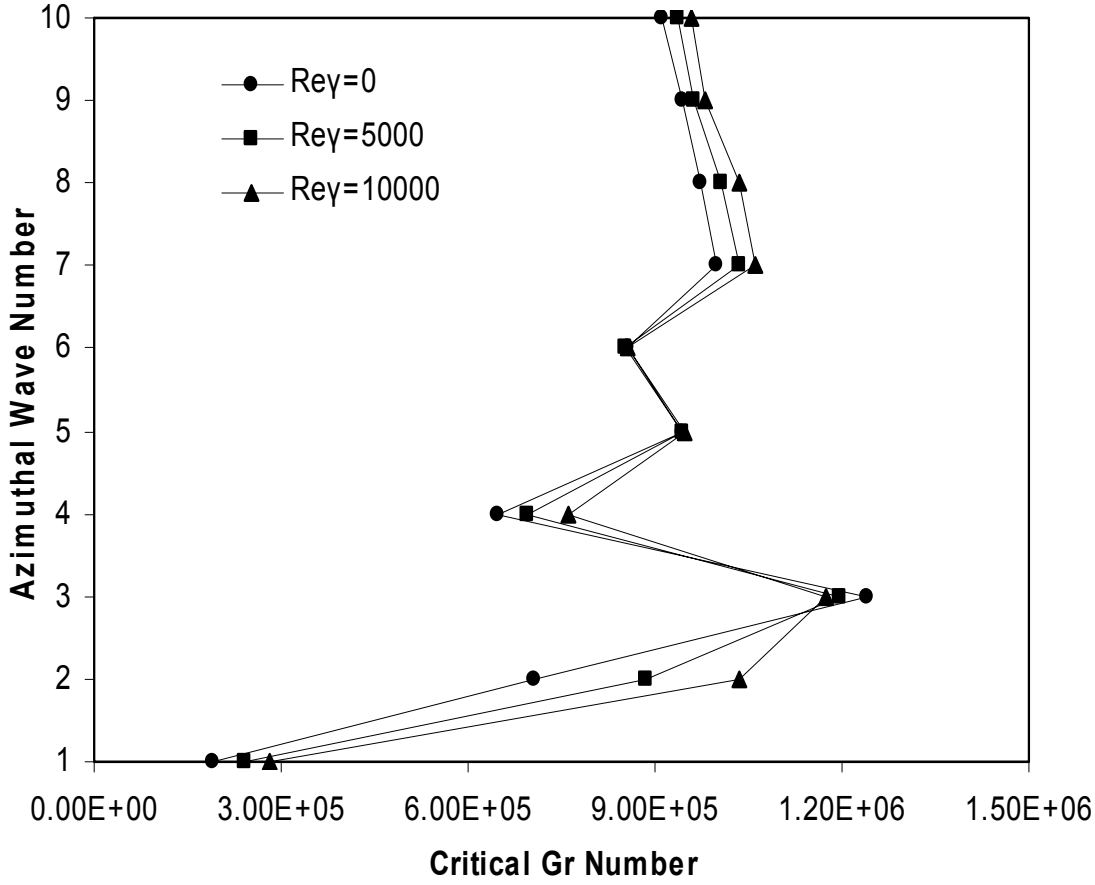

Figure 3.9 Critical Grashof numbers for Re_γ=0, 5000, and 10000 for R=H=1 and R_d=0.

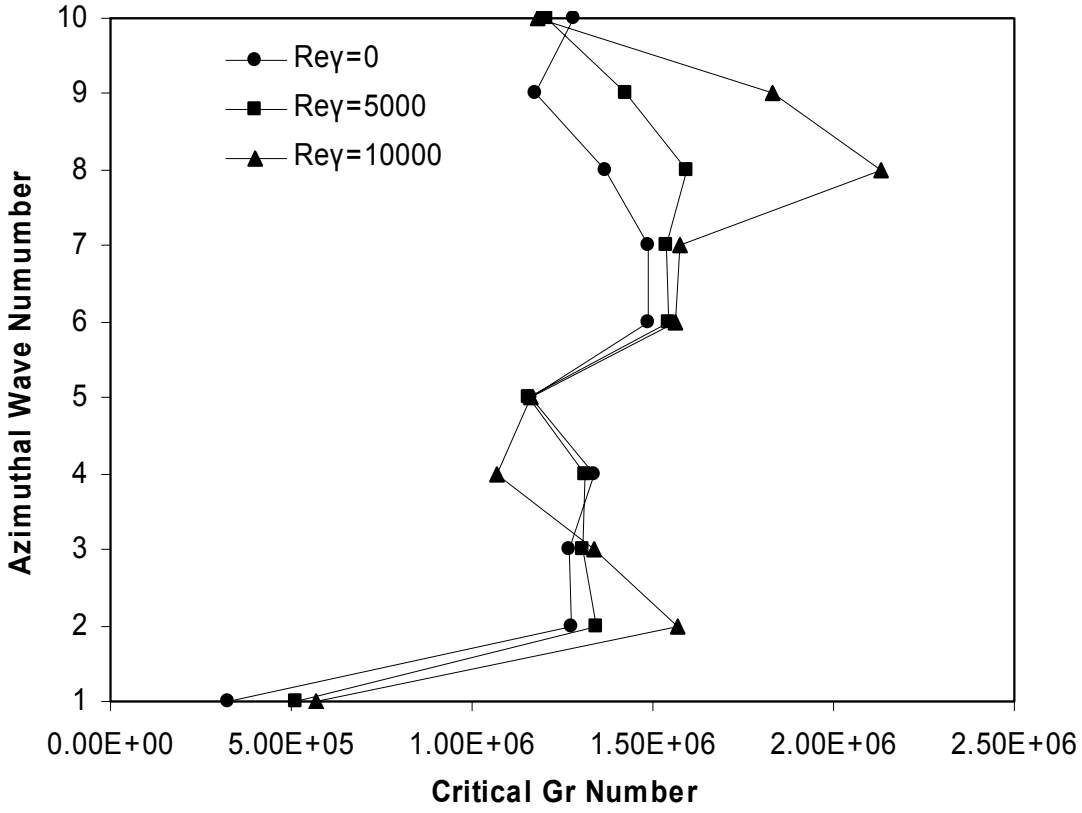

Figure 3.10 Critical Grashof numbers for Re_γ=0, 5000, and 10000 for R=H=1 and R_d=0.5.

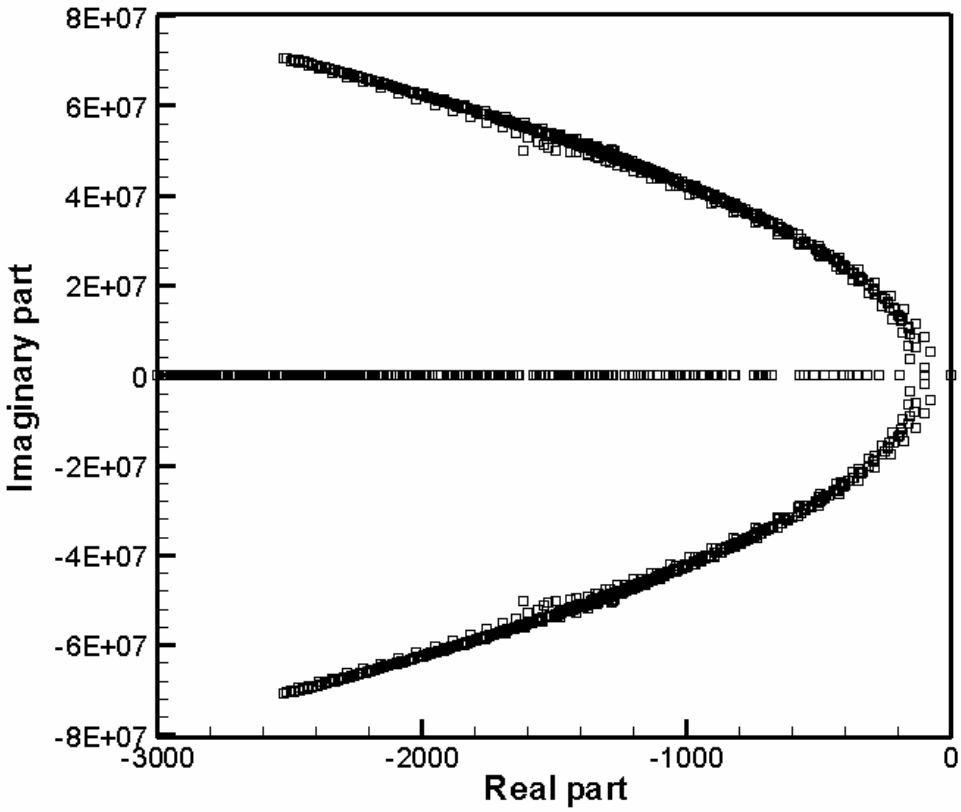

Figure 3.11 Eigenvalue spectrum of critical base flow with R=H=1, Gr_{cr}= 281224, $Re_{\gamma}=10^4$, m=1, q=1.0 and R_d=0.

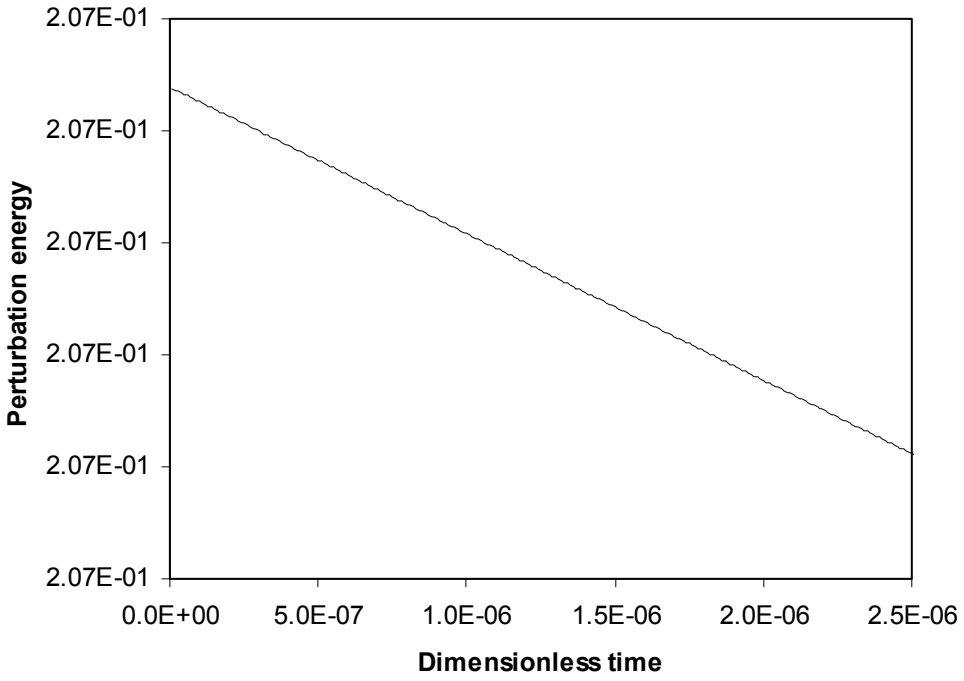

(a)

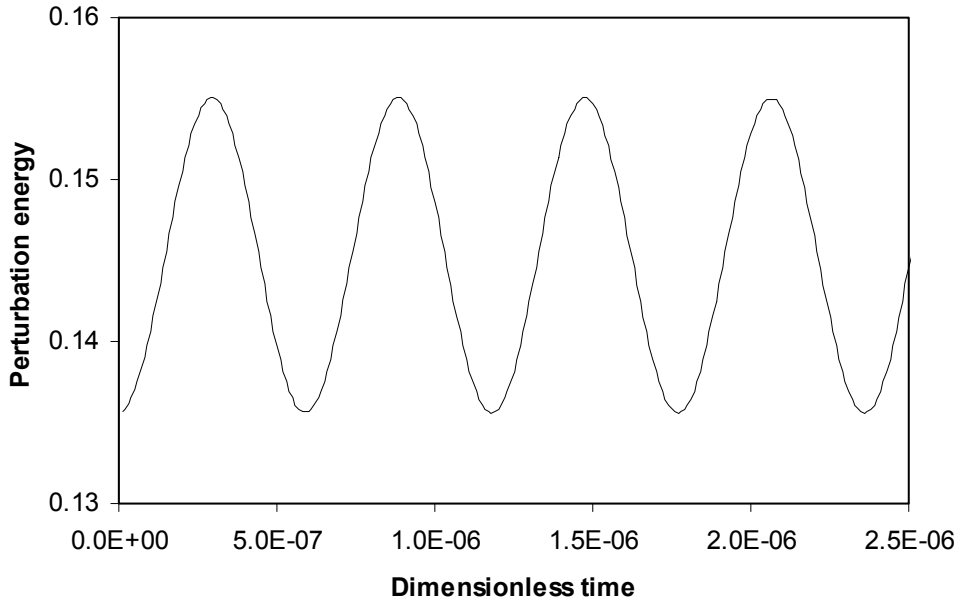

(b)

Figure 3.12 Evolution of perturbation energy in the axisymmetric plane at θ=0 for R=H=1, Gr_{cr}= 281224, Re_{γ}=10^4 and R_d=0: (a) first and (b) second leading eigenvalue.

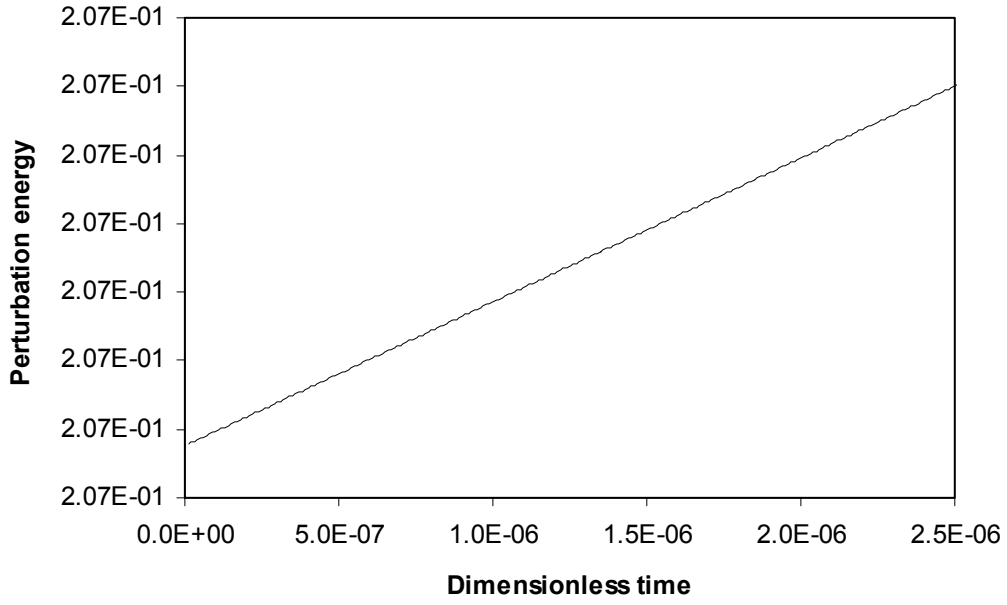

(a)

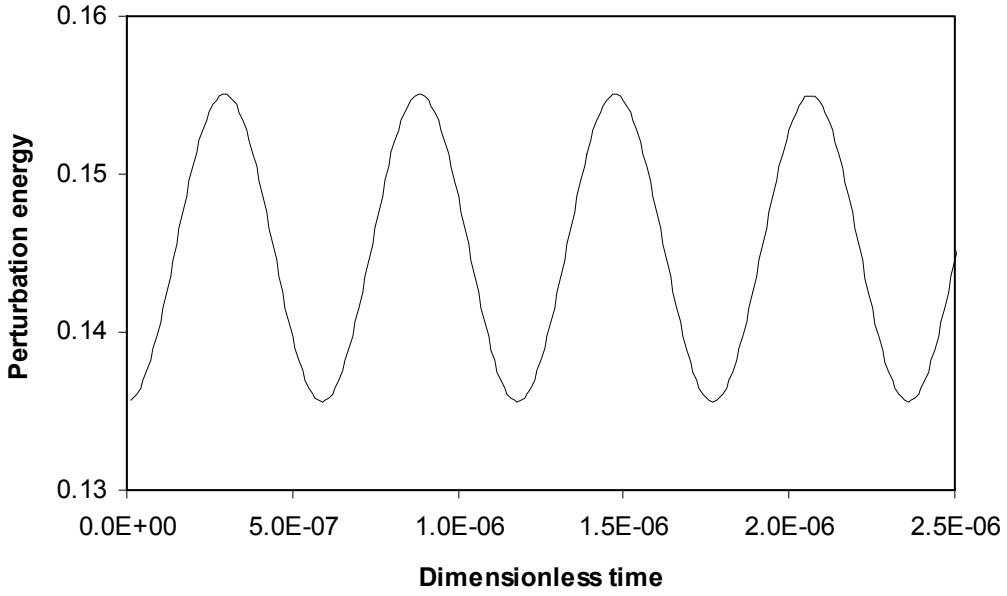

(b)

Figure 3.13 Evolution of perturbation energy in the axisymmetric plane at θ=0 for R=H=1, Gr= 281230, Re_γ=10^4 and R_d=0: (a) first and (b) second leading eigenvalue.

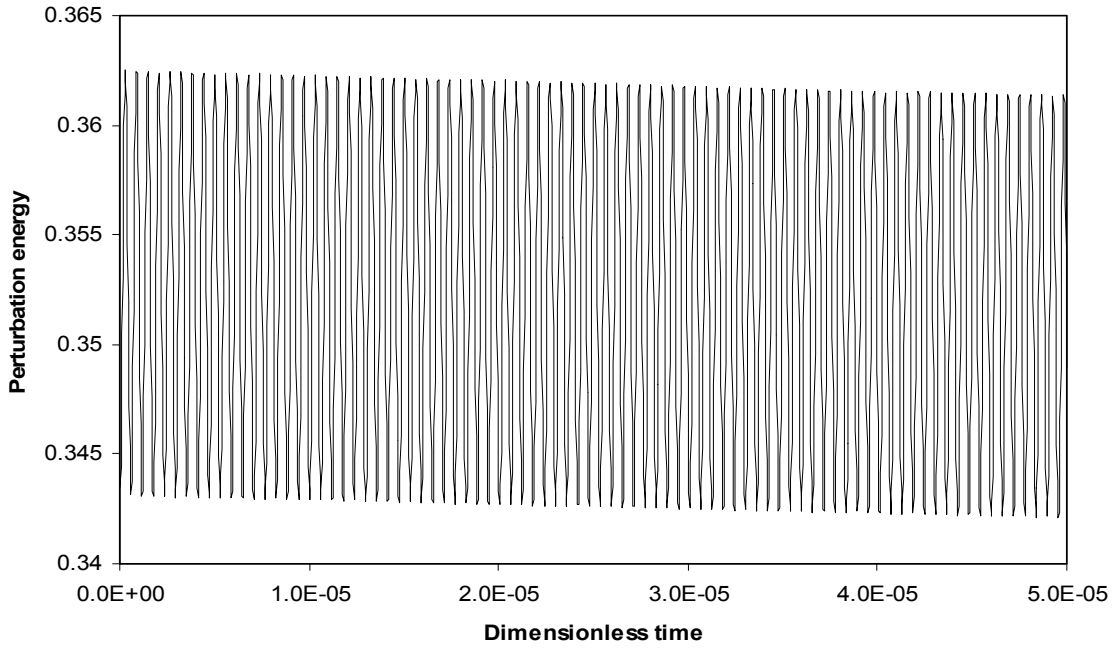

Figure 3.14 Evolution of combined perturbation energy for the first five leading eigenvalues in the axisymmetric plane at θ=0 for R=H=1, Gr= 281224, Re_γ=10^4 and R_d=0.

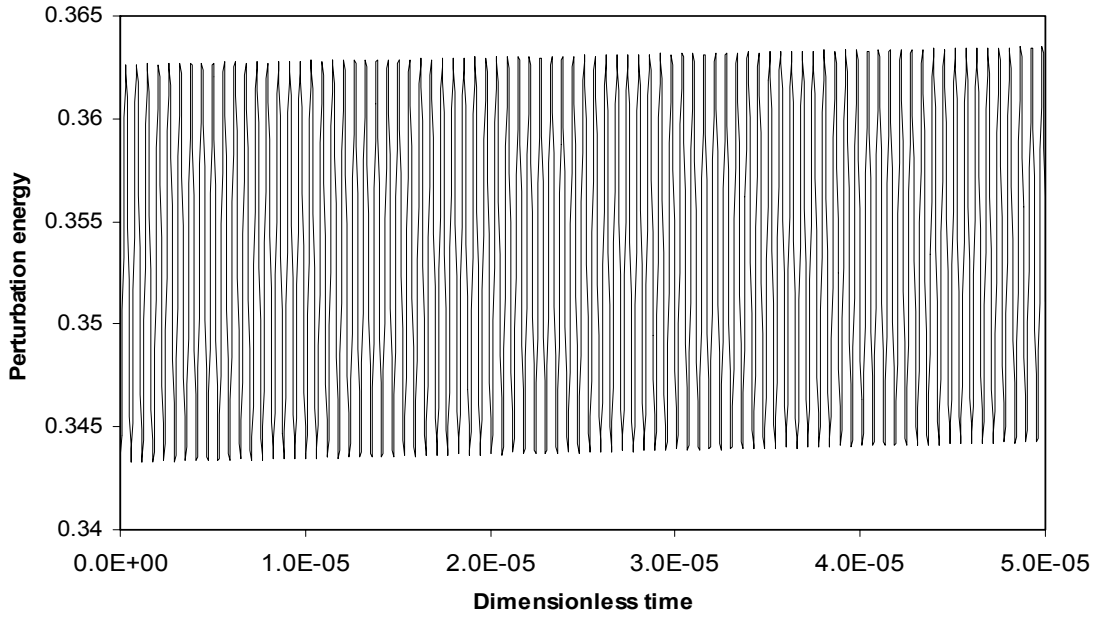

Figure 3.15 Evolution of combined perturbation energy for the first five leading eigenvalues in the axisymmetric plane at θ=0 for R=H=1, Gr= 281230, Re_γ=10^4 and R_d=0.

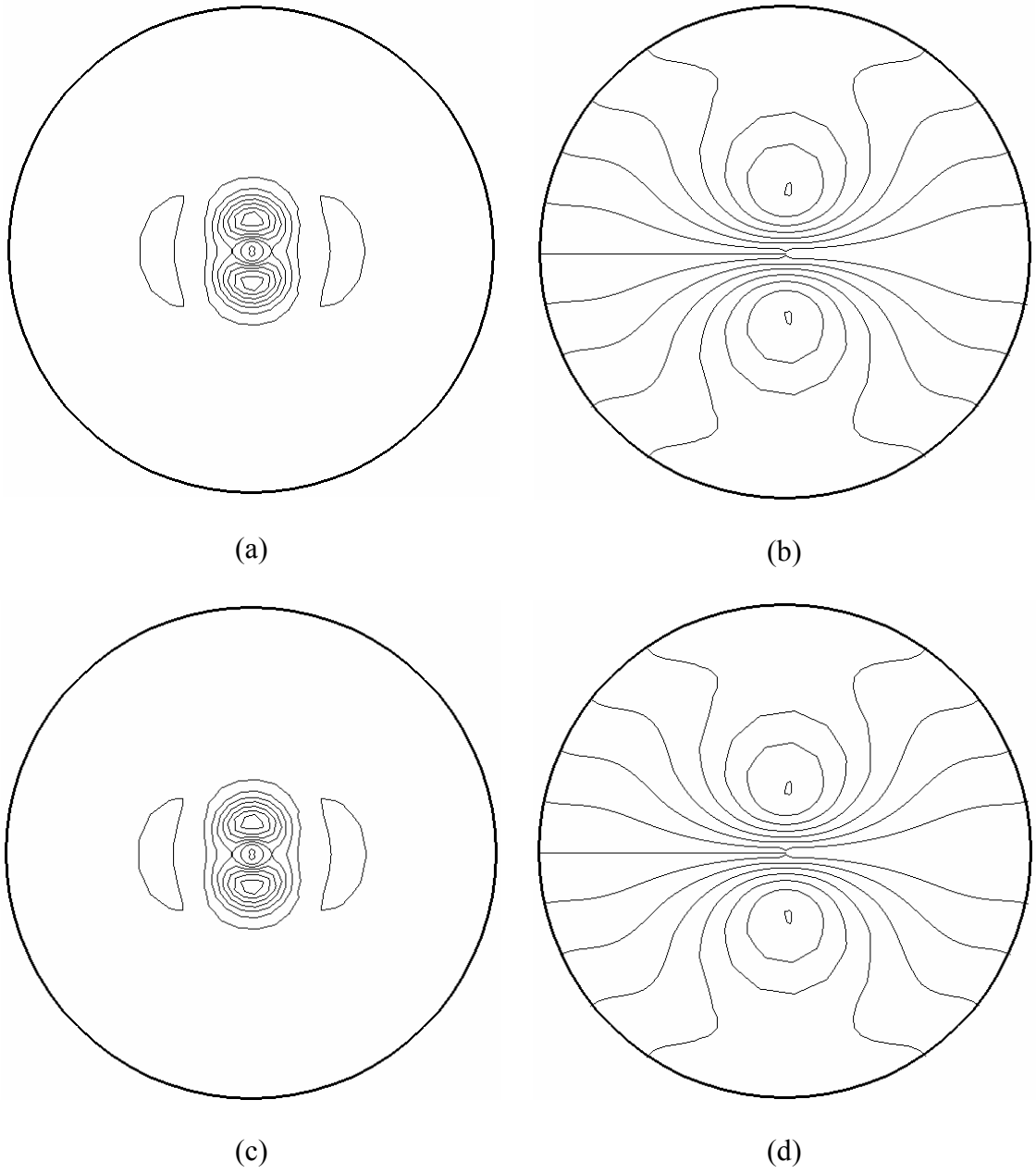

Figure 3.16 Pattern of perturbation of for the leading eigenvalue at the top surface corresponding to R=H=1, $\mathrm{Re}_{\gamma}=10^{4}$, Gr_{cr}=281224 and m=1: (a) energy at $t=2.5\times10^{-8}$; (b) temperature at $t=2.5\times10^{-8}$; (c) energy at $t=5\times10^{-8}$; (d) temperature at $t=5\times10^{-8}$.

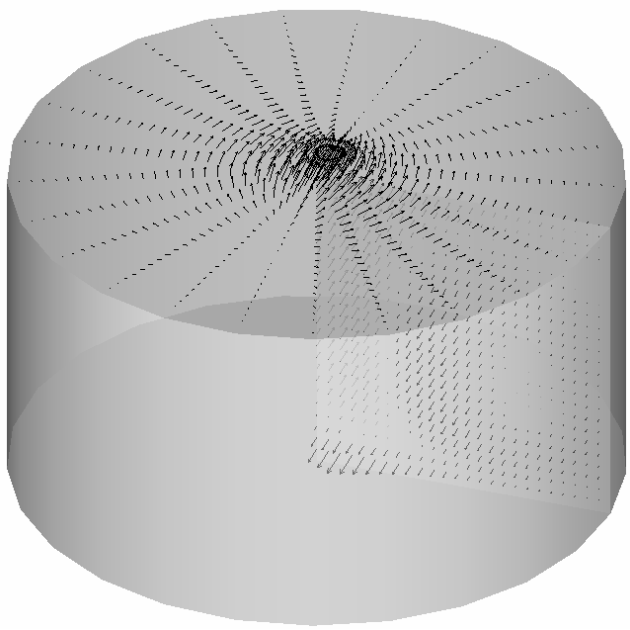

(a)

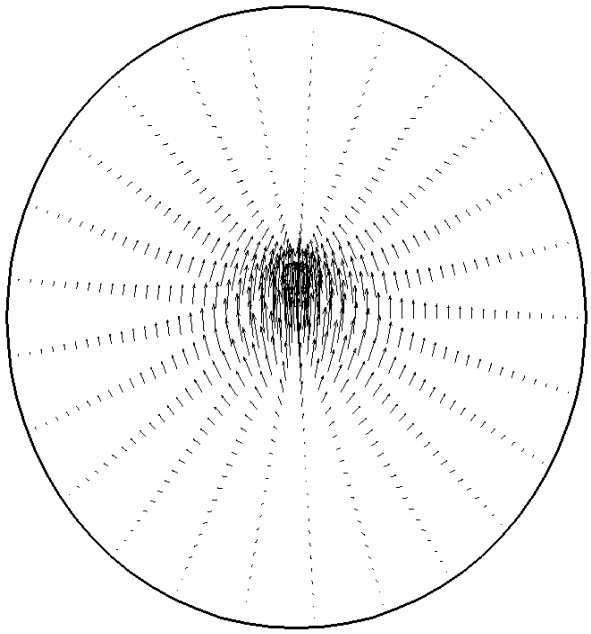

(b)

Figure 3.17 Three-dimensional flow pattern of the leading eigenvalue corresponding to the critical state for R=H=1, R_d=0, Re_γ=10^4, Gr_{cr}=281224 and m=1: (a) 3-D flow structure; (b) top surface flow pattern.

CHAPTER FOUR

NUMERICAL SIMULATION AND STABILITY OF RAYLEIGH-BÉNARD-MARANGONI CONVECTION IN OF RADIATION PARTICIPATING MELTS IN CRYSTAL GROWTH SYSTEMS

This chapter extends the numerical simulations and stability analysis presented in Chapter Three to a radiation participating melt. In the last chapter, the melt was considered transparent, in other words, the melt does not participate in radiative energy transfer. However, it is well known that oxide melts are not opaque to infrared radiation, which implies that the internal radiative energy absorption and emission strongly influence the heat transfer behavior during the crystal growth [Brandon and Derby, 1992; Kobayashi, *et al.*, 1997]. In this chapter, a discontinuous finite element model of internal radiation problem is presented and coupled with the high order difference model presented in the last chapter to solve the flow and temperature fields in the Czochralski crucibles. A linear stability analysis is carried out base on the numerical simulation to investigate how the internal radiation may change the stability diagrams of the melt flow at various radiative boundary conditions.

4.1 Governing Equations for Internal Radiation Problems

Radiative transfer in a participating medium is described by the radiative intensity, which is affected by the interaction between the traveling thermal rays and the medium, which includes emission, absorption and scattering. Radiative intensity is

increased due to absorption and incoming scattering. In the meantime, it is reduced by scattering and emission [Modest, 1993].

4.1.1 Radiative transfer equation

The radiative transfer equation governs the distribution of the radiative intensity $I(\mathbf{r},\mathbf{s})$, sometimes called radiation intensity, which is a function of both coordinates **r** and direction ***s***, see Figure 4.1. The radiative intensity is defined as radiative energy flow per unit solid angle, and unit area normal to the thermal rays. The transfer equation is derived from the local conservation of radiative energy and has the following general form [Seigel and Howell, 1992; Modest, 1993]:

$$\begin{aligned} &\frac{1}{c}\frac{\partial I_\lambda(\mathbf{r},\mathbf{s})}{\partial t}+\frac{\partial I_\lambda(\mathbf{r},\mathbf{s})}{\partial s} \\ &=-\beta_\lambda(\mathbf{r})I_\lambda(\mathbf{r},\mathbf{s})+\kappa_\lambda(\mathbf{r})I_{b\lambda}(\mathbf{r})+\frac{\sigma_\lambda(\mathbf{r})}{4\pi}\int_{4\pi} I_\lambda(\mathbf{r},\mathbf{s}')\Phi(\mathbf{s},\mathbf{s}')d\Omega' \end{aligned} \tag{4.1}$$

where $\beta_\lambda(\mathbf{r})=\kappa_\lambda(\mathbf{r})+\sigma_\lambda(\mathbf{r})$ is the extinction coefficient, $\kappa_\lambda(\mathbf{r})$ is the absorption coefficient, $\sigma_\lambda(\mathbf{r})$ is the scattering coefficient, $\mathbf{s} = \sin\theta\cos\phi\,\hat{i} + \sin\theta\sin\phi\,\hat{j} + \cos\theta\,\hat{k}$, and $\Omega(\mathbf{s})$ is the solid angle associated with direction **s**, where θ and ϕ are the discretization angles used to define the solid angle Ω, see Figure 4.2.

In Equation 4.1, $c = ds/dt$ is the speed at which thermal radiation travels. All the quantities are a function of location in space, time and wave numbers. The intensity and the phase function are also dependent upon directions **s** and **s**′. For many engineering applications, thermal radiation reaches equilibrium far faster than other heat transfer

mechanisms and thus a quasi-steady state approximation is often used. Considering the size of the crucible used in the present study (0.1 m in diameter and 0.05 m in height), the time needed for the radiative energy to travel across the crucible is approximately 3×10^{-9} s. This allows us to drop out the transient term. To facilitate discussion, it is further assumed that all quantities are spectral independent, although the numerical algorithms discussed later in this chapter apply equally to the case where these quantities are spectral dependent as well. With these approximations, Equation 4.1 can be simplified as

$$\frac{\partial I(\mathbf{r},\mathbf{s})}{\partial s} = -\beta(\mathbf{r})I(\mathbf{r},\mathbf{s}) + \kappa(\mathbf{r})I_b(\mathbf{r}) + \frac{\sigma(\mathbf{r})}{4\pi}\int_{4\pi} I(\mathbf{r},\mathbf{s}')\Phi(\mathbf{s},\mathbf{s}')d\Omega' \qquad (4.2)$$

Equation 4.2 is a first order integral-differential equation for the radiative intensity, in which, the first term on the left hand side measures the change in $I(\mathbf{s}, \mathbf{r})$ over a differential distance in the **s** direction, the first term on the right represents the loss to the medium due to absorption or scattering, the second is the local emission, and the third represents the contribution to the intensity in the **s** direction that results from the scattering of intensity in other directions. The equation needs to be solved for I in each given direction **s** at every position [Li, 2006].

4.1.2 Boundary conditions for the radiative transfer equation

To solve the radiative transfer equation given in Equation 4.2, the following radiative boundary conditions are applied to the Czochralski crucible shown in Figure 2.1. At the vertical wall, bottom and top surface, diffusive grey surfaces are assumed, for which the thermal balance gives the following equation,

$$I(\mathbf{r},\mathbf{s}) = \varepsilon(\mathbf{r})I_b(\mathbf{r}) + \frac{1-\varepsilon(\mathbf{r})}{\pi}\int_{\mathbf{s}'\cdot\mathbf{n}_w<0} I(\mathbf{r},\mathbf{s}')\left|\mathbf{s}'\cdot\mathbf{n}_w\right| d\Omega', \tag{4.3}$$

where ε is the boundary emissivity, $\mathbf{n}_w$ the normal direction of the boundary.

Along the center line r=0, symmetric boundary condition is used for the radiative transfer equation as

$$\begin{cases} I(\mathbf{r},\mathbf{s}) = I(\mathbf{r},\mathbf{s}^*) \\ \mathbf{n}\cdot\mathbf{s} = -\mathbf{n}\cdot\mathbf{s}^* \\ \mathbf{s}\times\mathbf{s}^*\cdot\mathbf{n} = 0 \end{cases} \tag{4.4}$$

where the **s*** is the symmetric vector of radiation direction **s**, in respect to the tangent of the boundary, with both **s** and **s*** lying on the plane of **t**–**n** (Figure 4.1).

4.1.3 Radiative heat flux and radiative heat source

The radiation is rarely the only means of heat transfer in engineering practice. In most of the materials processing systems, the radiation is coupled with convection and conduction to transfer heat from high temperature to low temperature. Often the radiative intensity is used to calculate the radiative heat flux and/or radiative heat source to facilitate the coupling with other heat transfer mechanisms. For a grey medium, the radiative heat flux and the radiative heat source are calculated using the following equations,

$$\mathbf{q}(\mathbf{r}) = \int_{4\pi} I(\mathbf{r},\mathbf{s})\mathbf{s}\cdot\mathbf{n}d\Omega\,, \tag{4.5}$$

$$\nabla\cdot\mathbf{q}(\mathbf{r}) = \kappa(4\sigma_s T^4(\mathbf{r}) - \int_{4\pi} I(\mathbf{r},\mathbf{s})\,d\Omega)\,, \tag{4.6}$$

where σ_s is the Stephen-Boltzmann constant, $\mathbf{q}(\mathbf{r})$ the radiative heat flux and its divergence is the radiative heat source.

4.2 Numerical Schemes

The radiative intensity $I(\mathbf{r}, \mathbf{s})$ depends on five independent variables, three spatial coordinates ($\mathbf{r}$) and two direction coordinates ($\mathbf{s}$). Solution of the integro-differential equation presented in Equations 4.2 is a challenging task. Various numerical schemes have been developed to simulate the thermal radiation phenomena and to assist in thermal design involving radiative heat transfer. Among the numerical schemes widely used for numerical solution of internal radiation problems are the finite difference, discrete ordinates, Monte Carlo method and finite element method. The details of the applications of the numerical methods in thermal radiation are given by Siegel and Howell [1992] and Modest [1993].

4.2.1 Discontinuous finite element method

In this study, discontinuous finite element method is employed to solve the radiative transfer equation, Equation 4.2. The discontinuous finite element method, also called discontinuous Galerkin method, was first introduced by Reed and Hill [1973] for the solution of the neutron transport equation. It received extensive attention for the past decade as a powerful numerical tool in the simulation of fluid flow and heat transfer

process. It has been shown that the discontinuous finite element method is particularly powerful in the solution radiative transfer problems in which some physical variables vary dramatically within the computational domain [Oden *et al.*, 1998]. Several reviews on the developments and applications of the discontinuous finite element method are available [Cockburn *et al.*, 2000; Cockburn, 2001]. A monograph on the applications of the discontinuous finite element method in heat transfer and fluid flow is given by Li [2006].

The discontinuous finite element method makes use of the same function space as the continuous finite element method, but with relaxed continuity at inter-element boundaries. The essential idea of the method is derived from the fact that the shape functions can be chosen so that either the field variable, or its derivatives or generally both, are considered discontinuous across the element boundaries, while the computational domain continuity is maintained. From this point of view, the discontinuous finite element method includes, as its subsets, both the finite element method and the finite difference (or finite volume) method. Therefore, it has the advantages of both the finite difference and the finite element methods, in that it can be effectively used in convection-dominant applications, while maintaining geometric flexibility and higher local approximations through the use of higher order elements. Because of the local nature of a discontinuous formulation, no global matrix needs to be assembled; and thus, this reduces the demand on the in-core memory. The effects of the boundary conditions on the interior field distributions then gradually propagate through element-by-element connection. This is another important feature that makes this method useful for fluid flow calculations. Computational fluid dynamics is an evolving subject,

and very recent developments in the discontinuous finite element method are discussed in [Li, 2006].

4.2.2 Discontinuous finite element formulation

In this section, the discontinuous finite element method is applied to solve the radiative transfer equation. Same as of its continuous counterpart, the first step of the discontinuous finite element formulation is to discretize the computational domain into a collection of finite elements. It is worth noting that using the discontinuous finite element, the solid angles are discretized in the framework of finite element space so that the conservation laws are observed, while most of the other numerical methods the solid angle integration is carried out using discrete ordinates.

In the present work, the discontinuous finite element model will be incorporated into the high order finite difference method presented in the last chapter, which is used to solve the flow and temperature fields. Therefore, structured triangular elements are used to solve the radiative heat transfer, which is shown in Figure 4.3. The triangular finite element mesh is constructed by splitting each of the rectangular finite difference elements into two triangular elements, as shown in Figure 4.3. For the two meshes, the nodes are numbered in the same sequence. The radiative calculation is carried out using primitive variables while the flow and temperature fields are solved using dimensionless variables.

The discontinuous finite element procedures start by integrating Equation 4.2 with respect to a weighing function $v(\Omega,\mathbf{r})$,

$$\begin{aligned}&\int_{\Delta\Omega_l}\int_{A_e} v(\Omega,\mathbf{r})\mathbf{s}\cdot\nabla I dA d\Omega \\ &= \int_{\Delta\Omega_l}\int_{A_e} v(\Omega,\mathbf{r})\big(-\beta(\mathbf{r})I(\mathbf{r},\mathbf{s})+S(\mathbf{r},\mathbf{s})\big)dA d\Omega\end{aligned}, \tag{4.7}$$

where A is the area of the element under consideration and $S(\mathbf{r}, \mathbf{s})$ the source term defined as

$$S(\mathbf{r},\mathbf{s}) = \kappa(\mathbf{r})I_b(\mathbf{r}) + \frac{\sigma(\mathbf{r})}{4\pi}\int_{4\pi} I(\mathbf{r},\mathbf{s}')\Phi(\mathbf{s},\mathbf{s}')d\Omega'. \tag{4.8}$$

Applying integration by parts once to Equation 4.7, we have the following expression:

$$\begin{aligned}&\int_{\Delta\Omega_l}\int_{V_e} -I\mathbf{s}\cdot\nabla v(\mathbf{r},\Omega)dV d\Omega + \int_{\Delta\Omega_l}\int_{\Gamma} v(\mathbf{r},\Omega)\, I^{+}\,\mathbf{n}\cdot\mathbf{s}\, d\Gamma d\Omega \\ &= \int_{\Delta\Omega_l}\int_{V_e}\big(-\beta(\mathbf{r})I(\mathbf{r},\mathbf{s})+S(\mathbf{r},\mathbf{s})\big)v(\mathbf{r},\Omega)dV d\Omega\end{aligned} \tag{4.9}$$

where the superscript + means taking the value outside the element boundary and where **n** is the out-normal of the element boundary. In deriving the above equation, use were made to the following divergence theorem,

$$\mathbf{s}\cdot\int_{\Gamma}\phi I\mathbf{n}dA - \mathbf{s}\cdot\int_{V_e} I\nabla\phi dV = \mathbf{s}\cdot\int_{V_e}\phi\nabla I dV \tag{4.10}$$

to convert the domain integral into the boundary integral. Note that in selecting the values of I on the boundary, we have chosen those lying just outside the element under consideration. This choice is made in order to be consistent with the upwinding scheme.

Applying integrate by parts once again and also using the divergence theorem to convert the volume integral into the surface integral, the following integral formulation for the radiative intensity I is obtained

$$\begin{aligned} &\int_{\Delta\Omega_l}\int_{V_e} v(\mathbf{r},\Omega)\,\mathbf{s}\cdot\nabla I\,dV\,d\Omega + \int_{\Delta\Omega_l}\int_{\Gamma} v(\mathbf{r},\Omega)\,[I]\,\mathbf{n}\cdot\mathbf{s}\;d\Gamma\,d\Omega \\ &= \int_{\Delta\Omega_l}\int_{V_e} \big(-\beta(\mathbf{r})I(\mathbf{r},\mathbf{s}) + S(\mathbf{r},\mathbf{s})\big)v(\mathbf{r},\Omega)\,dV\,d\Omega \end{aligned} \quad . \tag{4.11}$$

It is worth noting that in the conventional finite element formulation, the terms on the element boundary disappear when they are combined with neighboring elements. In the discontinuous formulation, however, these terms do not cancel when the elements are assembled. Instead, the following limiting values are used:

$$I_j^+ = \lim_{\mathbf{r}_j\to\Gamma^+} I(\mathbf{r}_j) \text{ and } I_j^- = \lim_{\mathbf{r}_j\to\Gamma^-} I(\mathbf{r}_j) \tag{4.12}$$

where the superscripts + and – denote the front side and back side of the normal vector, respectively. The above treatment assumes that the two values I_j^+ and I_j^- across the element boundaries are not the same, and these jumps are often denoted by,

$$[I]_j = I_j^+ - I_j^- \tag{4.13}$$

For the thermal radiation problem under consideration, the simplest and yet effective treatment of the jump condition is by using the upwinding procedure, which in the discontinuous finite element literature is sometimes referred to as the inflow boundary value,

$$[I]_j = \begin{cases} [I]_j & if \quad \mathbf{n}\cdot\mathbf{s} < 0 \\ 0 & if \quad \mathbf{n}\cdot\mathbf{s} > 0 \end{cases}. \tag{4.14}$$

Appropriate interpolation functions now may be chosen from the finite element broken space that does not demand continuity across the inter-element boundaries. A natural choice of shape functions for internal radiation applications is made by taking a step function for the solid angle and a polynomial function for the spatial variation, $v(\Omega,\mathbf{r}) = \psi(\Delta\Omega_l)\phi(\mathbf{r})$. Here $\psi(\Delta\Omega_l)$ is the step function of the solid angle differential centered at Ω_l, and $\phi(\mathbf{r})$ is the shape function of the spatial coordinates. Substituting this testing function into the integral expression and re-arranging, the final form of the integral presentation of the radiative transfer equation is obtained as

$$\begin{aligned} &\int_{\Delta\Omega_l} \mathbf{s}\cdot\int_{V_e} \phi\,\nabla I(\mathbf{r},\mathbf{s})\,dV d\Omega + \int_{\Delta\Omega_l}\int_{\Gamma} \phi\,[I]\,\mathbf{n}\cdot\mathbf{s}\,d\Gamma d\Omega \\ &= \int_{\Delta\Omega_l}\int_{V_e} [-\beta(\mathbf{r})\phi\, I(\mathbf{r},\mathbf{s}) + \phi\, S(\mathbf{r},\mathbf{s})]\,dV d\Omega \end{aligned}, \tag{4.15}$$

Equation 4.15 reduces to the finite volume formulation if a constant shape function $\phi(\mathbf{r})$ is used, and to the finite element formulation, across the element interface,

when [*I*] = 0 is enforced. From this perspective, Equation 4.15 represents a general integral formulation for all these integral-based methods.

Following the standard procedure for elemental calculations, Equation 4.15 can be solved, once the shape functions are known. Assembling all these discretized terms together for the element, the final discretized equation can be expressed in terms of the following matrix form:

$$\mathbf{KU} = \mathbf{F} \tag{4.16}$$

where **U** contains the unknown intensity vector and the matrix elements are summarized as follows:

$$\begin{aligned} K_{ij} &= \int_{V_e} \phi_i \nabla \phi_j \cdot \int_{\Delta\Omega_l} \mathbf{s}\, d\Omega\, dV + \int_{V_e} \phi_i \phi_j \beta dV \int_{\Delta\Omega_l} d\Omega \\ &+ \sum_{k=1}^{Nd} \max(0, -\int_{\Delta\Omega_l} \mathbf{s}\cdot\mathbf{n}_k\, d\Omega) \int_{\Gamma_k} \phi_i \phi_j\, d\Gamma \end{aligned} \tag{4.17}$$

$$F_i = \int_{V_e} \phi_i S(\mathbf{r},\mathbf{s}) dV \int_{\Delta\Omega_l} d\Omega + \sum_{k=1}^{Nd} \max(0, -\int_{\Delta\Omega_l} \mathbf{s}\cdot\mathbf{n}_k\, d\Omega) \int_{\Gamma_k} \phi_i \phi_j I_{NB,j}\, d\Gamma \tag{4.18}$$

where *Nd* being the number of boundaries associated with the *i*th element.

For those elements associated with a boundary element, the boundary condition is imposed as follows if the boundary is gray:

$$I^+(\mathbf{r},\mathbf{s}_l) = \varepsilon(\mathbf{r}) I_b(\mathbf{r}) + \frac{1-\varepsilon(\mathbf{r})}{\pi} \sum_{j=0,\,\mathbf{s}_j'\cdot\mathbf{n}>0}^{N_\Omega} I^-(\mathbf{r},\mathbf{s}_j') \left| \mathbf{s}_j'\cdot\mathbf{n} \right| \Delta\Omega'_j . \tag{4.19}$$

The following equation is used for the symmetry boundary condition,

$$I^{+}(\mathbf{r},\mathbf{s}_l) = I^{-}(\mathbf{r},\mathbf{s}_l^{*}) \tag{4.20}$$

where $\mathbf{s}^{*}$ is the symmetric direction of $\mathbf{s}$ with respect to the boundary, Figure 4.1. Equation 4.16 can be obtained for each element and its neighbors, and the calculations are then performed element by element. Thus, with Equation 4.16, the calculation for the *i*th element starts with selecting a direction and continues element by element until the entire domain and all directions are covered. Because of the boundary conditions, iterative procedures are required. Experience suggests that the successive substitution method seems to work well for these types of problems [Li, 2006].

It is worth noting that for the axisymmetric geometry under investigation in the present study, the discontinuous finite element computation is carried out over two-dimensional mesh. This is made possible by mapping the radiative intensity on the *r*-*z* plane into the entire three-dimensional domain during calculation. The mapping procedure exploits the symmetry and periodic conditions associated with the axisymmetry of the problem. Full details about the mapping procedure are given by Cui and Li [2005].

4.2.3 Coupling with the high order finite difference model

The radiation properties solved from the discontinuous finite element model presented in the last section is coupled with the temperature and fluid fields obtained

from the high order finite difference model given in the last chapter to describe the convective phenomena in the Czochralski crucibles.

As it has been shown earlier, the divergence of radiative heat flux gives volumetric heat source, which can be easily incorporated into the energy equation given in Equation 2.5 as

$$\rho c_p \frac{\partial \Theta}{\partial \dot{t}} + \rho c_p (\dot{\mathbf{u}} \cdot \nabla)\Theta = k\nabla^2\Theta + \dot{Q} - \nabla \cdot \mathbf{q}_r, \tag{4.21}$$

with $\nabla \cdot \mathbf{q}_r$ calculated using the radiative transfer equation as described in Equation 4.6. Since the radiation heat flux contribution appears as a divergence term in the source part of the heat balance equation, it can be incorporated in the high order finite difference model through the temperature field [Cui and Li, 2005].

The combined heat convection and radiation calculations require iterative procedures. In the present study, the temperature distribution is calculated using the higher order finite difference method while the internal radiation intensities are calculated by the discontinuous finite elements. The iteration starts with the calculation of temperature without radiative heat transfer. The radiative intensity distribution, and hence the divergence of the radiative heat fluxes, are then calculated using the calculated temperature field. The radiation heat flux divergence is then treated as a heating source and the temperature distribution is updated. This process repeats itself until a convergence on temperature and intensity is obtained.

The radiative heat fluxes at the domain boundaries are balanced by the other heat transfer modes. Therefore the thermal boundary conditions given in Chapter Two need to

be modified to take the radiative heat flux into account at the boundaries, which leads to the following expressions:

$$T = T_d \text{ , for } r \le R_d \text{ and } z=H \tag{4.22}$$

$$q_c + q_r = q \text{ , for } r=R,\ 0<z<H \tag{4.23}$$

$$q_c + q_r = 0 \text{ , for } 0<r<R,\ z=0 \tag{4.25}$$

where q_r and q_c are the heat flux due to radiation and conduction, respectively. The boundary radiative heat flux is calculated using

$$q(\mathbf{r}) = \varepsilon\left(\sigma_s T_w^4 - \int_{\mathbf{s}\cdot\mathbf{n}_w<0} I(\mathbf{r},\mathbf{s})\mathbf{s}\cdot\mathbf{n}_w d\Omega \right) \tag{4.26}$$

where T_w is the wall temperature and $\mathbf{n}_w$ the wall normal pointing into the medium.

Finally, the numerical computational procedures presented in this section are summarized as follows. For each time step, the governing equations are solved for an initial temperature and velocity fields using the high order difference model without the internal radiation. The initial temperature field is then used to calculate the radiative transfer intensity using the discontinuous finite element method. The divergence of the obtained radiative intensity is calculated as the radiative heat source and the boundary heat flux is calculated. The heat source and the boundary heat flux are used by the high order finite difference model to solve for the temperature and velocity fields again. An iterative process is employed to update the temperature field until convergence is reached

between the initial temperature field and the temperature field calculated from the high order finite difference model. The calculated temperature field is then used as initial temperature field of the next time step. The calculation proceeds until the dependant variables, which include velocity, temperature and radiative intensity, satisfy certain convergence conditions.

4.3 Results and Discussions

The discontinuous finite element model is used to solve for convective flow in a square box and the Czochralski crucible in this section. Some of the typical results on flow and temperature fields are presented. A linear stability analysis is carried out based on the flow and temperature fields. The neutral curves are compared with those presented in the last chapter to investigate how the internal radiation changes the stability of the convection.

4.3.1 Natural convection in a square box

Consider a square domain bounded by rigid walls and filled with radiation participating medium shown in Figure 4.4. The square box has a dimension of 1 × 1. Two of its vertical walls are held at different temperature with T_L=1 at y= 1 and T_H=2 at y=0. The two horizontal walls are thermally insulated. This case has been studied by several other researchers [Tan and Howell, 1991; Kssemi and Naraghi, 1993; Shu et al., 2004].

The calculations are carried out using 41 uniformly spaced nodes in both x and y directions. Numerical simulations are carried out at two different Grashof numbers with Gr=10^4 and 10^5. The melt has a Prandtl number of 0.7. It is absorbing, emitting but not

scattering. Figure 4.5 shows the velocity and temperature field for $Gr=10^4$. When the fluid is considered transparent, both the flow and temperature profiles are anti-symmetric, Figure 4.5(a, b). Strong circulating pattern is formed driven by the temperature gradient across the thermal boundaries near the cold and the hot walls. When the fluid is involved in radiative transfer with an absorption coefficient of 1.0, the flow and velocity fields are shown in Figure 4.5(c, d). Both the velocity and temperature fields change dramatically due to the presence of the internal radiation. The thermal boundary layer near the hot wall becomes thicker and that near the cold wall becomes thinner, which result in a high temperature gradient near the cold wall. The bulk fluid temperature increases due to the internal radiation, which is caused by the fourth order power law of the radiation [Tan and Howell, 1991]. The isothermals near the insulated walls are not perpendicular to the boundaries due to the radiative heat flux from the solid walls. Near the hot wall, the fluid is heated by the radiation from the insulated walls and near the cold wall it is cooled by radiation to the insulated walls.

Results for $Gr=10^5$ are shown in Figure 4.6. In this case, much strong convective flow is induced due the higher Grashof number. When the fluid does not participate the radiative transfer, the flow is nested with two co-rotating vortex near the center of the square box, Figure 4.6(a). The thermal boundary layers near the vertical walls are thinner than those for $Gr=10^4$, which results in stronger temperature gradients that induce the strong flow. When the fluid is involved in the internal radiation with an absorption coefficient of 1.0, the velocity vectors and isothermals are shown in Figure 4.6(c, d). The same changes in temperature profiles are observed. The isothermals are not orthogonal to the horizontal walls due to the radiative heat flux. The bulk fluid is heated by the internal

radiation. As shown in Figure 4.6(c), the two co-rotating loops merges into one major loop near the cavity center when the internal radiation presents.

The results obtained using the present numerical model compare well with those form the previous works [Tan and Howell, 1991; Kssemi and Naraghi, 1993; Shu et al., 2004].

4.3.2 Convective flow of radiation participating melt in the Czochralski crucibles

In this section, the numerical model developed in this chapter is used to solve for the convective flow in the Czochralski crucibles. The main objective of this section is to investigate how the internal radiation changes the convective flow pattern. Numerical simulations are carried out at various radiative parameters and the velocity and temperature profile are presented in this section.

The crucible under investigation is similar to that used in the last chapter, which is shown in Figure 2.1. Because the internal radiation properties are calculated using primitive variables, a crucible of R=H=0.05m is used for the results presented in this section. Another important parameter for radiation simulation is the reference temperature, T_m, of which 1000 K is used in the present study.

A mesh dependency test is carried out to determine the mesh to be used in the present study. For the axisymmetric base flow, simulations were carried out for a cylinder of R=H=1 with $\mathrm{Re}_\gamma=10^4$, $\mathrm{Gr}=6\times10^5$, κ=1, ε = 1 and σ = 0. The velocities at r=z=0.6 calculated using various uniform meshes are listed in Table 4.1. A uniform grid with 26 nodes in both r and z directions (N_r=N_z=26) is chosen to be used in simulation. Any further refinement will result in less than 2% error in base flow simulation. At each node, the solid angle is discretized into 8 elements in both the θ and φ directions. The

meshes are shown in Figure 4.3. The properties used in the simulations are listed in Table 4.2. The results are plotted in dimensionless variable except for the temperature profiles, which are presented in primitive values.

The flow and temperature fields for the convective flow in the crucible with $Gr=10^5$ are shown in Figure 4.7. The fluid ascends near the solid wall and descends at the crucible center due to the Rayleigh-Bénard-Marangoni effect. The fluid temperature is higher near the vertical wall due to the constant heat flux supplied. When there are internal radiation involves, the velocity vectors and isothermals are plotted in Figure 4.8 for $Gr=10^5$, $\kappa = 1\ m^{-1}$, $\varepsilon = 0.5$ and $\sigma = 0\ m^{-1}$. In this case, the melt is absorbing, emitting but not scattering radiative energy. As it is shown in Figure 4.8, the internal radiation has a strong effect on the temperature distribution. The temperatures near the vertical wall and the free surface are decreased. This is because that the presence of radiative heat flux at the boundaries requires higher temperature gradients to conduct the heat from the walls to ensure energy balance. Considering the reference temperature used in this case (1000 K), a strong heat flux is imposed at the boundaries, which decreases the melt temperature significantly. At the bottom, the isothermals are not orthogonal to the boundary due to the radiative heat flux at the bottom. The internal radiation does not have a strong effect on the velocity profile. Results for a higher wall emissivity of $\varepsilon = 1.0$ are depicted in Figure 4.9. As it is expected, the temperature is further decreased due to the higher boundary heat flux imposed by the higher wall emissivity.

The effects of the absorption coefficient are depicted in Figure 4.10, which shows the velocity vectors and the temperature distribution for $\kappa = 5\ m^{-1}$, $\varepsilon = 1$ and $\sigma = 0$. A comparison between Figures 4.9(b) and 4.10(b) indicates that the bulk temperature is

raised by approximately 6 K due to the increase in absorption coefficient. A careful examination of the radiative transfer equation (Equation 4.2) reveals that when a medium is absorbing and emitting, but not scattering radiative energy, the radiative intensity increases along a given direction **s**. It is observed that though the absorption and emission tends to increase the melt temperature, the cooling effect from the boundary radiative heat flux is much stronger that the bulk temperature is lower than that for the radiative transparent medium (see Figure 4.7).

One of major aspects of the internal radiation is scattering. The results presented so far are for non-scattering mediums. To investigate how the scattering may change the convective flow pattern, simulation was carried out at $Gr=10^5$, $\kappa = 1$, $\varepsilon = 1$ and $\sigma = 1$, of which the velocity and temperature profiles are shown in Figure 4.11. Comparing with the non-scattering results shown in Figure 4.9, it is observed that the melt temperatures near the boundaries are decreased due to the back scattering. The bulk melt temperature is decreased due to the scattering.

When a seeding crystal with radius of 0.5 (0.025 m) is in contact with the melt, results are shown in Figure 4.12. As it has been shown in the last chapter, with the presence of the crystal, a strong temperature gradient is imposed along the free surface, which induces strong Marangoni flow. The effect of the strong Marangoni flow is limited to where near the free surface. In other words, the Marangoni effect does not change the bulk flow structure much. Same changes in the temperature profiles are observed near the vertical wall as the wall emissivity increases. However, no obvious changes in the temperatures beneath the crystal is observed, which is because that the crystal is considered a cold body (T_d=0 K) in the present study.

4.3.3 Stability of convective flow in radiation participating medium

In this section, a linear stability analysis is carried out based on the numerical simulation results presented in the last section. The stability analysis is focused on how the radiative parameters affect the stability of the flow. Similar to the last chapter, neutral curves are determined as functions of the azimuthal wave numbers and the critical Grashof numbers at which the real parts of the leading eignvalues vanish. For the results presented in this chapter, the linear stability analysis is carried out at a fix Marangoni-Reynolds number of 10^4 for azimuthal wave numbers ranges from 1 to 8.

Figure 4.13 shows the critical Grashof numbers for absorbing, emitting but not scattering melt in a Czochralski crucible of R=H=0.05 m. The absorption coefficients, κ, used for the analysis are 1 m^{-1} and 5 m^{-1}, respectively. The emissivity at the boundaries is 1. The neutral curve for the corresponding transparent melt case is shown in Figure 3.9. A comparison between Figures 3.9 and 4.13 reveals that the presence of the internal radiation delays the onset of the instability. The critical Grashof number is raised from 281224 for transparent melt to 598673 for κ=1 m^{-1} and 629856 for κ=5 m^{-1}. It is obvious that the internal radiation stabilized the convection and the stabilization effect increases as the absorption coefficient increases. The same stabilization effect has been observed in several previous works [Arpci and Gözüm, 1973; Arpci and Bayazitoğlu, 1973]. The most dangerous azimuthal mode is changed from 1 to 5 due to the internal radiation.

The stability diagram at two different boundary emissivities is depicted in Figure 4.14. The neutral curves are obtained using the same crucible as the last case. The melt has an absorption coefficient of 1.0 and the vertical wall, the bottom and the top surface are emitting diffusively at two emissivities of 0.5 and 1, respectively. As it is expected,

the critical Grashof numbers are increased due to the internal radiation. The critical Grashof number is 476837 for ε=0.5 and 598673 for ε=1. The most dangerous azimuthal mode is found to be 5.

Figure 4.15 shows the neutral curves for an absorbing, emitting and scattering medium in the same crucible. The melt is absorbing at κ=1 m^{-1} and the stability curves are obtained at two different scattering coefficients of 0 and 1, respectively. As it can be seen from the figure, with the presence of the scattering, the critical Grashof number is further increased, which is 641827 when σ=1. Again, the most dangerous mode is found to be 5.

Figure 4.16 shows typical eigenvalue spectrum of the critical state at Gr_{cr}=598673 for κ = 1, ε = 1 and σ = 0. The eigenvalues could be either real numbers or conjugate complex pairs. The eigenvalue spectrum has T-shape structure, which is similar to those observed in the last chapter. This means the instability mechanism is the same for the radiation participating and non-participating mediums. Table 4.3 lists the first five leading eignvalues. The first leading eigenvalue is a real number while the rest four eigenvalues appear to be conjugate complex pairs. As it has been shown in the last chapter, the first leading eigenvalue is in stationary mode while the rest four eigenvalues are in HOPF mode. The transient evolution of the perturbation energy corresponding to the first two leading eigenvalues are plotted in Figures 4.17 and 4.18 for Gr=598673 and 598700, respectively. The profiles presented in the figures are similar to those obtained in the last chapter and confirm the eigenvalue spectrum shown in Figure 4.16.

The contours of the perturbation energy and temperature for the leading eigenvalue are shown in Figure 4.17. As it is shown in the figure, because of the most

dangerous mode of 5, the contours consist of five pairs of maxima and minima along the azimuthal direction.

Figure 4.18 shows the 3-D flow structure and free surface flow pattern constructed using the leading eigenvalue at the critical state of R=H=1, Re_γ=10^4, Gr_{cr}=598673 and m=5 for κ = 1, ε = 1 and σ = 0. For this case, 10 co-rotating loops are observed along the azimuthal direction, which confirms the perturbation contours plotted in Figures 4.16 and 4.17.

4.4 Summary

In this chapter, a discontinuous finite element model is developed to simulate the internal radiation phenomena in the material processing systems. The discontinuous finite element is incorporated into the high order finite difference model presented in the last chapter via an iterative process.

The integrated numerical model is used to simulate the convective flow of radiation participating melt in the Czochralski crucibles. It is shown that the internal radiation has a strong effect on the convective flow pattern in the crucibles. The radiative heat flux imposed by the domain boundaries induces higher temperature gradient near the boundaries, which decreases the bulk temperature. In the mean time, the melt is heated by combined absorption, emission and scattering effects. However, the boundary heat flux is strong enough to suppress the internal radiation effect.

A linear stability analysis is carried out at various radiative boundary conditions. It is found that the internal radiation stabilizes the convective flow. The convective flow is also stabilized when the emissivity at the boundaries increases. The most dangerous mode is found to be 5. The instability mechanism is also discussed in this chapter and the

same instability mechanism is found for the radiation participating and non-participating melt. Similar instability mechanism is found for the radiation participating and non-participating melts.

N_r	N_z	Velocity
16	16	373.6055
21	21	398.6386
26	26	407.9187
31	31	414.7241
36	36	419.1348

Table 4.1 Calculated velocity at r=z=0.6 calculated using different uniform meshes for a crucible of R= H=1 with Gr=6×10^5, $\mathrm{Re}_\gamma=10^4$, κ=1, ε = 1 and σ = 0.

Parameter	Value
Aspect ratio (R/H)	1.0 (0.05/0.05)
Pr	0.02
Re_γ	10^4
q	1.0
Rad	1.0
T_{amb}	0.0
T_d	0.0

Table 4.2 Parameters used in calculation.

No.	ω_r	ω_i
1	$-3.99467906664291390\times10^{-5}$	$-1.31879272795127343\times10^{-12}$
2	- 97.8254841940514410	± 5325219.45642233454
3	- 108.995862586469201	± 783.762223290688439
4	- 126.372794561720994	± 1841190.81395929889
5	- 131.882452964286188	± 8505316.69366715848

Table 4.3 First five leading eigenvalues for R=H=1, Gr_{cr}=598673 for κ = 1, ε = 1 and σ = 0.

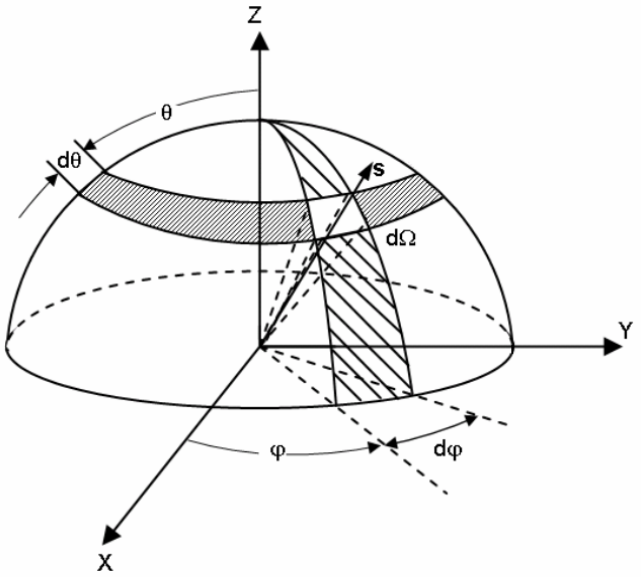

Figure 4.1 Schematic representation of discretization angles for internal radiation problems [Cui and Li, 2005].

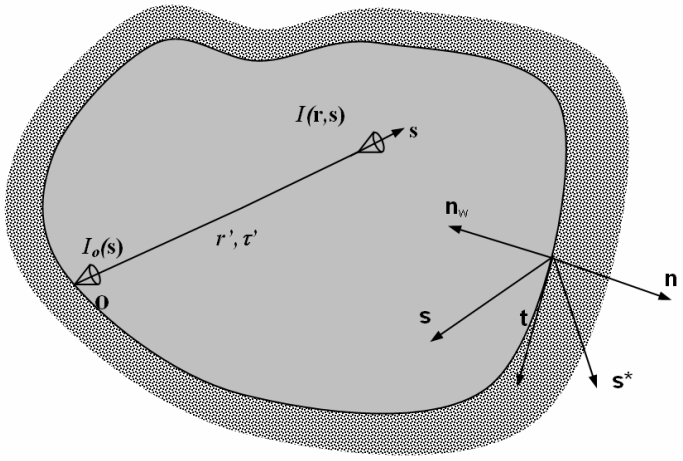

Figure 4.2 Schematic representation of internal radiation heat transfer and symmetry boundary condition [Li, 2006].

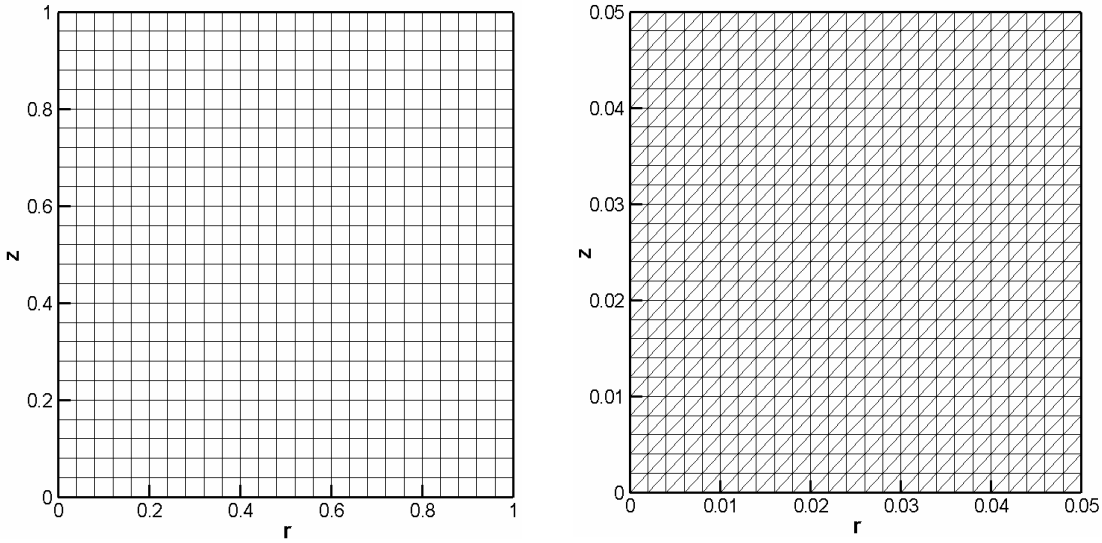

(a) (b)

Figure 4.3 Computational meshes: (a) rectangular mesh for finite difference model; (b) triangular mesh for finite element model.

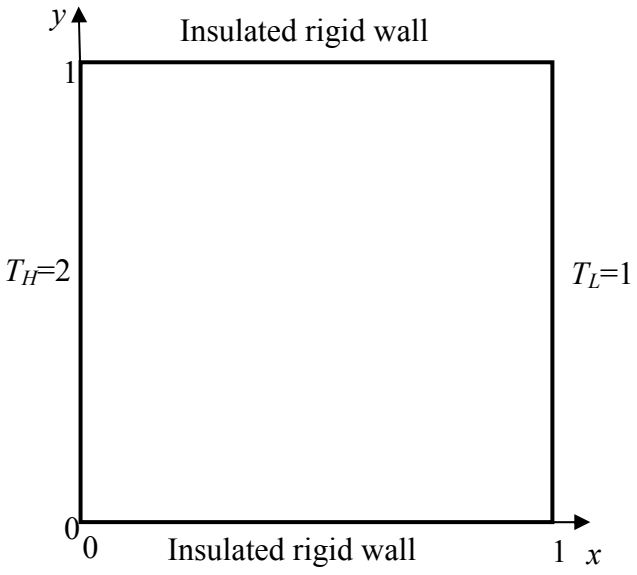

Figure 4.4 Physical setup of temperature gradient induced convection in a square cavity.

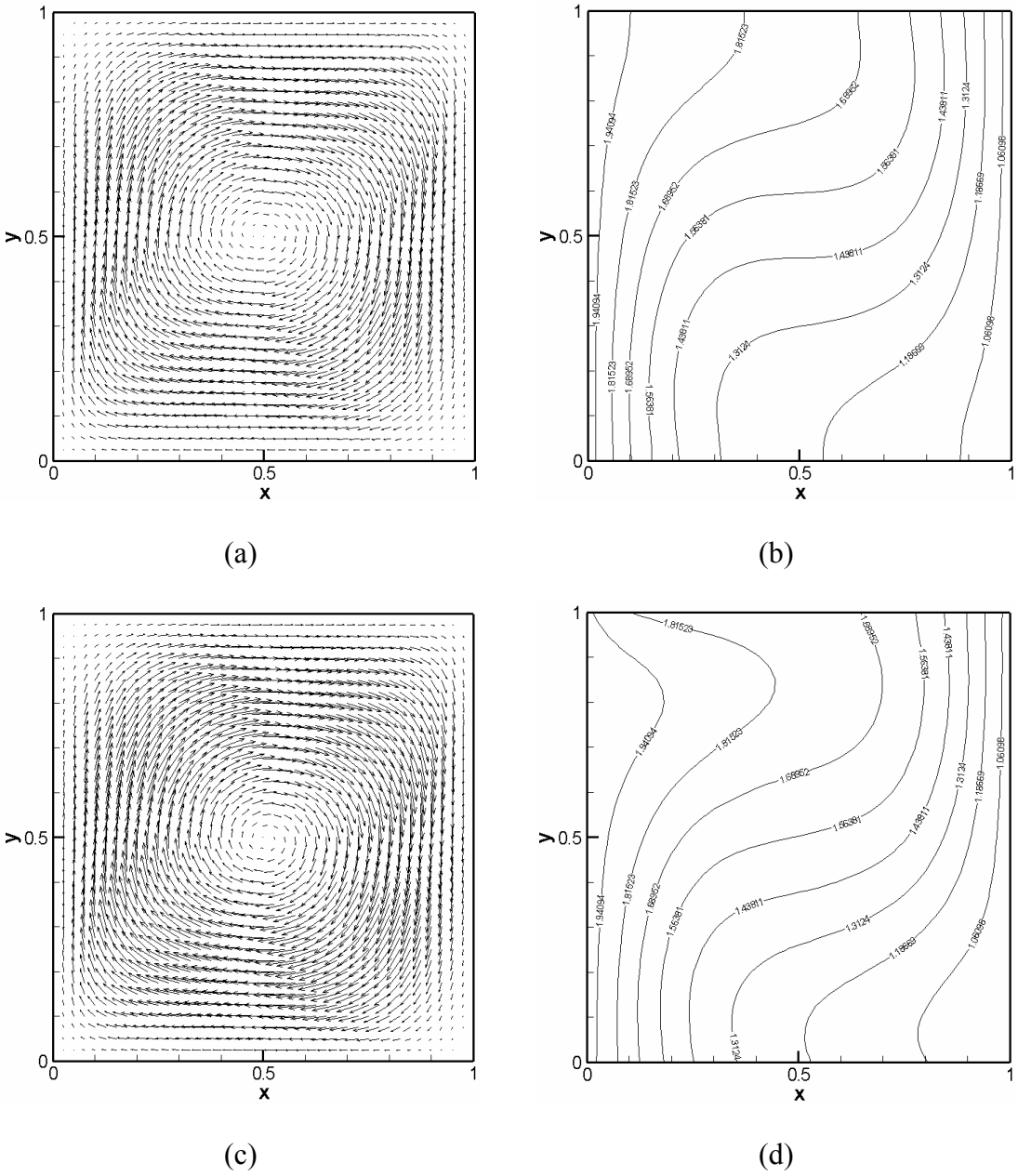

Figure 4.5 Internal radiation effects on melt flow and temperature fields in a rectangular box at Gr=10^4 and Pr=0.7: (a) velocity vectors and (b) temperature profile for non participating medium; (c) velocity vectors and (d) temperature for κ=1.0 m^{-1}.

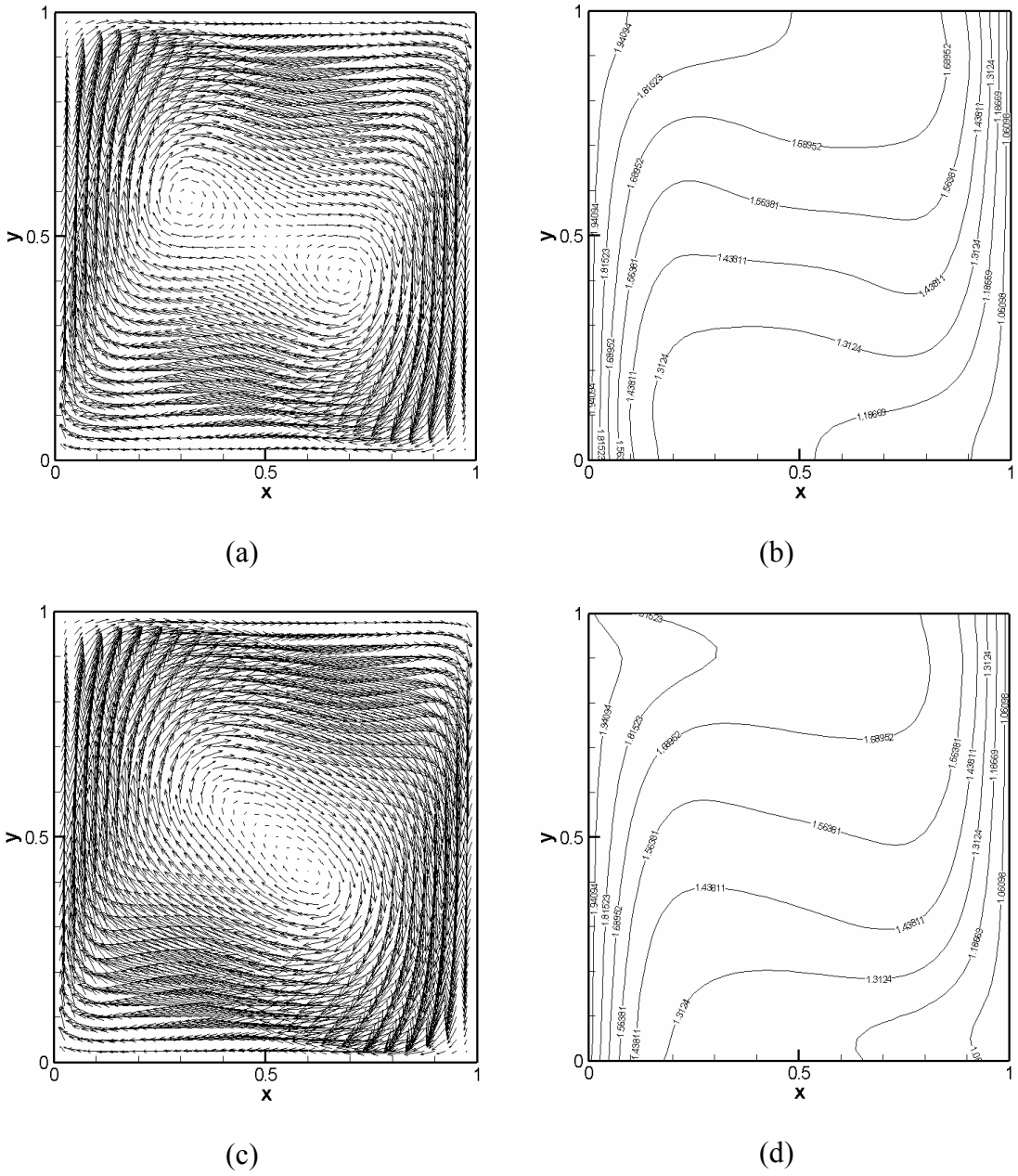

Figure 4.6 Internal radiation effects on melt flow and temperature fields in a rectangular box at $Gr=10^5$ and Pr=0.7: (a) velocity vectors and (b) temperature profile for non participating medium; (c) velocity vectors and (d) temperature for $\kappa=1.0\ m^{-1}$.

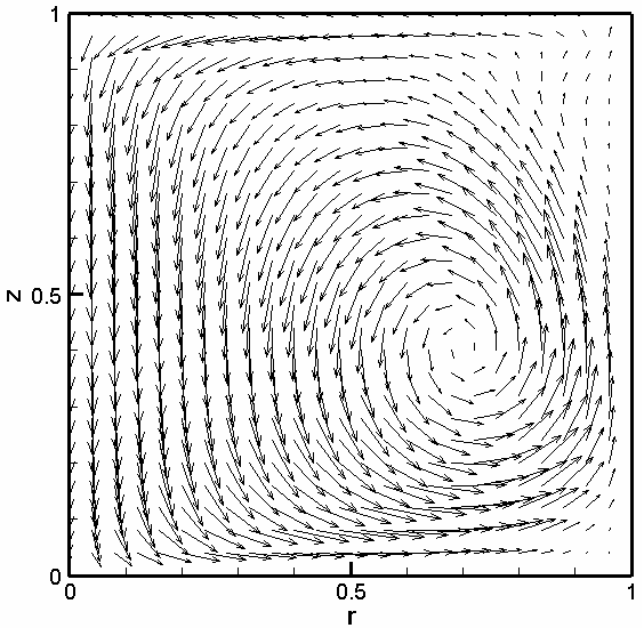

(a)

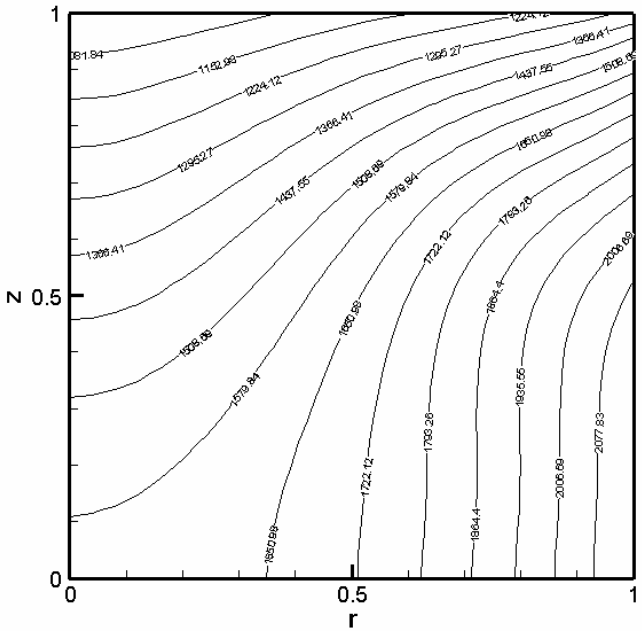

(b)

Figure 4.7 Velocity field (a) and isotherms (b) of the convective flow corresponding to Gr=10^5 and $\kappa = \varepsilon = \sigma = 0$.

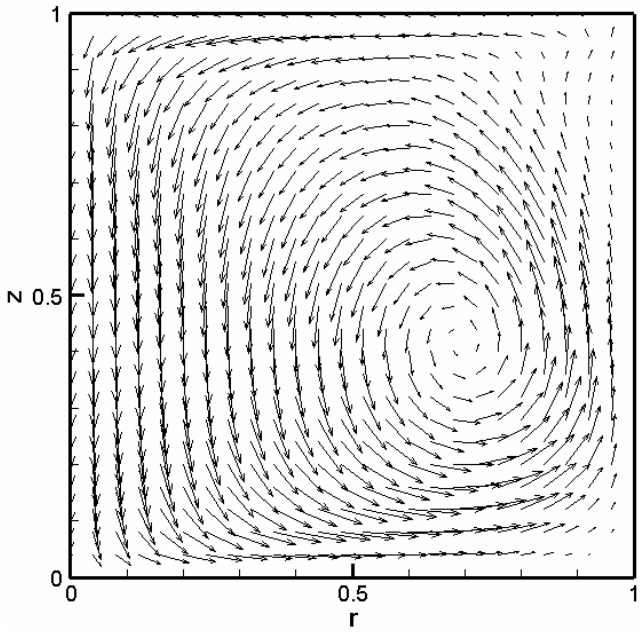

(a)

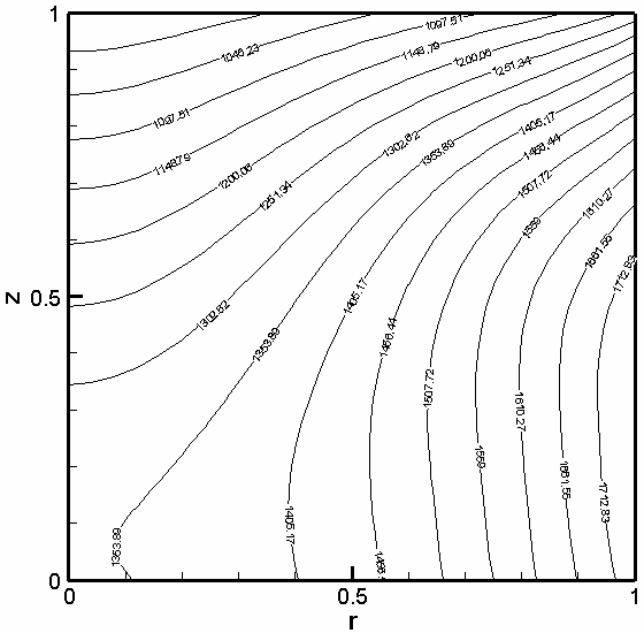

(b)

Figure 4.8 Velocity field (a) and isotherms (b) of the convective flow corresponding to Gr=10^5, $\kappa = 1$ m^{-1}, $\varepsilon = 0.5$ and $\sigma = 0$ m^{-1}.

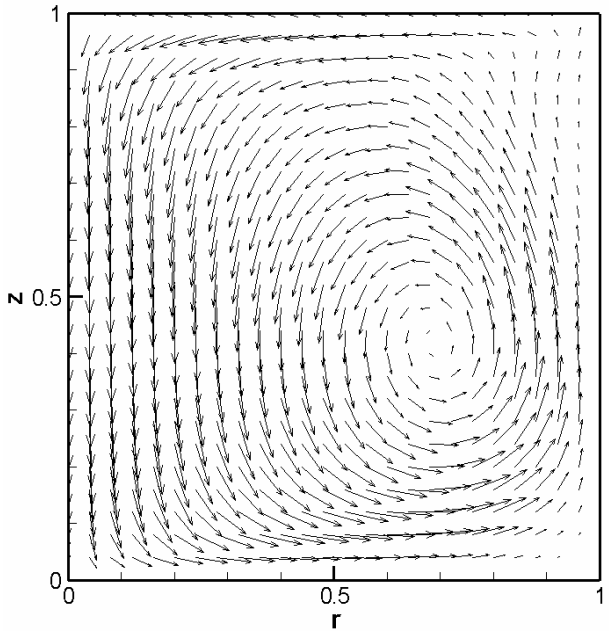

(a)

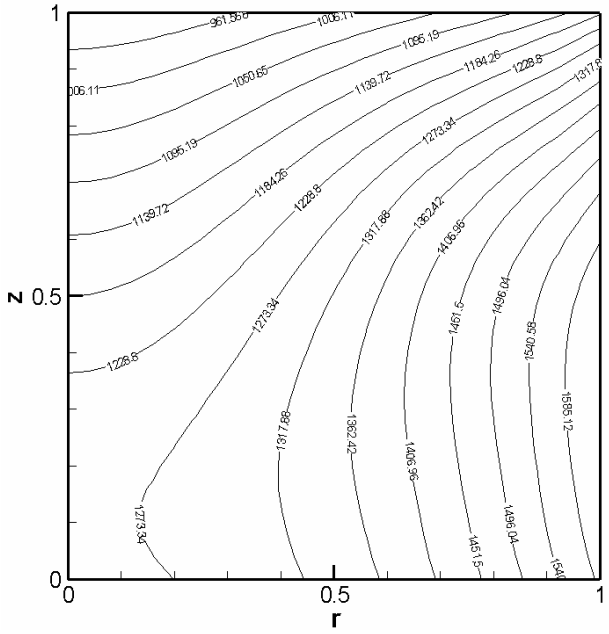

(b)

Figure 4.9 Velocity field (a) and isotherms (b) of the convective flow corresponding to Gr=10^5, $\kappa = 1$ m^{-1}, $\varepsilon = 1$ and $\sigma = 0$ m^{-1}.

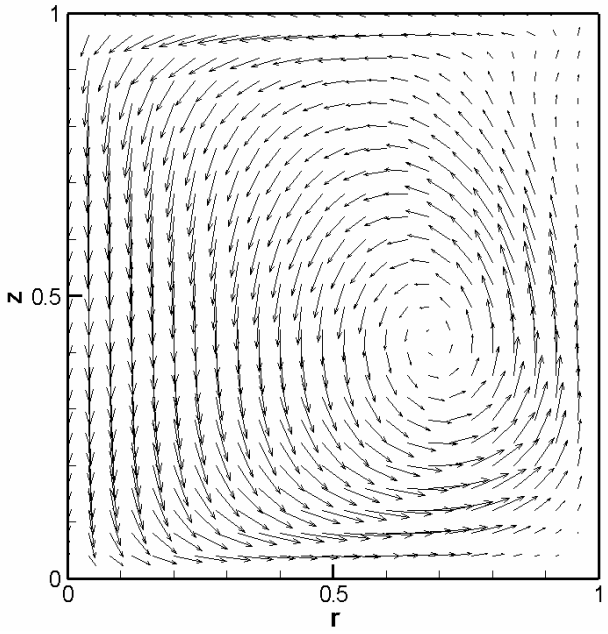

(a)

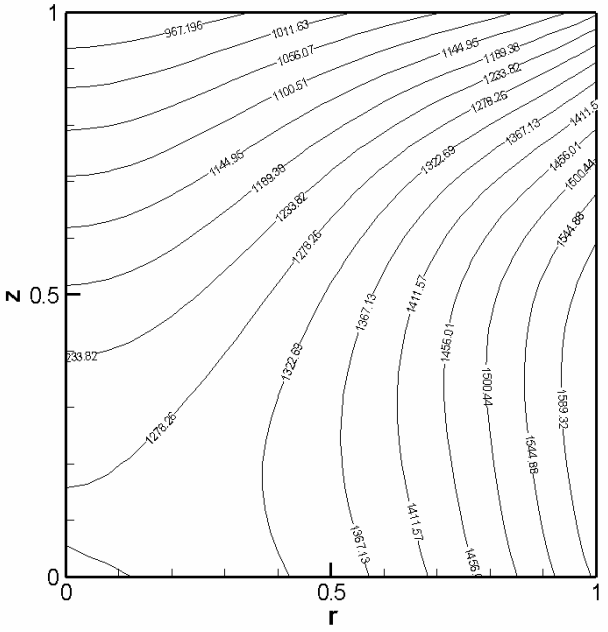

(b)

Figure 4.10 Velocity field (a) and isotherms (b) of the convective flow corresponding to Gr=10^5, $\kappa = 5$ m^{-1}, $\varepsilon = 1$ and $\sigma = 0$ m^{-1}.

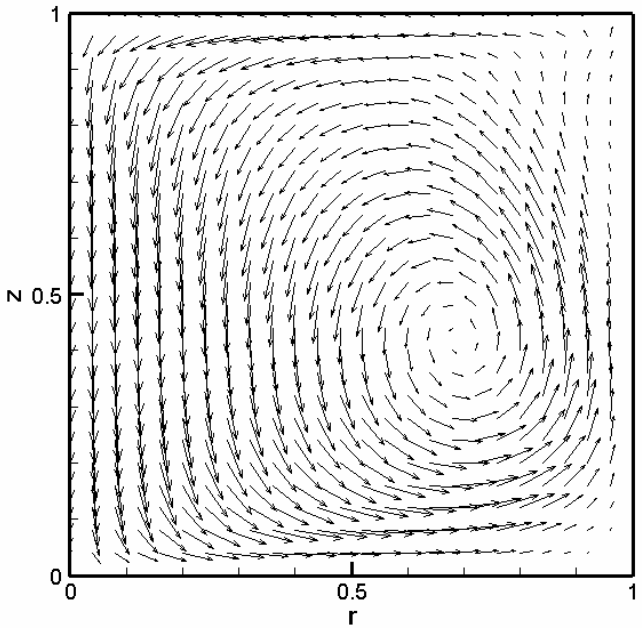

(a)

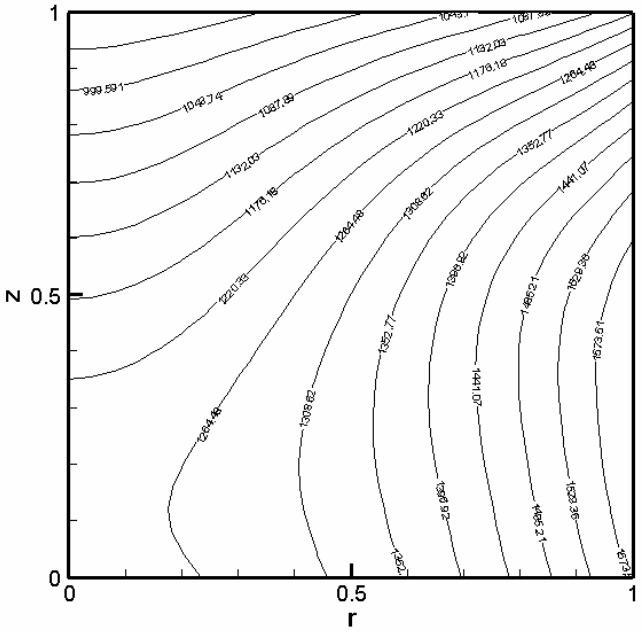

(b)

Figure 4.11 Velocity field (a) and isotherms (b) of the convective flow corresponding to Gr=10^5, $\kappa = 1$, $\varepsilon = 1$ and $\sigma = 1$.

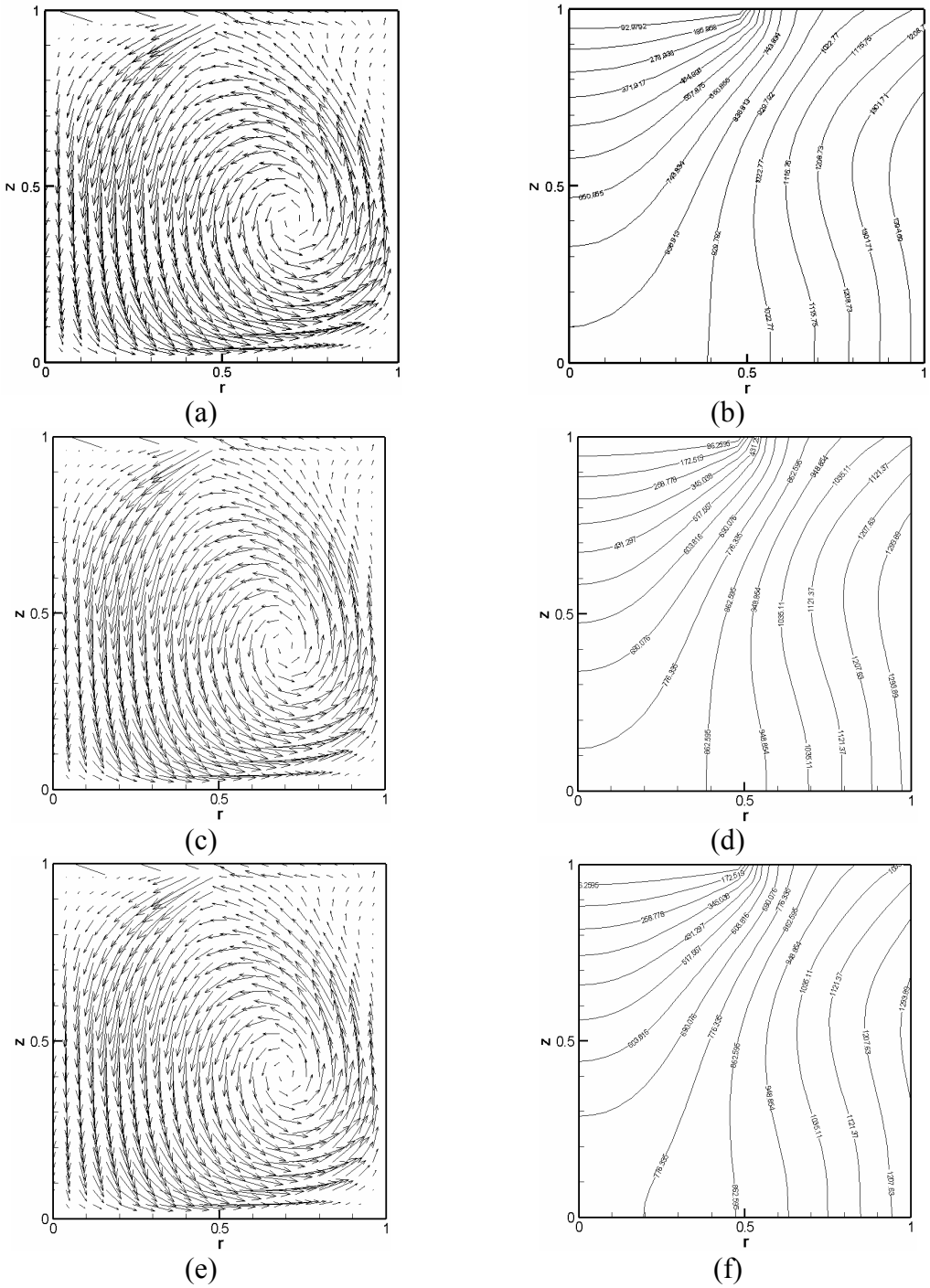

Figure 4.12 Velocity field and isotherms of the convective flow corresponding to $Gr=10^5$, $\kappa = 1$, $\sigma = 0$ and $R_d=0.5$; (a) velocity vectors and (b) temperature profile for non participating medium; (c) velocity vectors and (d) temperature for $\varepsilon = 0.5$; (e) velocity vectors and (f) temperature for $\varepsilon = 1$.

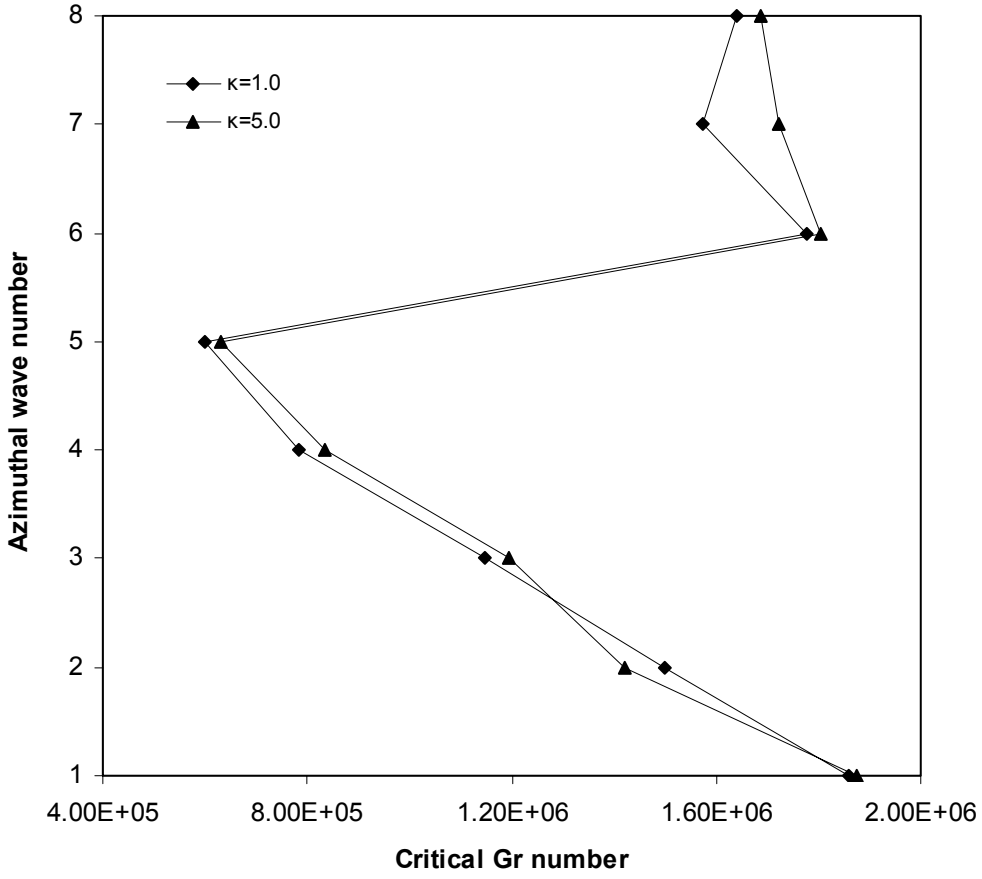

Figure 4.13 Critical Grashof numbers at κ = 1 and 5 for ε = 1 and σ = 0. The critical Grashof number for the corresponding radiative non-participating case is 281224.

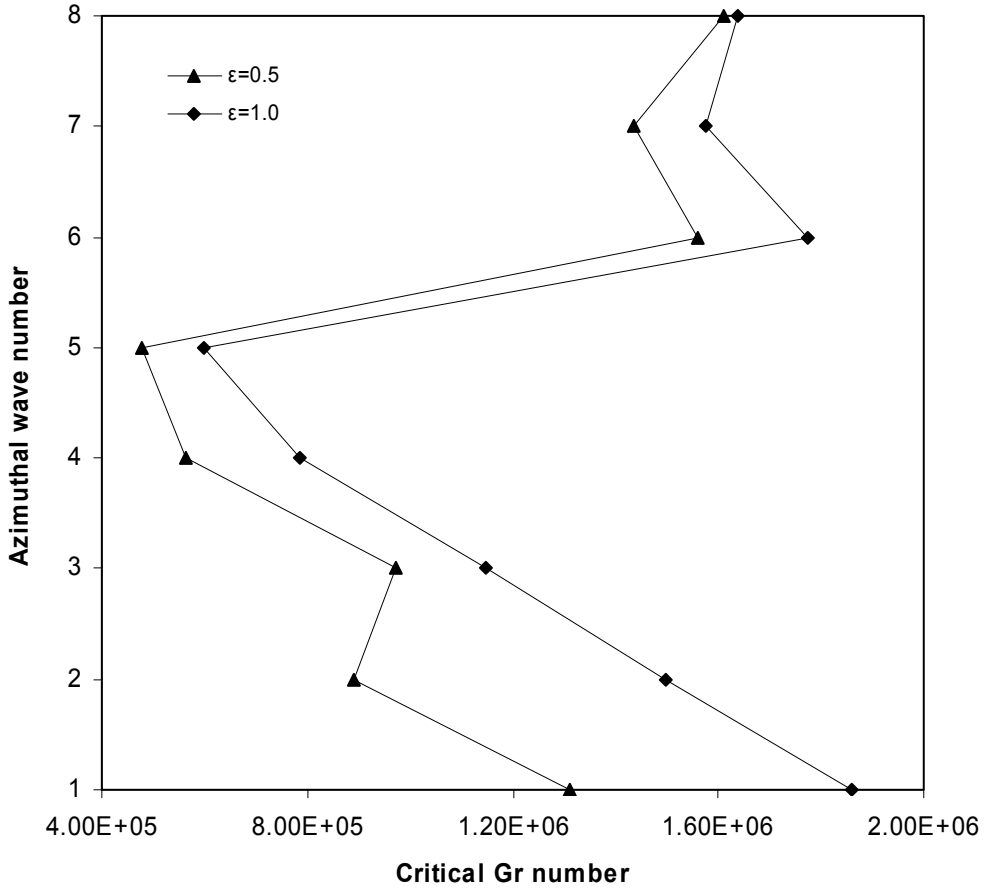

Figure 4.14 Critical Grashof numbers at ε = 0.5 and 1 for κ = 1 and σ = 0. The critical Grashof number for the corresponding radiative non-participating case is 281224.

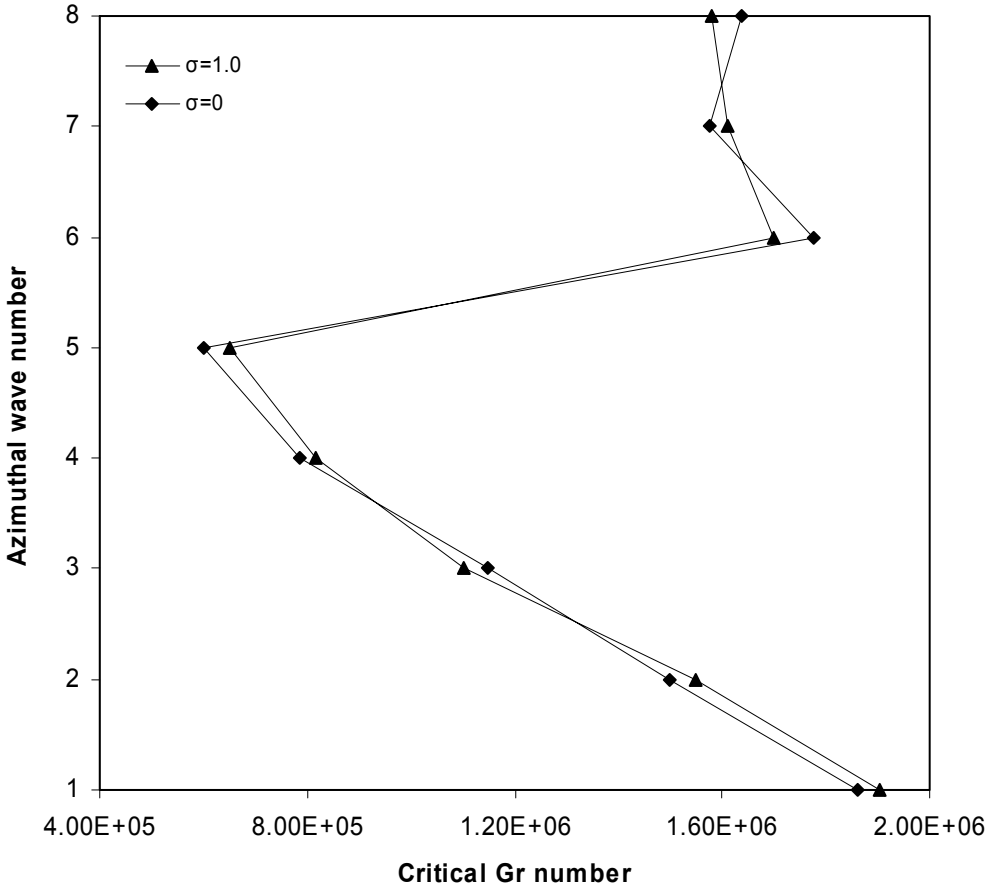

Figure 4.15 Critical Grashof numbers at $\sigma = 0$ and 1 for $\varepsilon = 1$ and $\kappa = 1$. The critical Grashof number for the corresponding radiative non-participating case is 281224.

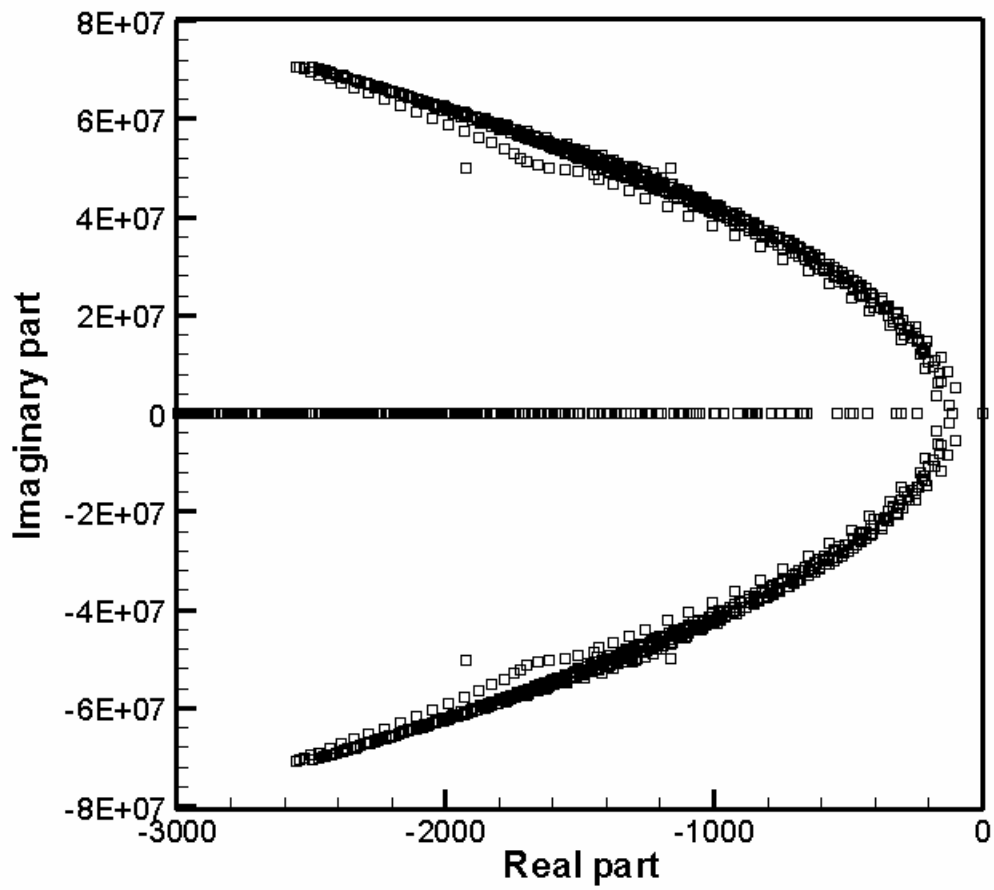

Figure 4.16 Eigenvalue spectrum of critical base flow for R=H=1, Gr_{cr}=598673 at κ = 1, ε = 1 and σ = 0.

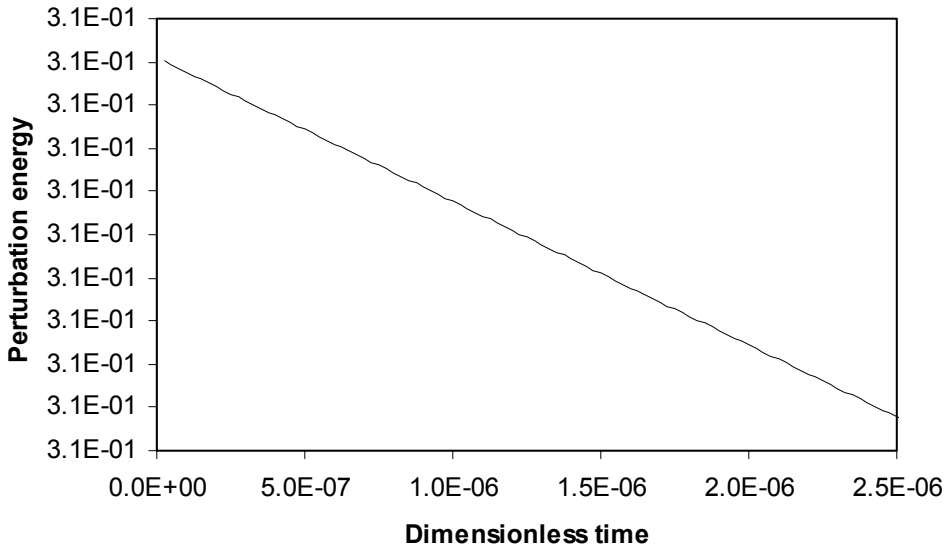

(a)

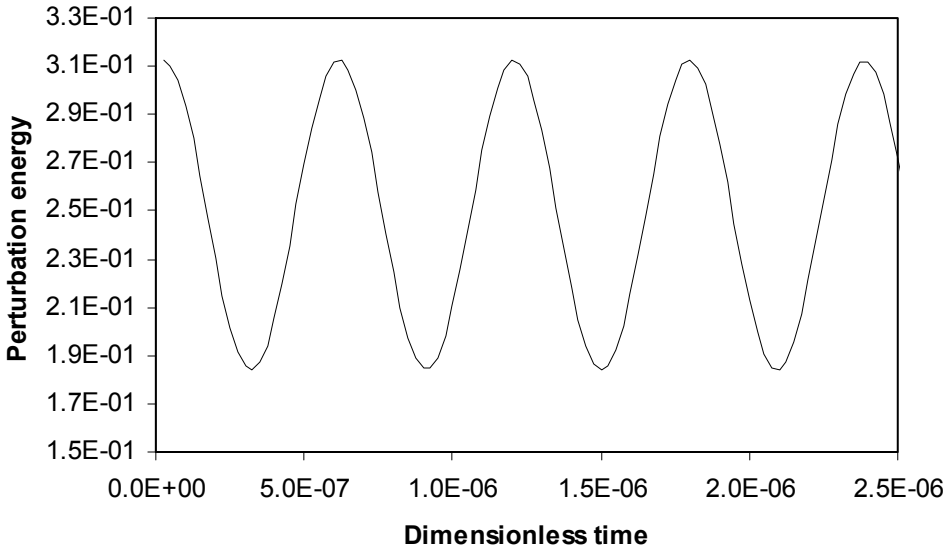

(b)

Figure 4.17 Evolution of perturbation energy in the axisymmetric plane at θ=0 for R=H=1, Gr_{cr}= 598673, Re_{γ}=10^4, κ = 1, ε = 1 and σ = 0: (a) first and (b) second leading eigenvalue

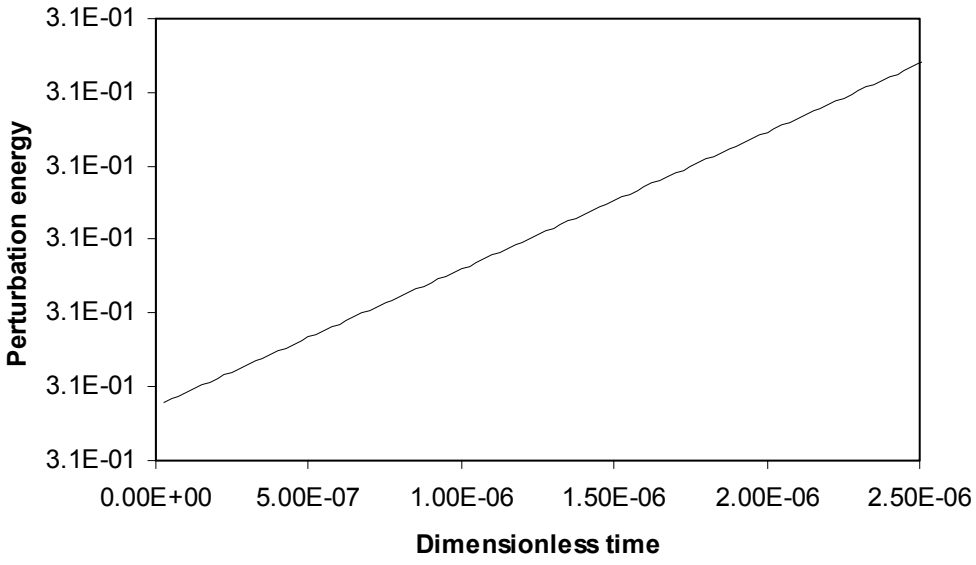

(a)

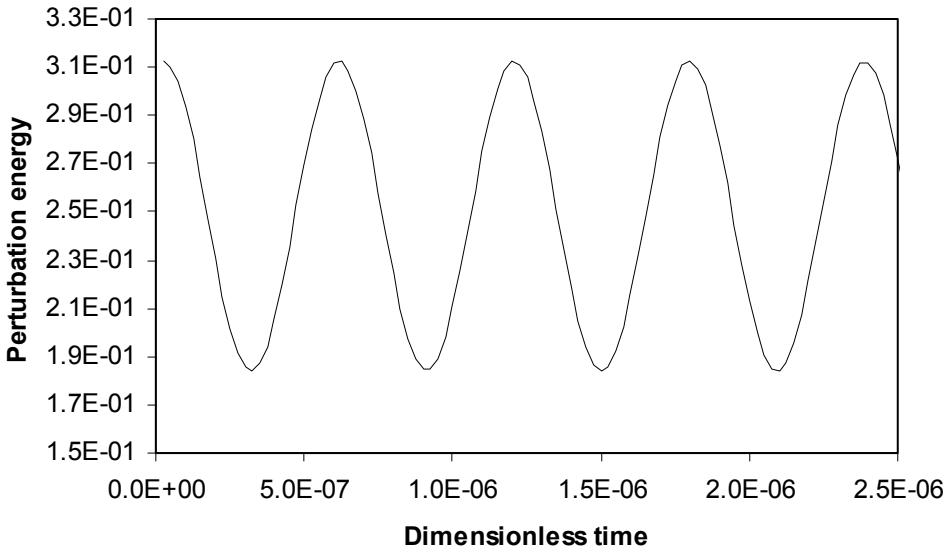

(b)

Figure 4.18 Evolution of perturbation energy in the axisymmetric plane at θ=0 for R=H=1, Gr= 598700, Re_γ=10^4, κ = 1, ε = 1 and σ = 0: (a) first and (b) second leading eigenvalue

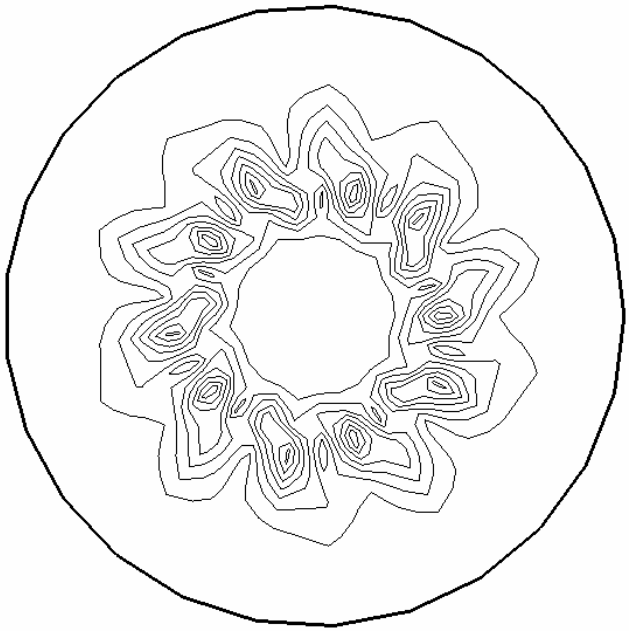

(a)

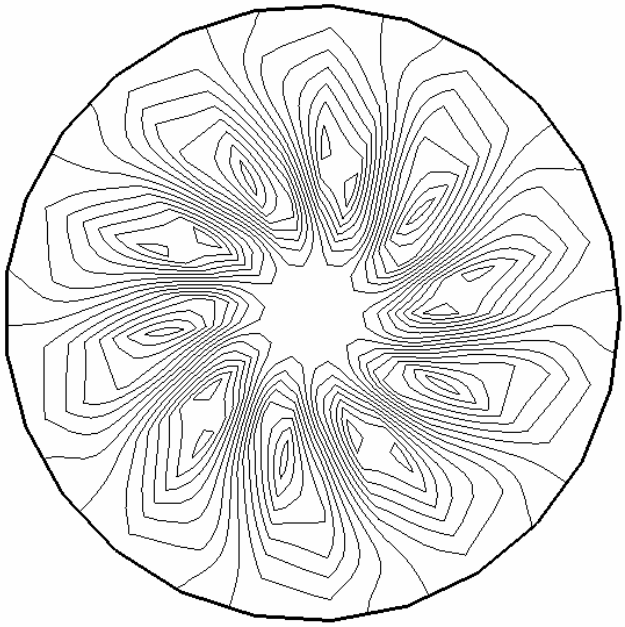

(b)

Figure 4.19 Pattern of perturbation of for the leading eigenvalue at the z=0.5 corresponding to R=H=1, Re_{γ}=10^4, Gr_{cr}=598673, m=5, κ=1, ε = 1 and σ = 0: (a) energy at t=2.5×10^{-8}; (b) temperature at t=2.5×10^{-8}.

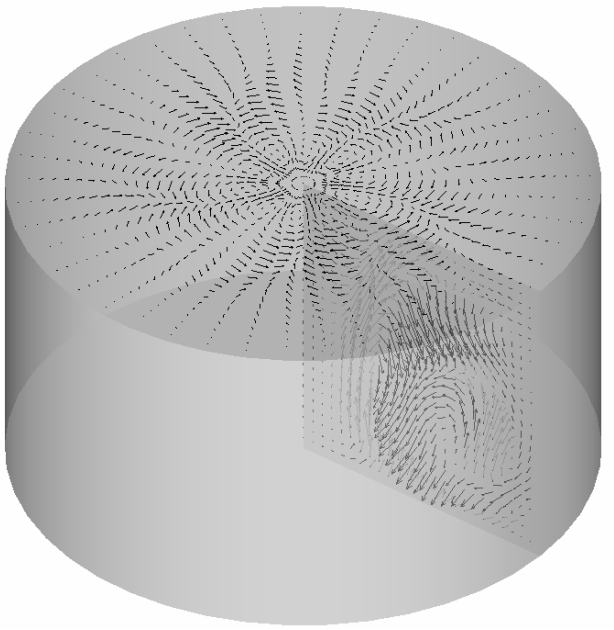

(a)

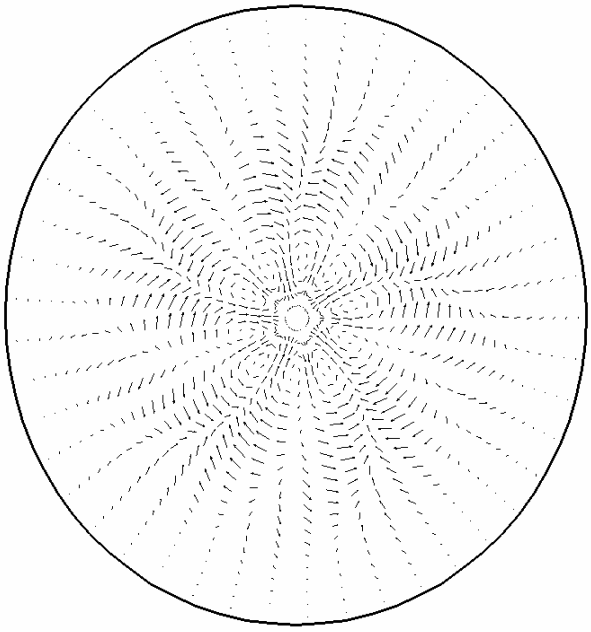

(b)

Figure 4.20 Three-dimensional flow pattern of the leading eigenvalue corresponding to the critical state for R=H=1, $\mathrm{Re}_\gamma=10^4$, Gr_{cr}=598673 and m=5: (a) 3-D flow structure; (b) top surface flow pattern.

CHAPTER FIVE

HOT-FILM MEASUEMENT OF NATURAL CONVECTION IN A RECTANULAR CAVITY WITH AND WITHOUT AN APPLIED MAGNETIC FIELD

This chapter presents an experimental investigation on natural convection in a molten metal subject to a uniform magnetic field. The working fluid is molten gallium, which is contained in a rectangular box with the two opposite vertical walls held at different temperatures. The imposed magnetic fields are parallel to the temperature gradient. The velocity and temperature distributions in the molten gallium are measured both with and without an imposed magnetic field. Numerical simulations of convective flows in the system are also performed. Good agreement exists between the measured and computed results for the conditions studied. Results show that natural convection is suppressed with an imposed magnetic field and the magnetic damping effect increases with an increase in the applied field strength. As a consequence of weakened convection with an increased magnetic field, the temperature distribution approaches to a nearly linear profile across the test cell.

5.1 Introduction

The thermally-induced convection plays an important role in affecting the formation of defects such as dopant segregation or striation during the melt growth of these crystals [Langlois, 1985]. The widespread use of the processes for electronic and

optical materials has resulted in extensive research towards the understanding and hence control of natural convection in these systems.

One of the effective means practiced in industry for thermally-induced melt flow control is magnetic damping, which is derived from the interaction between an electrically conducting melt flow and an applied magnetic field to generate an opposing Lorentz force to the convective flows in the melt. The damping effect depends on the strength of the applied magnetic field and its orientation with respect to the convective flow direction.

There seems to be little work, if not at all, on the direct measurement of thermally-induced melt convection in the presence or absence of an external magnetic field. The need for these measured data cannot be over-emphasized. An experimental study of this type is of crucial importance in providing a database to directly validate the numerical predictions of convective flows from the numerical models in existence and under development. It should also be of great value in direct interpreting the physics governing the magnetic damping effects on convective flows in thermal processing systems.

This chapter presents an experimental study of natural convection in molten gallium with and without an imposed magnetic field. The experimental system consists of a rectangular cell with a prescribed thermal gradient controlled by two thermal baths. The temperature is measured using the thermocouples and the melt flow velocity field is determined using the hot wire probes. The measured velocity and temperature profiles are used to compare with the predictions from numerical models developed in early studies [Shu, *et al.*, 2002]. Good agreements between the numerical predictions and

experimental measurements are achieved. Magnetic damping effects are observed in both the temperature and the velocity profiles when an external magnetic field is applied. The measured velocity and temperature fields should provide a valuable experimental database against which other numerical models developed for natural convection with and without an imposed magnetic field can be validated.

5.2 Experimental Facility and Instrumentation

The setup of the present experiment is shown in Figure 5.1. The system consists of a hot-film anemometer, a hot-film probe, an electromagnet, a probe calibration system and a test cell. Detailed descriptions of each of the components are given in this section.

5.2.1 Gallium

Molten gallium is used as working fluid because its melting point is 302 K and it is inert. Molten gallium is opaque and bright silver in color. Some of its thermal physical properties are listed in Table 5.1 along with the properties of two other liquid metals, mercury and liquid sodium [Brito *et al.*, 2001 and Aurmou and Olsen, 2001], that are commonly used as a working fluid to study heat transfer and convection in liquid metals. Gallium's electrical and thermal conductivities are about four times higher than that of mercury, which makes it an outstanding working fluid for MHD research. Compared with mercury and sodium, gallium is easier and safer to handle because of its low toxicity and low vapor pressure. The initial gallium sample used in the present experiments had a purity of 99.99 %.

5.2.2 Test Cavity

The test cell used in this study was a rectangular container 3-cm deep by 3-cm wide by 15-cm long, which is shown in Figure 5.2. The two long vertical walls (shaded in Figure 5.2) were made of copper and attached to two constant temperature water baths. The temperatures of the water baths were controlled within an accuracy of ± 0.05 K. A horizontal temperature gradient was applied across the gallium inside the cell by holding the two water baths at different temperatures. The open top surface of the cell facilitated the traversing of the hot-film probe and the thermocouple. The other walls of the cell were made of 3-mm Plexiglas. The thermal conductivity of the Plexiglss is 0.2 W/(mK), which is about 1/150 that of the molten gallium. It was observed that a layer of the gallium covered and stayed on the copper walls shortly after the copper walls were in contact with the gallium. No visual observation reveals further deterioration on the copper plates.

5.2.3 Magnetic field

The cell containing the gallium was placed between two electromagnet poles, of 10 in. diameter, of a Walker Scientific Inc. (Model #: HV10H) (see Figure 5.3). A magnetic field strength of up to 10^4 Gauss over an air gap of 10 cm can be generated with the electromagnet. A Walker Scientific Inc. HS-1785 DC power supply was used as the power source for the electromagnets. The power supply provides a stabilized current control, which ensures the stability of the magnetic fields. The strength of the magnetic field was controlled by regulating the D.C. power input to the coils around the electromagnets. In the present experiment, field strengths of 300 and 3500 Gauss, over an air gap of 20 cm were used, which corresponded to 15 Amp and 50 Amp DC input at 75 Volt, respectively.

Spatial uniformity of the magnetic field was assessed by measuring the horizontal magnetic field using a S. W. Bell 9950 Gaussmeter. Typical magnetic field distributions within the cross sectional plane at the middle of the *Z*-direction are shown in Figure 5.4. Considering the size of the test cell, the spatial variation of the magnetic field strength is less than 0.5%.

5.2.4 Hot-film probe

A standard TSI 1210 cylindrical single sensor hot-film probe is used with a TSI 1050 anemometer working in the constant temperature mode with an over heat ratio of 1.1 for a fluid temperature 341 K. In most of the cases when a hot-film is used in liquid metal, the over heat ratio is within the range of 1.05 and 1.075. The relatively high over heat ratio value of 1.1 was used in the present experiment in order to reduce the temperature sensitivity at low velocities [Reed, *et al.*, 1986]. The hot-film probe was powered by a TSI 1050 anemometer working under constant temperature mode in the present experiment. The anemometer bridge output voltage was measured with an HP 3478A voltmeter.

The probe is 1 mm long with an aspect ratio (length/diameter) of approximately 20. A picture of the probe is shown in Figure 5.5. It is coated with a 1 μm layer of quartz to insulate it from the gallium. At very low velocities, the flow around a hot-film anemometer probe is a combination of the externally imposed flow and natural convection driven by the temperature difference between the probe and the surrounding fluid [Trakas, *et al.*, 1983]. Generally speaking, the effects for the natural convection induced by the probe can be neglected if the cubic root of Grashof number for the probe is less than the Reynolds number based on the probe diameter [Collis and Williams,

1959]. For our experiment, the sensor outer diameter is 50 μm, temperature difference between the probe and the gallium is 15 ºC, and typical velocities are 1 cm/s, which give a Reynolds number of 1.6, and a Grashof number of 0.025. Therefore, the effect of probe induced natural convection can be neglected except for velocities below 0.2 cm/s. At these low velocities the magnetic field could alter the probe induced natural convection flow and therefore the heat transfer from the probe [Malcolm, 1970; Lykoudis and Dunn, 1973; Holroyd, 1980]. Since the purpose of this work is to investigate the effect of a magnetic field on natural convection it is difficult to predict *a priori* when this effect will be important. But, as long as probe induced natural convection is not important it can be assumed the magnetic field will not affect the hot-film measurement. Lykouds and Dunn [1973] calibrated hot-film probes in mercury over a Reynolds number range of 0 to 130 and the Hartmann number ranges from 0 to 4.68. They found that the cubic root criterion suggested by Collis and Williams [1959] predicts the critical Reynolds number between the free and forced convection regions well. In our experiment, the Hartmann number is 0.78 with 3500 Gauss applied field. The effect of the magnetic field can be ignored in the present study.

5.2.5 Hot-film probe calibrator

The hot-film probe was calibrated using a rotating platform consisting of an inner container and an outer water jacket. The system is sketched in Figure 5.6. The temperature of the gallium was regulated by running hot water from a constant temperature water bath through the water jacket. The inner container, which held the gallium during the calibration, has a diameter of 10 cm and is made of glass. The outer wall of the water jacket was made hollow and filled with water (shaded in Figure 5.6).

The large volume and high heat capacitance of the water helped to minimize a temperature drift with ± 0.05 K during the calibration. A variable speed motor capable of an angular velocity of 20 to 65 rpm was used to rotate the double container to generate the tangential flow needed for calibration. A type T thermocouple, an ice bath, and an HP 33420A nano-voltmeter were used to measure the temperature of the gallium at the same radial position that was used to calibrate the hot-film probe.

5.3 Experimental Procedure and Data Processing

In the present experiment, the hot-film probe was first calibrated using the rotating platform facility described in the last section. It was then used to measure the velocity field in the molten gallium. In this section, full details of the calibration and measurements procedures are presented along with the data processing method use in this experiment.

5.3.1 Calibration of the hot-film probe

Using a hot-film probe in liquid metals is plagued by the problem of random bridge output offset caused by a layer of impurities that form at the interface between the liquid metal and the probe surface when the probe is immersed into the liquid metal. The impurity layer creates a contact thermal resistance that changes the heat transfer rate between the probe and the liquid metal. The thickness of the impurity layer changes each time the probe is re-immersed into the liquid gallium. This results in a non-predictable offset in anemometer bridge output.

Sajben [1965] investigated the problem using mercury as working fluid and proposed that the effects of the impurity layer can be eliminated by using an $X(Pe)$ function, given by

$$X(Pe) = \pi k_f L_p \Delta T \left(\frac{1}{Q(0)} - \frac{1}{Q(Pe)} \right), \tag{5.1}$$

where k_f is the thermal conductivity of the liquid, L_p the length of the hot-film probe, and ΔT the temperature difference between the probe and the liquid. $Q(0)$ and $Q(Pe)$ are heat transfer rates at a flow velocity of zero and at test conditions, respectively. Pe is the Péclet number, which, for a given temperature, is a non-dimensional velocity in liquid metal given by

$$Pe = \frac{Ud}{\alpha}, \tag{5.2}$$

where U is the velocity, and d the outer diameter of the hot-film prob. At steady state, the heat dissipation rate from the hot-film probe can be determined from the anemometer bridge output by

$$Q = \frac{E^2 R_P}{(R_P + R_T)^2}, \tag{5.3}$$

where E is the bridge output from the anemometer, R_P the resistance of the hot-film probe, and R_T the resistance in series with R_P. R_T is a combined resistance of the leads and the probe holder body, which was measured by a multimeter with the probe replaced by a jumper wire. The combined resistances of R_P and R_T were measured using the resistance decades in the anemometry and then R_P was determined by subtracting R_T from the measured resistance. The values of the measured resistances are listed in Table 5.2. ΔT was determined using the operating temperature of the hot-film probe, calculated using an over-heat ratio of 1.1 and the temperature coefficient of resistance of the probe, and the temperature of the molten gallium, which was measured using a thermocouple. Ignoring the temperature dependence of fluid properties and combining Equations 5.1 and 5.3 give

$$X(Pe) = \frac{\pi k_f L \Delta T (R_P + R_T)^2}{R_P} \left(\frac{1}{E^2(0)} - \frac{1}{E^2(Pe)} \right). \tag{5.4}$$

It is worth noting that the X(Pe) given in Equation 5.4 is function of the anemometer bridge outputs at no-flow condition, $E^2(0)$, and measured condition, $E^2(Pe)$, and the fluid temperature, which is required to calculate ΔT.

It was observed that in addition to the constant offset of the bridge voltage due to impurities, the bridge output varied continuously with time. This continuous drifting of signal was probably caused by an unknown chemical reaction between the liquid gallium and the impurities coating of the hot-film probe. The continuous drifting decreased to an acceptable level after the probe had been immersed in the gallium for several hours;

therefore the probe was aged in the liquid gallium, with the probe hot, for at least four hours before being used.

As it was mentioned earlier, the anemometer bridge voltage is a function of both the velocity and the temperature of the gallium. Because the flow being studied was natural convection and therefore both the velocity and temperature varied through the container, the probe had to be calibrated over the full range of temperatures and velocities that might occur in the experiment. Various temperature compensation schemes are available [Lomas, 1986; Bruun, 1995]. However, all the available temperature compensation schemes require that the temperatures of the fluid and the probe be determined with very low bias error. In this experiment, because only a few measurements were required, the uncertainty was minimized by calibrating the probe over the full temperature and velocity ranges and building a lookup relationship for each measurement. The calibration was done at four constant temperatures, 328 K, 333 K, 339 K and 341 K, and for velocities between 0.5 to 2.8 cm/s at each temperature. During the calibration process, the bridge output was recorded at no-flow condition and then over the entire velocity range at each temperature setting. This process was repeated for each of the four temperatures. The measured bridge outputs were converted to *X(Pe)* using Equation 5.4 for each temperature. The *X(Pe)*-velocity data for each of the four temperatures were curve-fit using

$$U = A_0 + A_1 X(Pe) + A_2 X(Pe)^2, \tag{5.5}$$

where U is the velocity. The obtained calibration curves at the four temperature settings are plotted in Figure 5.7. Typical values for the calibration constants in Equation 5.5 are given in Table 5.2. The shape of the curves shown in Figure 5.7 resembles that found by Malcolm [1969]. Because the over-heat ratio increases as the fluid temperature decreases, the probe is more sensitive at lower fluid temperatures. The calibration was reproducible from one experiment to another over two months within ± 10%. Measured velocities have an uncertainty of ± 0.2 cm/sec and temperatures have a bias uncertainty of ± 0.5 K.

Most liquid metals react with the oxygen in air. Conventionally, the surface of liquid metals is covered with a thin layer of water to stop this reaction. In the present experiment it was found that keeping a layer of water on the top of open liquid gallium surface introduced unwanted disturbance to the temperature field, which may severely affect the calibration process, therefore no water was placed on top of the gallium surface. It was observed that after exposing the free surface of the gallium to ambient air for several minutes, a layer of gallium oxide formed. This layer of oxide insulated the gallium from direct contact with ambient air. After each set of measurements, the oxide and scum were removed from the gallium to keep the gallium clean. No residue was found at the bottom of the cell after the experiments. The probe itself was not cleaned during the experiments.

5.3.2 Measurements

Measurements were taken within cross-sectional surface of Z = 7.5 cm at vertical locations of Y = 0.25 cm, 1.5 cm and 2.75 cm and in increment of 0.25 cm in the X

direction at each vertical level. The probe was accurately positioned in the gallium using a screw-driven manipulator affixed to the electromagnet. Each time the probe was inserted into the gallium it was allowed to stabilize for at least 4 hours and then the free convection bridge output voltage, *E(0)*, was measured for gallium temperatures between 328 K and 341 K with no temperature gradient and no magnetic field applied. A temperature gradient was then applied to the gallium without removing the probe from the liquid metal. When the flow reached a steady state, the velocity field was measured. The magnetic field was then applied and when the flow reached a steady state, the velocity field was again measured. After all the velocity data were taken, the hot-film probe was removed from the gallium and replaced by a type T thermocouple. The measurement process was repeated to map the temperature fields under the same conditions used when the velocity field was measured.

Determination of the velocity from the measured anemometer voltage involved first finding the zero velocity anemometer voltage, *E(0)*, for each measurement and then using *E(0)* and the measured voltage *E(Pe)* to find *X(Pe)* and finally using *X(Pe)* to find the velocity. The no-flow bridge output, *E(0)*, depends on the gallium temperature, which means an *E(0)*–temperature curve was needed in order to process the velocity data at different temperatures. Therefore, before each set of measurements, *E(0)* was first measured over the same temperature ranges as the calibration was carried out. This process was repeated each time the probe was re-immersed into the molten gallium to account for the change in the impurity layer. The measured *E(0)* – temperature data were then fitted to

$$E(0) = B_0 + B_1 T + B_2 T^2 . \tag{5.6}$$

Typical results are shown in Figure 5.8 and typical values for the curve-fitting constants are given in Table 5.2. The zero-velocity voltage decreases as temperature increases because of the smaller probe overheat ratio at higher gallium temperatures.

After all the velocity and temperature data were taken, each anemometer voltage, *E(Pe)*, was converted to *X(Pe)* using Equation 5.4, the zero velocity voltage, *E(0),* from Equation 5.6 and the measured temperature. For each *X(Pe)*, a velocity can be found that corresponds to each of the four calibration temperatures of 328 K, 333 K, 339 K and 341 K using Equation 5.5 and the constants listed in Table 5.2. The four velocity-temperature pairs can then be curve fit to

$$U = C_0 + C_1 T + C_2 T^2 , \tag{5.7}$$

and measured temperature was inserted into Equation 5.7 to find the velocity. Typical values of the curve-fitting constants are listed in Table 5.2.

The temperature measurement has a bias uncertainty of ± 0.5 K. The measured velocities have a bias uncertainty of ± 0.5 cm/s.

5.4 Numerical Model

The numerical model used to compare with the experimental measurements in the present study is described in detail by Shu *et al.* [2002] and thus only a brief description of the points pertinent to the present study is given in this section.

5.4.1 Governing equations and boundary conditions

For molten gallium contained in a rectangular cavity that is subject to a horizontal temperature gradient and a static applied magnetic field (Figure 2.2), governing equations are the equations of continuity, momentum and energy, which are written in a non-dimensionalized form as

$$\nabla \cdot \mathbf{u} = 0\,, \tag{5.8}$$

$$\frac{\partial \mathbf{u}}{\partial t} + (\mathbf{u} \cdot \nabla)\mathbf{u} = -\nabla p + \nabla^2 \mathbf{u} - GrT\mathbf{g} + Ha^2\left[(\mathbf{u} \times \mathbf{B}) \times \mathbf{B}\right], \tag{5.9}$$

$$\frac{\partial T}{\partial t} + \mathbf{u} \cdot \nabla T = \frac{1}{Pr}\nabla^2 T\,, \tag{5.10}$$

where **u** is the velocity vector, T the temperature, p the pressure, t the time, **g** the vertical downward unit vector, and **B** the applied magnetic field. In the above equations, length is non-dimensionalized using L, velocity using v/L, time using L^2/v and temperature using $\frac{T - T_c}{T_h - T_c}$, where L is the distance between the two vertical walls in Figure 2.2, v the kinematic viscosity, T_h and T_c the temperatures at the hot and the cold wall, respectively. The dimensionless numbers governing the flow are Prandtl number (Pr), Grashof number (Gr), and Hartmann number (Ha), which are written as

$$\mathrm{Pr} = \frac{\nu}{\alpha},\ Gr = \frac{g\beta(T_h - T_c)L^3}{\nu^2},\ \text{and}\ Ha = BL\sqrt{\frac{\sigma}{\mu}},$$

where α is the thermal diffusivity, g the gravitational acceleration, β the thermal expansion coefficient, σ the electrical conductivity of the fluid, and μ is the dynamic viscosity. For the molten gallium, the Prandtl number used in calculation is 0.02. The last term on right hand side of Equation 5.9 represents the Lorentz force applied by the external magnetic field, which is the damping force in the present study. For the simplified square 2-D cavity, the governing equations are subjects to the following boundary conditions,

$$\mathbf{u} = \mathbf{0} \text{ at } x = 0, x = 1, \text{and } y = 0, \text{ and } \frac{\partial \mathbf{u}}{\partial y} = 0 \text{ at } y = 1,$$

$$\frac{\partial T}{\partial y} = 0 \text{ at } y = 0, \; T = 0 \text{ at } x = 1, \text{ and } T = 1 \text{ at } x = 0,$$

$$\frac{\partial T}{\partial y} = -Bi\left(T - T_{\infty}\right) \text{at } y = 1,$$

where Bi is the Biot number at the top surface, and T_{∞} the ambient air temperature. The two vertical walls are kept at constant temperatures and the bottom wall is thermally insulated. At the top surface, flow is free of shear stress and rejects heat to the ambient via convection.

5.4.2 Numerical scheme

The governing equations along with the boundary conditions are solved using the standard Galerkin finite element method. The dependent variables **u,** p and T are

interpolated by the shape functions ϕ, ψ and θ. Then the velocity, pressure, and temperature fields are approximated by:

$$u_i(x,t) = \phi^T(x)U_i(t) \tag{5.11}$$

$$p(x,t) = \psi^T(x)P(t) \tag{5.12}$$

$$T(x,t) = \theta^T(x)T(t) \tag{5.13}$$

Following the finite element procedures, the governing equations can be written as:

$$(\int_\Omega \psi \hat{i} \cdot \nabla \phi^T dV)U_i = -\varepsilon_P (\int_\Omega \psi \psi^T dV)P \tag{5.14}$$

$$\begin{aligned}&(\int_\Omega \phi\phi^T dV)\frac{dU_i}{dt} + (\int_\Omega \phi \mathbf{u} \cdot \nabla \phi^T dV)U_i - (\int_\Omega \hat{i} \cdot \nabla \phi \psi^T dV)P \\ &+ (\int_\Omega Gr_T g_i \phi\theta^T dV)T + (\int_\Omega Gr_S g_i \phi\theta^T dV)C = \int_{\partial\Omega} \underline{n} \cdot \tau \cdot \hat{i}\, \phi dS\end{aligned} \tag{5.15}$$

$$\begin{aligned}&(\int_\Omega \theta\theta^T dV)\frac{dT}{dt} + (\int_\Omega \theta \mathbf{u} \cdot \nabla \theta^T dV)T \\ &+ \frac{1}{\mathrm{Pr}}(\int_\Omega \nabla\theta \cdot \nabla\theta^T)dV)T = -\int_{\partial\Omega} q_T \theta dS\end{aligned} \tag{5.16}$$

Once the forms of shape functions ϕ, ψ and θ are specified, the integrals defined in the above equations can be calculated numerically over each individual element. Combining the discretized momentum, energy, and solute transport equations gives rise to the following global finite element stiffness matrix:

$$\begin{bmatrix} \mathbf{M} & \mathbf{0} \\ \mathbf{0} & \mathbf{N_T} \end{bmatrix} \begin{bmatrix} \dot{\mathbf{u}} \\ \dot{\mathbf{T}} \end{bmatrix} + \begin{bmatrix} \mathbf{A(U)} + \mathbf{K} + \mathbf{1/\varepsilon_P}\,\mathbf{E M_P^{-1} E^T} & \mathbf{B_T} \\ \mathbf{0} & \mathbf{D_T(U)} + \mathbf{L_T} \end{bmatrix} \begin{bmatrix} \mathbf{u} \\ \mathbf{T} \end{bmatrix} = \begin{bmatrix} \mathbf{F} \\ \mathbf{G_T} \end{bmatrix} \tag{5.17}$$

While constructing the above element matrix equation, penalty formulation is applied, and the p in momentum equation is substituted by $(1/\varepsilon_P)\mathbf{M}_P^{-1}\mathbf{E}^T\mathbf{U}$. The assembled global matrices are stored in skyline forms and solved using the Gaussian elimination method.

Details of model development and mesh independence study were given by Shu, *et al.* [2002]. In the present study, 900 4-node elements with 31 nodes in both X and Y directions are used. The node spacing decreases from the center toward the walls following an arithmetic progressive ratio of 0.2. The non-uniform mesh ensures denser grid near the solid walls. This mesh arrangement is adequate for the present studies and any further mesh refinement produces results with an error less than 0.5 %.

5.5 Results and Discussions

The hot water in the thermal baths on either side of the container holding the gallium was adjusted until the temperature at the inside center of the copper plates reached 328 K and 339 K, giving a ΔT = 11 K. All experimental measurements were made for this temperature difference. During the experiments the room air was fairly constant at 293 K.

The measured and computed temperature profiles with applied magnetic fields of 0 Gauss, 300 Gauss, and 3500 Gauss are shown in Figures 5.9, 5.10, and 5.11,

respectively. In each of the figures, the temperature profiles across the width of the cell are plotted for Y= 2.75 cm, 1.5 cm and 0.25 cm. The non-linear temperature distributions depicted in Figure 5.9 are clearly a manifestation of the strong natural convection present in the test cell. The temperature profiles along the *X* direction become less-distorted with an imposed magnetic field of 300 Gauss, suggesting that the applied field helps to reduce the convection. This magnetic damping effect is evident in Figure 5.10. When the applied magnetic field reaches 3500 Gauss, the temperature profile is nearly linear, indicating that the convective flow is substantially reduced, and the primary heat transfer mechanism between the hot and cold walls is by conduction, as appears in Figure 5.11. In an idealized natural convection cell with the top and bottom thermally insulated perfectly, the temperature distributions at equal distance above and below the centerline (Y = 1.5 cm) exhibit certain symmetry structure [Shu, *et al*., 2002]. Such a symmetry, however, is not observed between the experimental measured temperature profiles at Y = 2.75 cm and *Y* = 0.25 cm. This asymmetric profile is apparently caused by the heat loss from the top surface of the gallium to the surrounding cooler air, which decreases the temperature near the top surface at *Y*=2.75 cm. The heat loss at the top surface, however, has little effect on the temperature profiles at *Y*=1.5 cm and 0.25 cm. Similar asymmetry was also reported by Juel, *et al.* [2001]. With the presence of the magnetic fields, the convective flow becomes weaker, thereby resulting in less heat being lost at the top surface and the thermal profiles becoming closer in symmetry to the idealized system. For the present system, however, even with a moderate magnetic field strength of 300 Gauss, an obvious temperature drop is observed along Y=2.75 cm, as appears in Figure 5.10.

As a comparison, numerical predictions are also plotted along with the measurements in Figures 5.9, 5.10, and 5.11. The computed temperature profiles at Y = 0.25 and 1.5 cm are in good agreement with the experimental data, but less satisfactory at Y = 2.75 cm for the case without an applied magnetic field. For all the cases, the measured temperature profiles agree with the numerical simulations better along the center-line of the test cell. Various heat transfer coefficients at the top surface were tested to match the temperature profile at Y = 2.75 cm. The numerical simulations show that for this system the heat loss at the top surface does not change the calculated velocity profile.

The velocity vector maps from the experimental measurements and numerical simulations are depicted in Figure 5.12 for three different magnetic fields applied. The scale factor used for the plot is approximately 1.8 cm/s per cm. The direction of the measured velocities are determined by the numerical predictions, as the hot-wire probes measure only the magnitude of the velocity. For a very small velocity, measurement uncertainties sometimes generate a non-physical negative velocity magnitude, which was set to zero. Examination of the results in Figure 5.12 illustrates that an anti-clockwise convection cell is developed in the system as a result of an imposed thermal gradient and the fluid moves downward near the cold wall and upward near the hot wall. This recirculating flow structure is shown in both predictions and measurements. Note also that the velocity magnitudes match very well both qualitatively and quantitatively between the predicted and measured data. Both the numerical simulations and experimental measurements indicate that the velocity is suppressed with an imposed magnetic field and the reduction in velocity is more significant with an increase in

applied magnetic fields. With the field strength of 3500 Gauss, the velocity field is reduced essentially beyond detection by the hot-film probe.

To further quantify the magnetic damping effects, the measured velocity magnitude distributions across the cell along Y = 2.75 cm, 1.5 cm and 0.25 cm are illustrated in Figures 5.13, 5.14, and 5.15, respectively. Each figure gives the profiles for the three levels of the applied magnetic field strength. In light of the vector velocity fields plotted in Figure 5.12, it is clear that the flows are parallel to the top and bottom walls, but in the opposite directions, with the maximum at the middle (X=1.5 cm) for Y=2.75 cm (Figure 5.13) and Y=0.25 cm (Figure 5.15). The maximum of the measured velocity (in magnitude) distribution across the cell at Y=1.5 cm occurs near the two sidewalls, where the flow moves upward and downward along the walls. Once again, the velocity attains its maximum at the middle of the walls. Inspection of the results in Figures 5.13 to 5.15 indicates that the measured velocity decreases with the applied magnetic field increased. With a moderate magnetic field strength of 300 Gauss, the maximum velocity is reduced to about 60% of that without the magnetic field. As the magnetic field strength increases to 3500 Gauss, the velocity is suppressed to nearly zero within the experimental uncertainty. This supports the measured near-linear temperature profile at 3500 Gauss shown in Figure 5.11. For the purpose of comparison, Figures 5.13, 5.14, and 5.15 also show the velocity magnitudes obtained from numerical computations. The computations agree well with the experimental measurements within the experimental uncertainty of 0.5 cm/s.

It could be remarked here that the flow sensed by the hot-film probe is a combination of natural convection induced by the probe and the main natural convective

flow due to the temperature gradient across the cell. Therefore the measured velocity profiles agree with the numerical simulations better at higher velocity magnitudes, near X=15 cm in Figures 5.13 and 5.15 and near the sidewalls in Figure 5.14.

Properties		Gallium	Mercury	Sodium
Density	kg/m^3	6.09×10^3	13.59×10^3	0.93×10^3
Kinematic Viscosity	m^2/s	3.1×10^{-7}	1.14×10^{-7}	7.75×10^{-7}
Electric Conductivity	$(m\Omega)^{-1}$	3.68×10^6	1.04×10^6	10.35×10^6
Thermal Conductivity	W/(mK)	31	8.3	142
Melting Point	°C	29	-39	98
Boiling Point	°C	2227	356	881
Coefficient of thermal expansion	K^{-1}	1.27×10^{-4}		
Surface tension	N/m	0.735		

Table 5.1 Thermal physical properties of some liquid metals [Brito *et al.*, 2001 and Aurmou and Olsen, 2001].

T(K)	**328**	**333**	**339**	**341**
A_0	5.68×10^{-2}	1.14×10^{-1}	1.35×10^{-1}	4.27×10^{-3}
A_1	3.26×10^3	4.00×10^3	6.46×10^3	1.85×10^4
A_2	-8.51×10^5	-1.30×10^6	-3.41×10^6	-3.26×10^7
B_0	1.73×10^1			
B_1	2.40×10^{-2}			
B_2	-3.96×10^{-5}			
R_P	8.03 Ω			
R_T	0.20 Ω			

Table 5.2 Calibration constants.

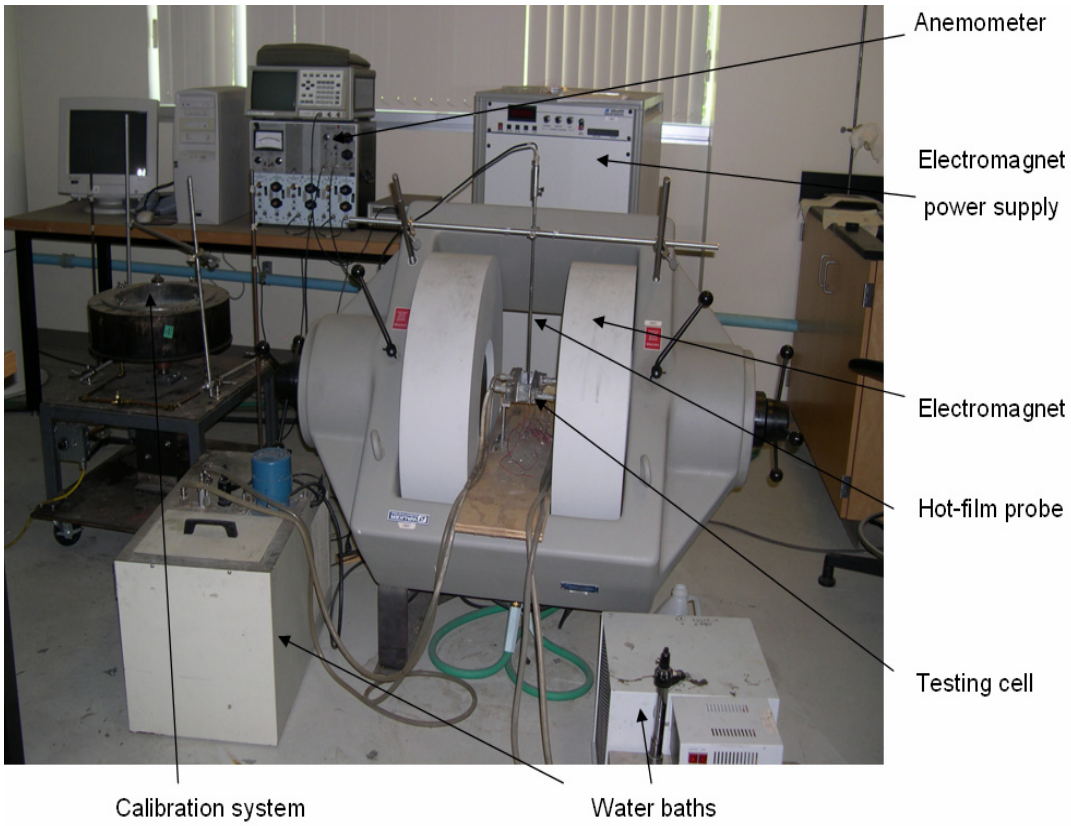

Figure 5.1 Picture of overall experimental setup.

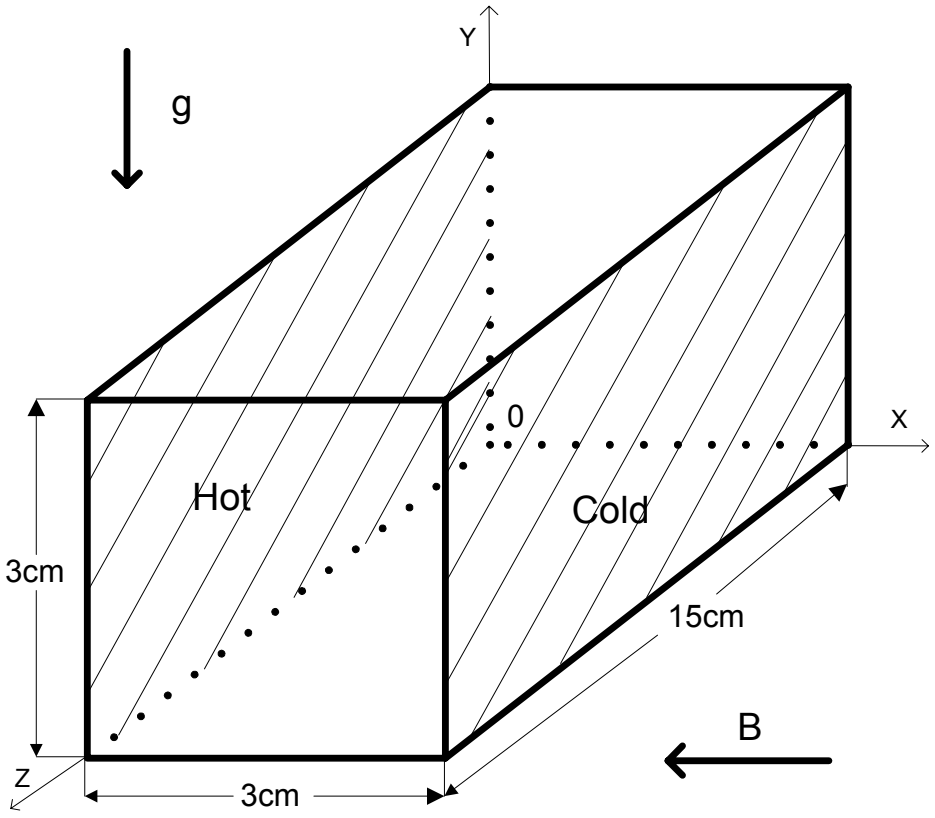

Figure 5.2 Test cell for the experimental study of thermally-induced melt flows.

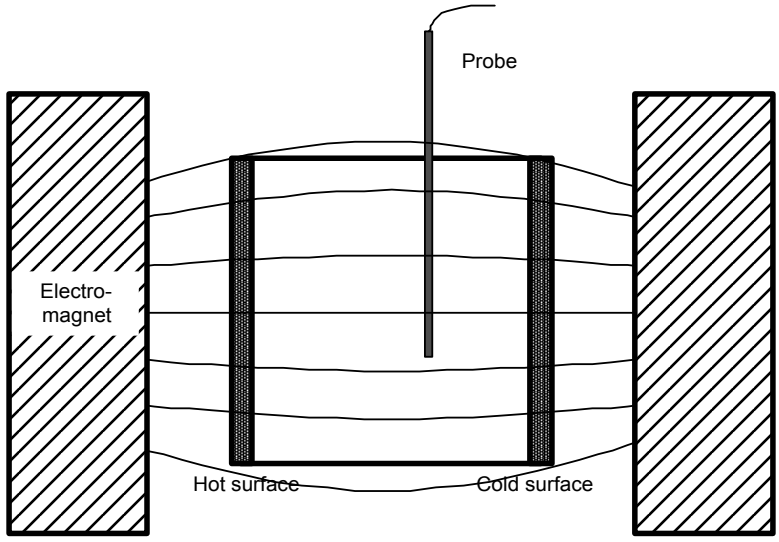

Figure 5.3 Placement of the experimental apparatus for the measurement of the temperature and velocity field distributions in molten gallium subject to applied magnetic fields.

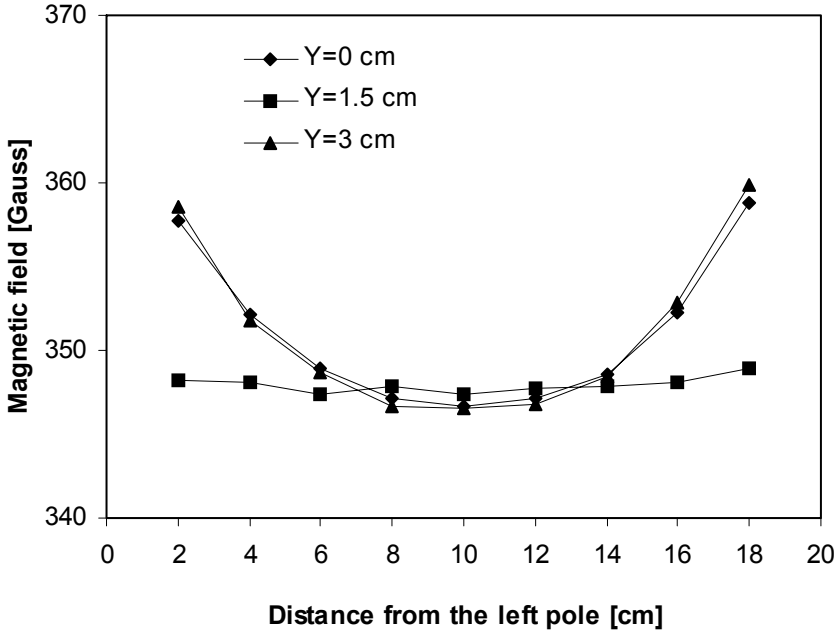

Figure 5.4 Distribution of the horizontal magnetic field strengths along *Y*=0.0 cm, 1.5 cm and 3.0 cm for air gap of 20 cm and 15 Amp DC power supply.

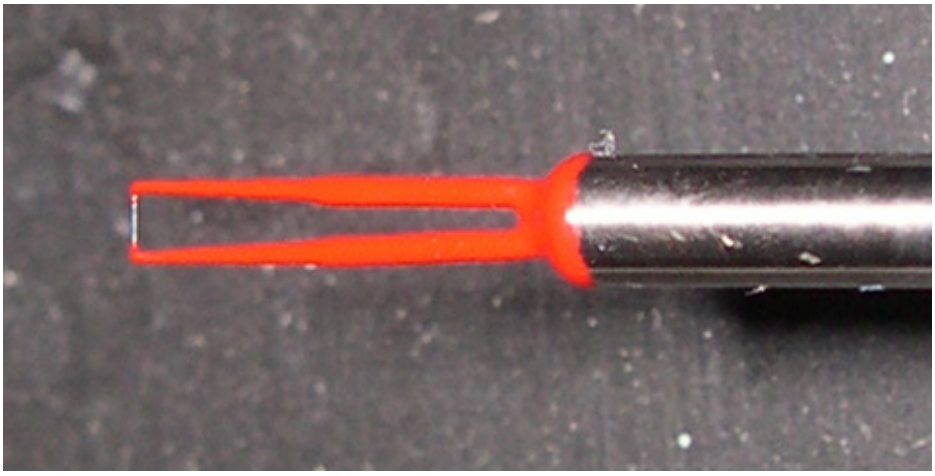

Figure 5.5 Picture of the TSI 1210 cylindrical single sensor hot-film probe used in the present experiment.

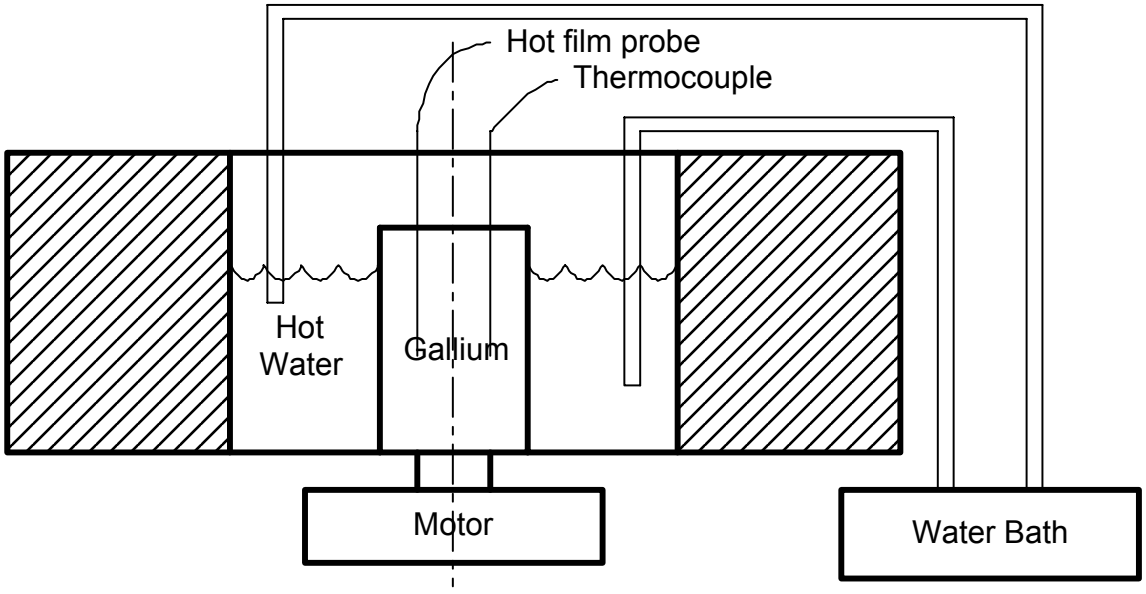

Figure 5.6 The turntable facility for calibration of the hot-wire probe used in the present experiment.

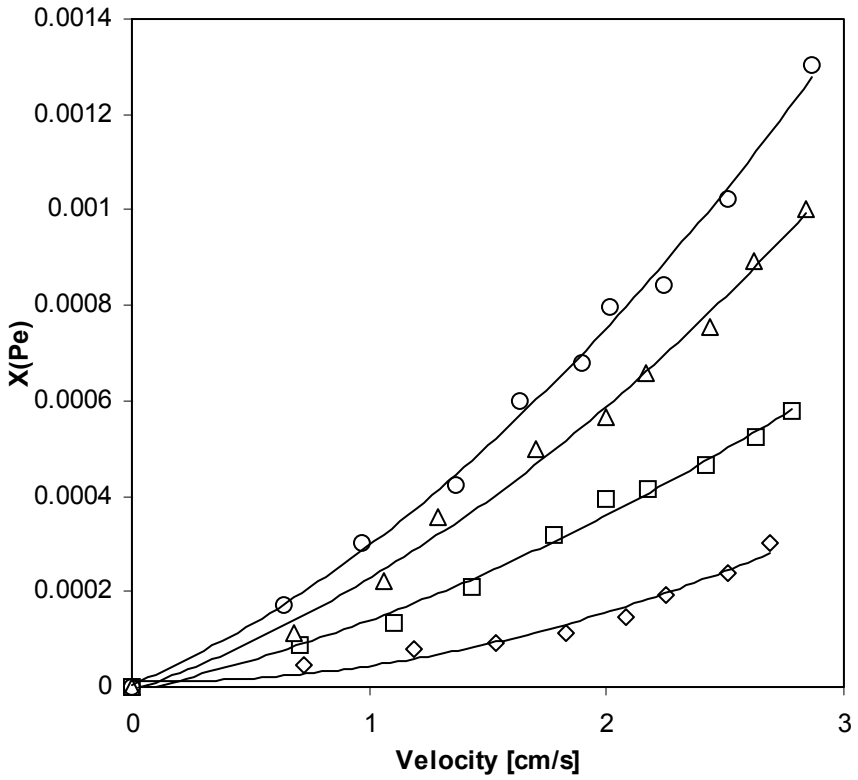

Figure 5.7 Calibration curves for the constant temperature hot wire probe at different temperatures: circles 328.15 K, triangle 333.15 K, squares 339.15 K and diamonds 341.15 K.

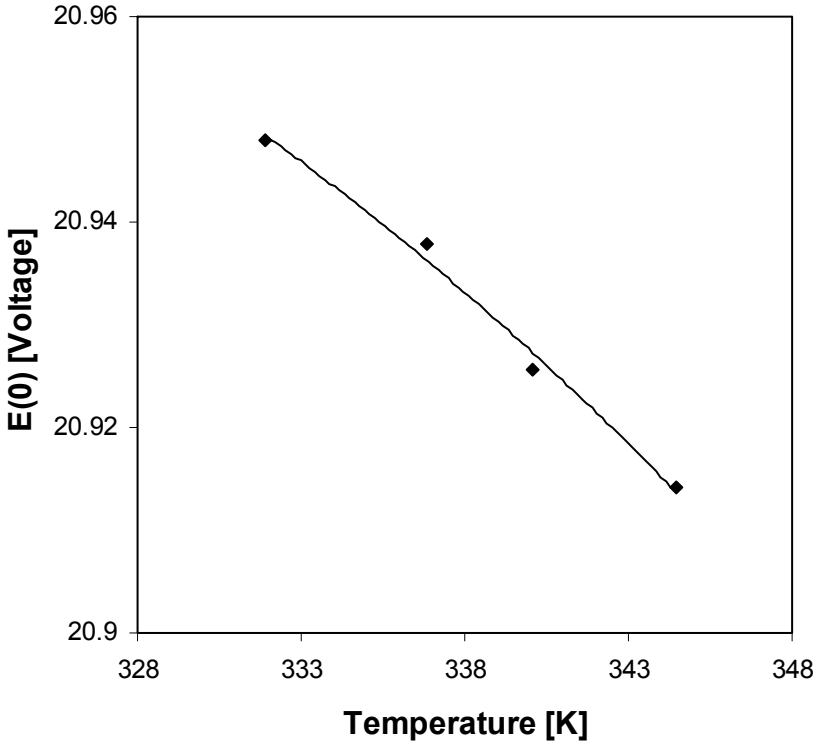

Figure 5.8 E(0)-temperature curve for the hot-wire velocity probe.

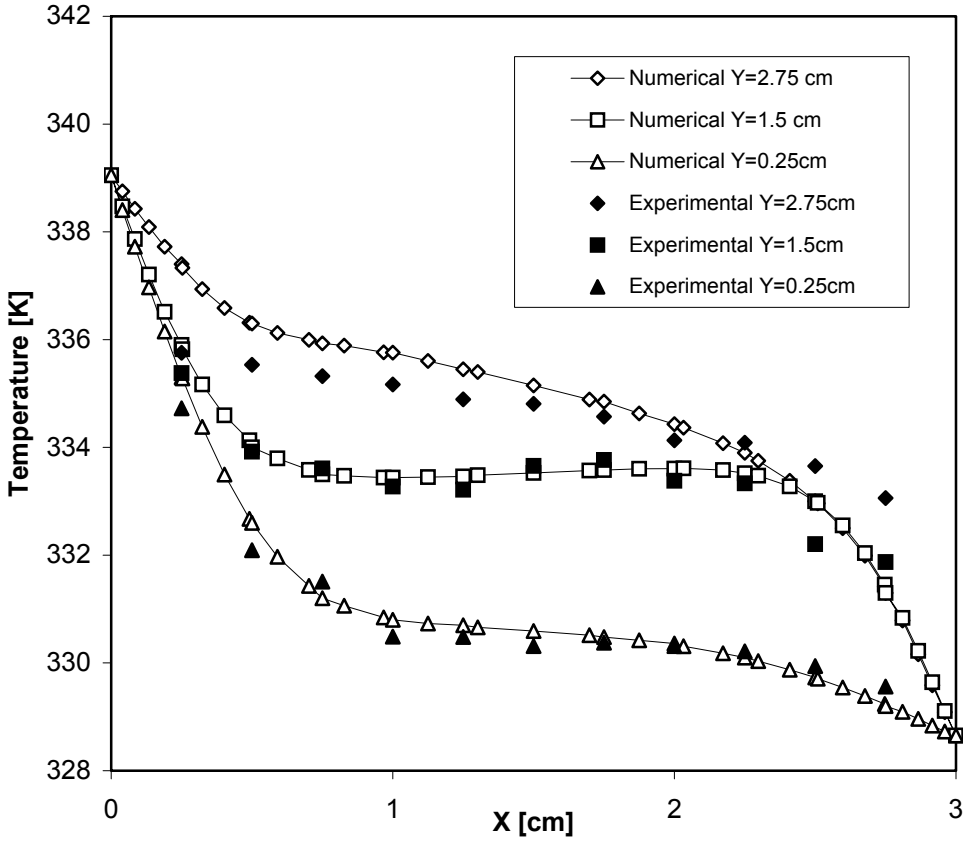

Figure 5.9 Comparison of the experimentally-measured and numerically-calculated temperature distributions across the cell at different vertical locations without externally applied magnetic field.

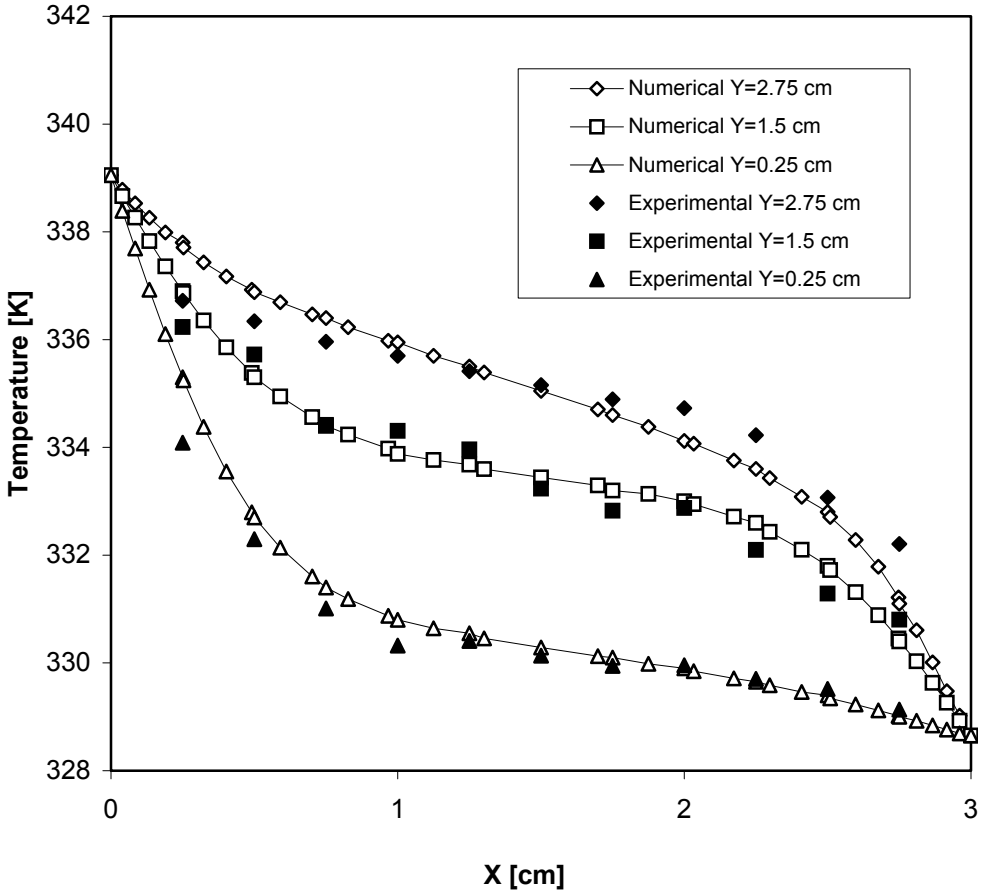

Figure 5.10 Comparison of the experimentally-measured and numerically-calculated temperature distributions across the cell at different vertical locations, subject to an externally applied magnetic field of 300 Gauss.

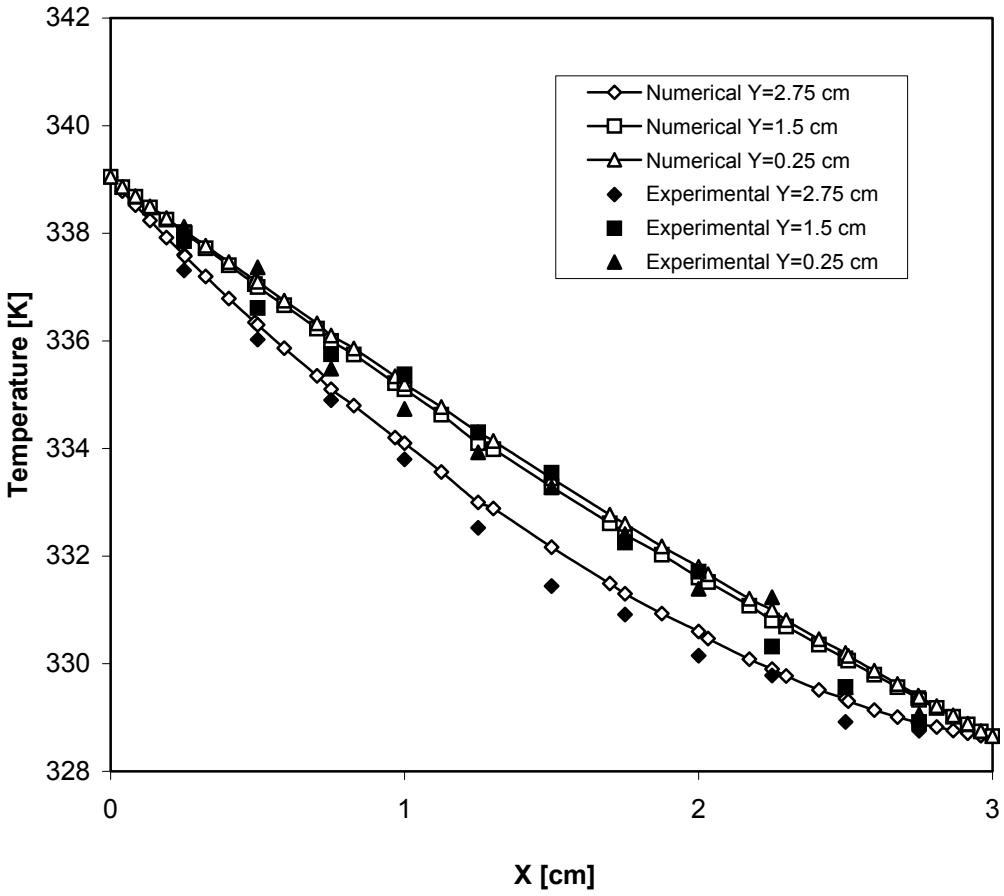

Figure 5.11 Comparison of the experimentally-measured and numerically-calculated temperature distributions across the cell at different vertical locations, subject to an externally applied magnetic field of 3500 Gauss.

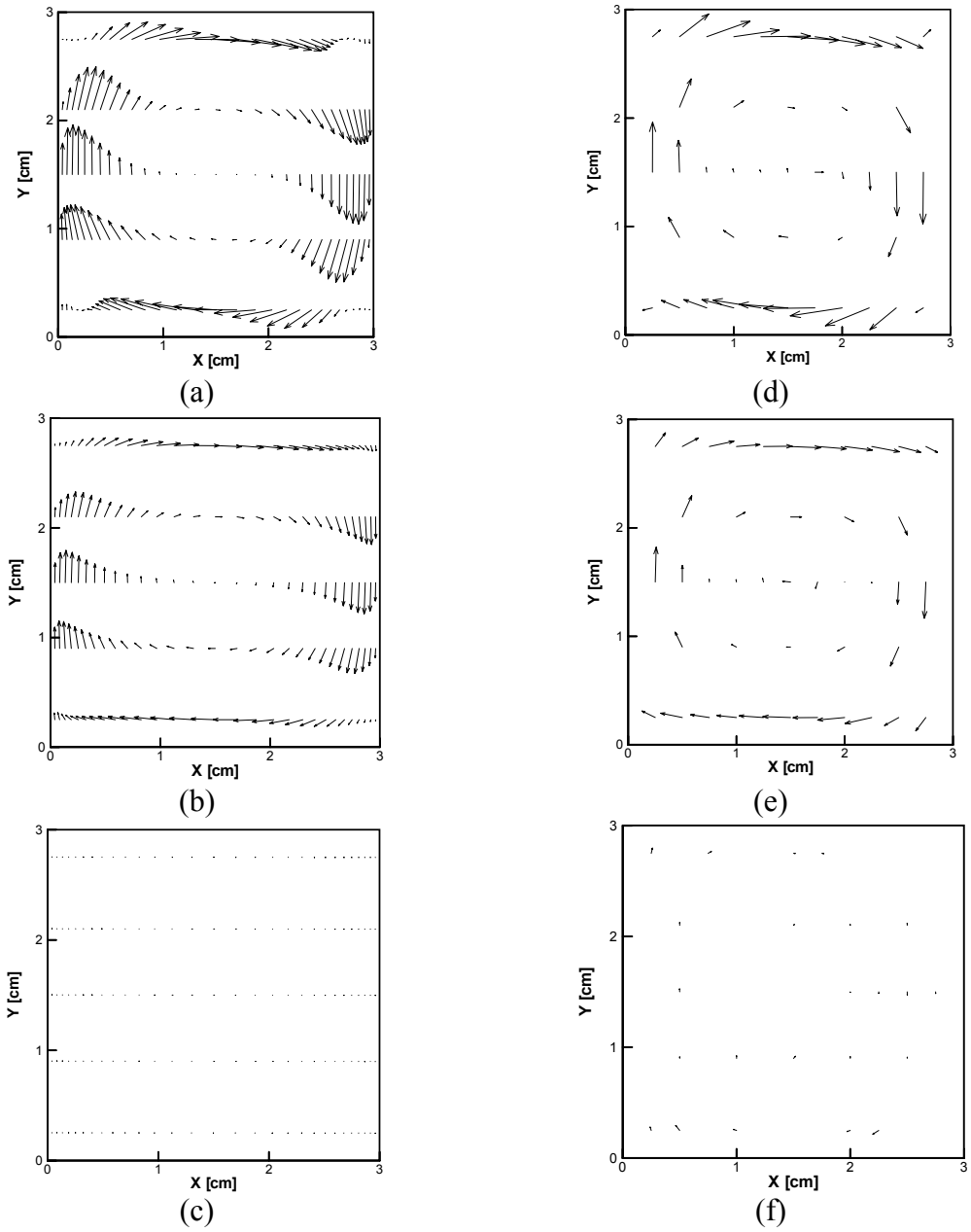

Figure 5.12 Comparison of computed and measured vector velocity distribution in the molten gallium for various field strengths: (a-c) Numerical results without magnetic field (a), with the field strength of 300 Gauss (b) and with the field strength of 35Gauss; and (d-f) measured velocity field without magnetic field (d), with the field strength of 300 Gauss and (c) with the field strength of 3500 Gauss.

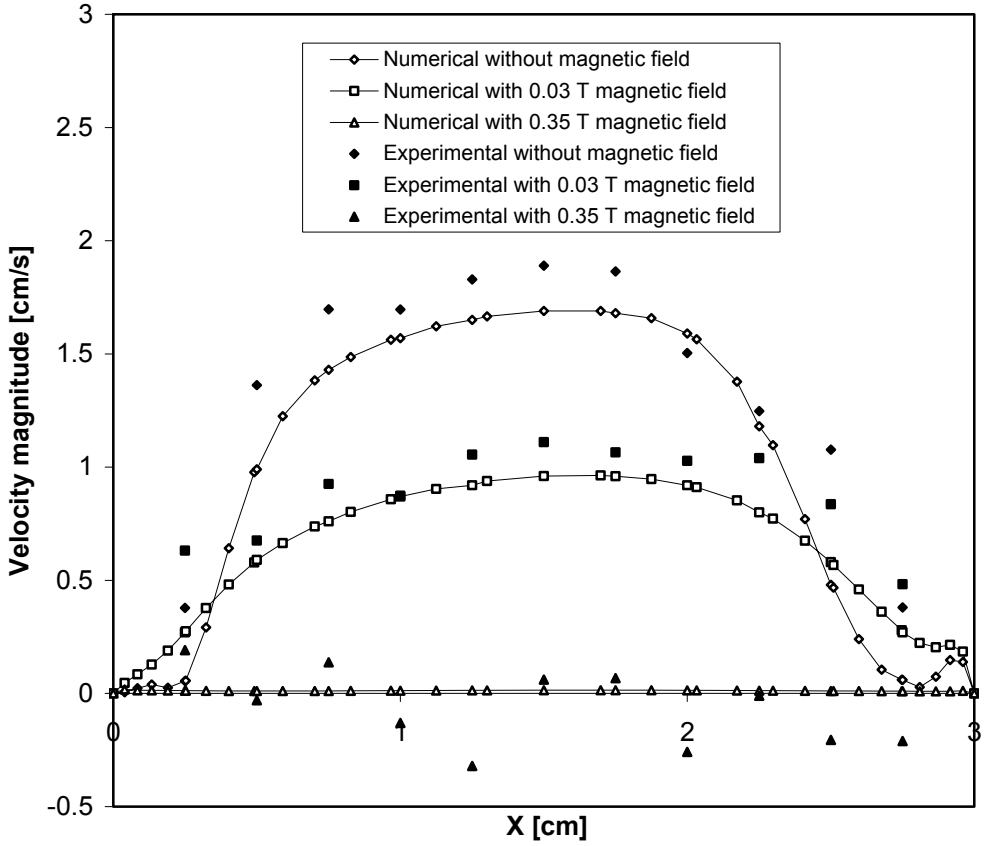

Figure 5.13 Dependence of velocity (in magnitude) distribution upon an applied magnetic field along Y = 2.75 cm.

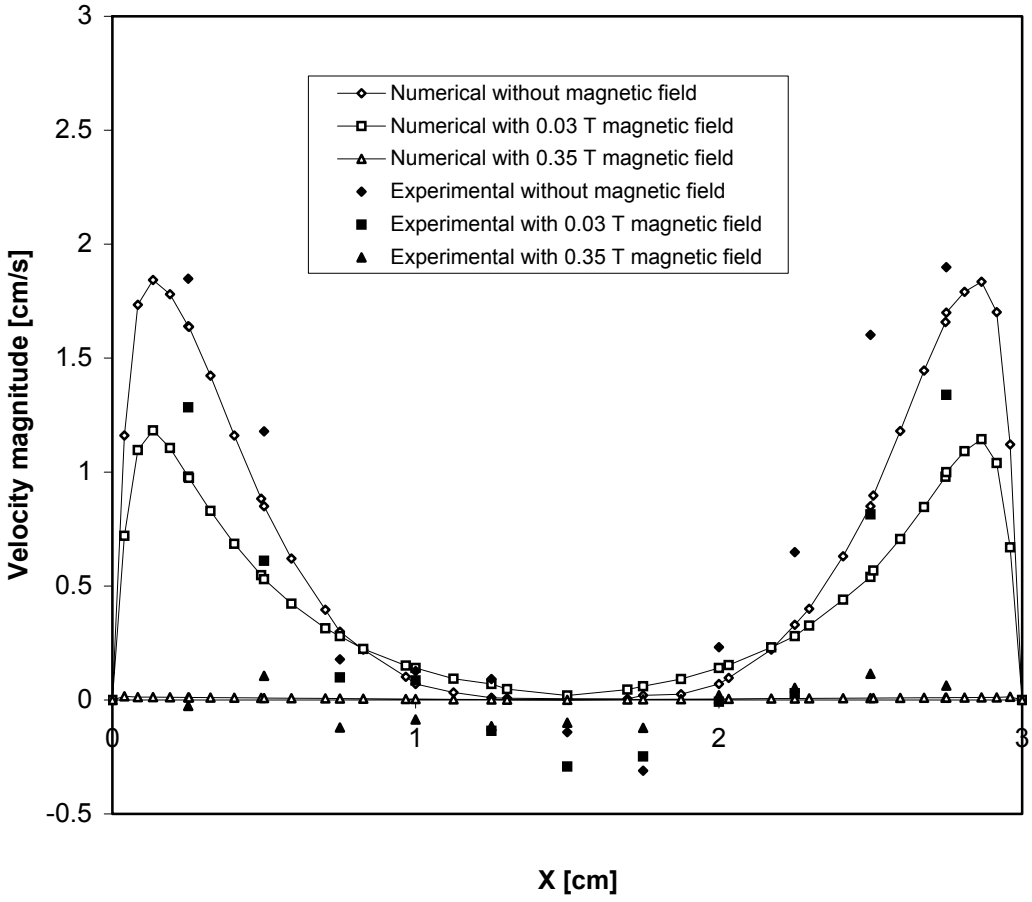

Figure 5.14 Dependence of velocity (in magnitude) distribution upon an applied magnetic field along Y = 0.5 cm.

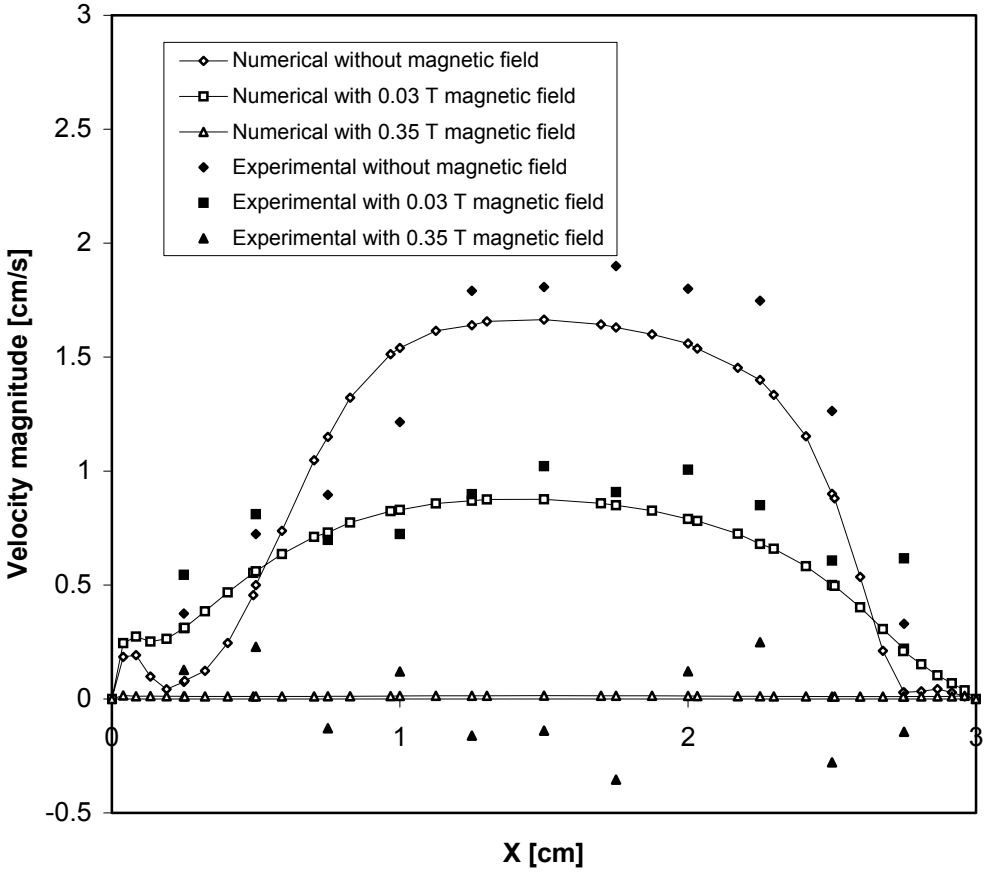

Figure 5.15 Dependence of velocity (in magnitude) distribution upon an applied magnetic field along Y = 0.25 cm.

CHAPTER SIX

CONCLUSIONS AND FUTURE WORK

6.1 Conclusions

The present study is focused on convective phenomena in the material processing systems. The major conclusions drawn from the present study are summarized in the following paragraphs.

A numerical model has been developed to describe the fluid flow and heat transfer process in the crucible. The temperature and velocity fields are solved using the high order finite difference method and the internal radiation problem is modeled using the discontinuous finite element method. The two numerical models are coupled through an iterative process. The integrated numerical model is used to simulate Marangoni-Rayleigh-Bénard flow of radiation participating melt in the Czochralski crucibles. Based on the numerical simulations, linear stability analysis of the convective flow is carried out at various geometric boundary conditions and radiative properties to determine the critical Grashof numbers at which the flow loses its axisymmetry. It is found that when the melt is transparent to the radiative energy transfer, the flow consists of a major convective loop and a small recirculation near the free surface caused by the Marangoni effect. The Marangoni effect does not have a strong effect on the bulk flow structure. Along the free surface, the Marangoni flow and the Bénard flow are both dragged from the vertical towards the center and therefore, the Marangoni flow plays a stabilizing role in the coupled Marangoni-Rayleigh-Bénard convection.

When the melt is radiation-participating, the computed temperature fields are changed significantly. Strong heat flux imposed at the system boundaries tends to decrease the melt temperature while the absorption, emission and scattering of the radiative energy traveling through the melt increase the melt temperature. In most of the cases, the effect of the boundary heat flux is strong enough to suppress that of the internal radiation. The stability analysis has shown that the fact that the melt is involved in the radiative energy transfer delays the occurrence of the three-dimensional convection. The most dangerous azimuthal mode is changed from 1 to 5 due to the internal radiation. This implies that the internal radiation has a significant effect on the formation of the spoke line along the free surface. It is found that the internal radiation does not change the velocity field significantly.

An experimental investigation of natural convection driven by a temperature gradient in molten metal contained in a rectangular enclosure with and without the presence of an external magnetic field is presented. Molten gallium was used as a working fluid. Both the temperature and velocity fields were measured. The temperature profile was determined using a thermocouple and the melt flow velocity was measured using a standard constant temperature hot-film anemometer. The measured velocity field exhibits a recirculating cell, which is consistent with numerical predictions obtained from a numerical model reported in an early study. The flow structure remains the same with and without an applied magnetic field. The magnitude of the velocity, however, is reduced with an increase in applied magnetic field strengths. The reduction in convection is also manifested in the measured thermal profiles, which approach to a linear distribution across the cell as the magnetic field increases in strength. The measured

velocity and temperature profiles are compared reasonably well with the numerical predictions.

6.2 Future work

To further extend the present study, the following recommendations are made for future investigations.

- Stability curves over a wider range of the material properties, such as Prandtl number, would be helpful in better understanding of the convective phenomena in the material processing systems;
- The nonlinear behavior of the Marangoni flow is important in the understanding of the formation of the surface flow pattern such as the well-known spoke line pattern. A nonlinear stability analysis can be used to obtain detailed information of transition in flow pattern and understand the instability mechanisms that cause the formation and transition of certain surface flow pattern;
- Based on the stability analysis result, three-dimensional numerical simulation of the convective flow in the Czochralski crucibles can be carried out. In order to fully capture the highly nonlinear Marangoni behavior along the free surface, extremely fine mesh and time-step are required, which impose overwhelming high computational load. A parallel algorithm is highly desirable to make the task possible;
- The present experiment measures the velocity profile using a single sensor hot-film probe, which provides only the information on velocity

magnitude. To fully understand the two-dimensional convection in the box, further measurements using multi-dimensional probe is desirable;

- Previous investigations have shown that the magnetic damping effect depends on the relative direction of the temperature gradient and the magnetic field. In the present study, only the case in which the temperature gradient is parallel to the magnetic field is measured. Measurements carried out on other relative directions would be an important complement to the present study.

BIBLIOGRAPHY

Adams, N.A. and Kleiser, L., 1996, Subharmonic transition to turbulence in a flat-plate boundary layer at Mach number 4.5, *J. Fluid Mech.*, vol. 317, pp. 301.

Ai, X., 2004, The instability analysis and direct numerical simulation of turbulent flows in electromagnetically levitated droplets, Ph.D. Thesis, Washington State University, Pullman, WA.

Alboussière, T., Garandet, J.P. and Moreau, R., 1993, Buoyancy-driven convection with a uniform magnetic field. Part 1. Asymptotic analysis, *J. Fluid Mech.*, vol. 253, pp. 545.

Alboussière, T., Garandet, J.P. and Moreau, R., 1996, Asymptotic analysis and symmetry in MHD convection, *Phys. Fluids*, vol. 8, pp. 2215.

Arnoldi, W.E., 1951, The principle of minimized iterations in the solution of the matrix eigenvalues problem, *Qua. Appl. Math.*, vol. 9, pp. 17.

Arpci, V.S. and Gözüm, D., 1973, Thermal stability of radiating fluids: the Bénard problem, *Phys. Fluids.*, vol. 16, pp. 581.

Arpci, V.S. and Bayazitoğlu, Y., 1973, Thermal stability of radiating fluids: asymmetric slot problem, *Phys. Fluids.*, vol. 16, pp. 589.

Aurnou, J.M. and Olson, P.L., 2001, Experiments on Rayleigh-Bénard convection magnetoconvection and rotating magnetoconvection in liquid gallium, *J. Fluid Mech.*, vol. 430, pp. 283.

Baumgartl, J. and Müller, G., 1996, The use of magnetic fields for damping the action of gravity fluctuations (g-jitter) during crystal growth under microgravity, *J. Cryst. Growth*, vol. 169, pp. 582.

Bénard, H., 1990, Les tourbillons cellulaires dans une nappe liquide, *Rev. Gén. Sci. Pures Appl.*, vol. 12, pp. 1261.

BenHadid, H. and Henry, D., 1996, Numerical simulation of convective three-dimensional flows in a horizontal cylinder under the action of a constant magnetic field, *J. Cryst. Growth*, vol. 166, pp. 436.

BenHadid, H. and Henry, D., 1997, Numerical study of convection in the horizontal Bridgman configuration under that action of a constant magnetic field. Part2. Three-dimensional flow, *J. Fluid Mech.*, vol. 333, pp. 57.

Block, M.J., 1956, Surface tension at the cause of Bénard cells and surface deformation in a liquid film, *Nature*, vol. 178, pp. 650.

Brito, D., Nataf, H.-C., Cardin, P., Aubert, J. and Masson, J.-P., 2001, Ultrasonic Doppler velocimetry in liquid gallium, *Exp. Fluids*, vol. 31, pp. 653.

Brandon, S., and Derby, J.J., 1992, Heat transfer in vertical Bridgman growth of oxides: effects of conduction, convection, and internal radiation, *J. Cryst. Growth*, vol. 121, pp. 473.

Bruun, H.H., 1995, Hot-film Anemometry: Principles and Signal Analysis, Oxford University Press, Oxford.

Buell, J.C. and Catton, I., 1983, The effect of wall conduction on the stability of a fluid in a right circular cylinder heated from below, *ASME J. Heat Transfer*, vol. 105, pp. 255.

Chandrasekhar, S., 1961, Hydrodynamic and hydromagnetic stability, The Claredon Press, Oxford.

Chang, L.C., Yang, K.T. and Lloyd, J.R., 1983, Radiation-natural convection interaction in two-dimensional complex enclosures, *ASME J. Heat Transfer*, vol. 105, pp. 89.

Charlson, G.S. and Sani, R.N., 1970a, Thermoconvective instability in a bounded cylindrical fluid layer, *Int. J. Heat Mass Transfer*, vol. 13, pp. 1479.

Charlson, G.S. and Sani, R.N., 1970b, On Thermoconvective instability in a bounded cylindrical fluid layer, *Int. J. Heat Mass Transfer*, vol. 14, pp. 2157.

Christie, I., 1985, Upwind compact finite difference schemes, *J. Comput. Phys.*, vol. 59, pp. 353.

Cockburn B., Karniadakis G., and Shu, C.W., 2000, The development of discontinuous Galerkin methods. In: Cockburn B, Karniadakis G, Shu CW, editor. Discontinuous Galerkin Methods: Theory, Computation and Applications. Lecture Notes in Computational Science and Engineering, 11. New York: Springer Verlag.

Cockburn B., 2001, Devising discontinuous Galerkin methods for non-linear hyperbolic conservation laws., *J. Comput. Appl. Math.*, vol. 128, pp. 187.

Coriell, S.R. and Sekerka, R.F., 1981, Effect of convective flow on morphological stability, *PhysicoChem. Hydridyn.*, vol. 2, pp. 281.

Cui, X. and Li, B.Q., 2004, A discontinuous finite-element formulation for internal radiation problems, *Num. Heat Transfer, Part B*, vol. 46, pp. 223.

Cui, X. and Li, B.Q., 2005, A discontinuous finite-element formulation for radiative transfer in axisymmetric finite cylindrical enclosures and coupling with mode heat transfer, *Num. Heat Transfer, Part B*, vol. 48, pp. 317.

Dauby, P.C., Lebon, G. and Bouhy, E., 1997, Linear Bénard-Marangoni instability in rigid circular containers, *Phys. Review E*, vol. 56(1), pp. 520.

Davis, S.H., 1987, Thermocapillary instabilities, *Ann. Rev. Fluid Mech.*, vol. 19, pp. 403-435.

Davoust, L., Cowley, M.D., Moreau, R. and Bolcato, R., 1999, Buoyancy-driven convection with a uniform magnetic field. Part 2. Experimental investigation, *J. Fluid Mech.*, vol. 400, pp. 59.

Desreyaud, G. and Lauriat, G., 1985, Natural convection of radiating fluid in a vertical layer, *ASME J. Heat Transfer*, vol. 107, pp. 710.

Ding, Y. and Kawahara, 1998, Linear stability of incompressible fluid flow using a mixed finite element method, *J. Computational Phys.*, vol. 139, pp. 243.

Drazin, R.G. and Reid, W.H., 1981, Hydrodynamic stability, The Cambridge University Press.

Eckert, S. and Gerbeth, G., 2002, Velocity measurements in liquid sodium by means of Ultrasound Doppler Velocimetry, *Exp. Fluids*, vol. 32(5), pp. 542.

Eckert, S., Witke, W. and Gerbeth, G., 2000, A new mechano-optical technique to measure local velocities in opaque fluids, *Flow Meas. and Instrum.*, vol. 11, pp. 71.

Ezersky, A.B., Garcimartín, A., Burguete, J., Mancini, H.L., and Pérez-García, 1993, Hydrothermal waves in Marangoni convection in a cylindrical container, *Phys. Rev.*, vol. 47, pp.1126.

Favre, E., Blumendeld, L. and Daviaud, F., 1997, Instabilities of a liquid layer locally heated on its free surface, *Phys. Fluids*, vol. 9(5), pp. 1473.

Fleming, M.C., 1974, Solidification processing. McGraw-Hill Inc.

Galazka, Z., Schwabe, D. and Wilke H., 2003, Influence of internal radiation on the heat transfer during growth of YAG single crystals by the Czochralski method, *Crystal Research Technology*, vol. 38, pp. 859.

Garandet, J.P., Alboussière, T. and Moreau, R., 1992, Buoyancy-driven convection in a rectangular enclosure with a transverse magnetic field, *Int. J. Heat Mass Transfer*, vol. 35, pp. 741.

Gardner, R.A. and Lykoudis, P.S., 1971, Magneto-fluid-mechanic pipe flow in a transverse magnetic field, *J. Fluid Mech.*, vol. 47(4), pp. 737.

Garnier, N. and Chiffaudel, A., 2001, Two dimensional hydrothermal waves in an extended cylindrical vessel, *Eur. Phys. J. B.*, vol. 19, pp. 87.

Gershuni, G.Z. and Zhukhovitskii, E.M., 1976, Convective stability of incompressible fluids, Keter Publishing House Jerusalem Ltd.

Glicksman, M.E., Coriell, S.R. and McFadden, G.B., 1986, Interaction of flows with the crystal-melt interface, *Ann. Rev. Fluid Mech.*, vol. 18, pp. 307.

Hamacher, J. and Merbold, 1987, Analysis of microgravity measurements performed during D1, *Proc. 6th European Symp. On Materials Sciences under Microgravity Conditions,* Bordeaux, France, ESA SP-255, pp. 413.

Hof, B., Juel, A. and Mullin, T., 2003, Magnetohydrodynamic damping of convective flows in molten gallium, *J. Fluid Mech.*, vol. 482, pp. 163.

Hoyas, S., Herrero, H. and Mancho, A.M., 2002, Thermal convection in a cylindrical annulus heated laterally, *J. Phys. A: Math. Gen.*, vol. 35, pp. 4067.

Hunt, J.C.R and Shercliff, J.A., 1971, Magnetohydrodynamics at high Hartmann number, *Ann. Rev. Fluid Mech.*, vol. 3, pp. 37.

Hurle, D.T.J., 1966, Temperature oscillations in molten metals and their relationship to growth striae in melt-grown crystals, *Phil. Mag.*, vol. 13, pp. 305.

Hurle, D.T.J., Jakeman, E. and Johnson, C.P., 1974, Convective temperature oscillation in molten gallium, *J. Fluid Mech.*, vol. 64, pp. 565.

Jing, C.J., Imaishi, N., Yasuhiro, S. and Miyazawa, Y., 1999, Three-dimensional numerical simulation of spoke pattern in oxide melt, *J. Cryst. Growth*, vol. 200, pp. 204.

Juel, A., Mullin, T., BenHadid, H. and Henry, D., 1999, Magnetohydrodynamic convection in molten gallium, *J. Fluid Mech.*, vol. 378, pp. 97.

Kapulla, R., Sigg, B., Horanyi, S. and Hudina, M., 2000, Local velocity measurements in a thermally-stratified sodium mixing layer using a permanent-magnet probe, *Exp. Thermal Fluid Sci.*, vol. 20, pp. 115.

Kassemi, M. and Naraghi, M.H.N., 1993, Analysis of radiation-natural convection interactions in 1-g and low-g environments using the discrete exchange factor method, *Int. J. Heat Mass Transfer*, vol. 36(17), pp. 4141.

Kim, J. and Moin, P., 1985, Application of a fractional-step method to incompressible Navier-Stokes equations, *J. Comput. Phys.*, vol. 59, pp. 308.

Kobayashi, M., Tsukada, T. and Hozawa, M., 1997, Effect of internal radiative heat transfer on the convection in CZ oxide melt, *J. Cryst. Growth*, vol. 180, pp. 157.

Koschmieder, E.L. and Pallas, S.G., 1974, Heat transfer through a shallow, horizontal convecting fluid layer, *Int. J. Heat Mass Transfer*, vol. 17, pp. 991.

Koschmieder, E.L, 1993, Bénard cells and Taylor vortices, Cambridge University Press.

Koster, J.N., Seidel, T. and Derebail, R., 1997, A radioscopic technique to study convective fluid dynamics in opaque liquid metals, *J. Fluid Mech.*, vol. 343, pp. 29.

Lan, C.W., 2004, Recent progress of crystal growth modeling and growth control, *Chem. Engr. Sci.*, vol. 59, pp. 1437.

Langlois, M.E., 1986, Interaction of flows with the crystal-melt interface, *Ann. Rev.. Fluid Mech.*, vol. 18, pp. 307.

Larson, D.W., 1981, Enclosed radiation and turbulent natural convection induced by a fire, *Numerical Method in Heat transfer* (Edited by Lewis, R.W., Morgan, K. and Zienkiewicz, O.C.), Wiley, New York.

Li, B.Q., 2006, Discontinuous Finite Elements in Fluid Dynamics and Heat Transfer, Springer.

Le, H. and Moin, P., 1991, An improvement of fractional step methods for the incompressible Navier-Stokes equations, *Int. J. Numer. Meth. Fluids*, vol. 92, pp. 369.

Lele, S.K., 1992, Compact finite difference schemes with spectral-like resolution, *J. Comput. Phys.*, vol. 103, pp. 16.

Levich, H.G. and Krylov, V.S., 1969, Surface tension-driven phenomena, *Ann. Rev. Fluid Mech.*, vol. 1, pp. 293.

Lomas, C.G., 1986, Fundamentals of Hot Wire Anemometry, Cambridge University Press, Cambridge, UK.

Ma, N. and Walker, J.S., 1996, Magnetic damping of buoyant convection during semiconductor crystal growth in microgravity. continuous random g-jitters, *Phys. Fluids*, vol. 8 (4), pp. 944.

Malcolm, D.G., 1969, Some aspects of turbulence measurement in liquid mercury using cylindrical quartz-insulated hot-film sensors, *J. Fluid Mech.*, vol. 37, pp. 701.

Modest, M.F., 1993, Radiative heat transfer, McGraw-Hill, Inc., New York.

Moreau, R., 1990, Magnetohydrodynamics, Kluwer.

Nelson, E.S., 1994, Examination of anticipated g-Jitter on space station and its effects on materials processes. *NASA TM*, 103775, pp. 1.

Neumann, G., 1990, Three-dimensional numerical simulation of buoyancy-driven convection in vertical cylinders heated from below, *J. Fluid Mech.*, vol. 214, pp. 559.

Oden, J.T., Babuka, I. and Baumann, C., 1998, A discontinuous HP finite element method for diffusion problems, *J. Comput. Phys.*, vol. 146, pp. 491.

Okada, K. and Ozoe, H., 1992, Experimental heat transfer rate of natural convection of molten gallium suppressed under an external magnetic field in either X, Y, or Z direction, *J. Heat Transfer*, vol. 114, pp. 107.

Ozoe, H. and Okada, H., 1989, The effect of the direction of the external magnetic field on the three-dimensional natural convection in a cubic enclosure, *Int. J. Heat Mass Transfer*, vol. 32, pp. 1939.

Pan, B., Shang, D.-Y., Li, B.Q. and de Groh, H.C., 2002, Magnetic field effects on g-jitter induced flow and solute transport, *Int. J. Heat Mass Transfer*., vol. 45, pp. 125.

Pearson, J.R.A., 1958, On convection cells induced by surface tension, *J. Fluid Mech.*, vol. 4, pp. 489.

Peltier, L.J., and Biringen, S., 1993, Time-dependent thermocapillary convection in a rectangular cavity: numerical results for a moderate Prandtl number fluid, *J. Fluid Mech.*, vol. 257, pp. 339.

Pimputkar, S.M. and Ostrach, S., 1981, Convective effects in crystal growth from melt, *J. Cryst. Growth*, vol. 55, pp. 614.

Prasad, S.R., Mallika, C., Anderson, T.J. and Narayanan, R., 1994, An electrochemical method to detect flow profiles during convection in liquid metals, *J. Cryst. Growth*, vol. 198/199, pp. 194.

Priede, J. and Gerbeth, G., 1999, Oscillatory and rotational instabilities in electromagnetic levitation, in *Fluid Flow Phenomena in Metals Processing*, Ed. El-Kaddah, N., Robertson, D.G.C., Johansen, S.T. and Voller, V.R., TMS, San Diego, California.

Pruett, C.D. and Zang, T.A., 1992, Direct numerical simulation of laminar breakdown in high-speed axisymmetric boundary layers, *Theor. Comput. Fluid Dynam.*, vol. 3, pp. 345.

Rai, M.M. and Moin, P., 1993, Direct numerical simulation of transition and turbulence in a spatially evolving boundary layer, *J. Comput. Phys.*, vol. 109, pp. 169.

Rayleigh, L., 1916, On convection currents in a horizontal layer of fluid, when the higher temperature is on the under side, *Philos. Mag.*, vol. 32, pp. 529.

Reed, W.H. and Hill, T.R., 1973, Triangular mesh methods for neutron transport equation, Tech. Pep. LA-UR-73-479, Los Alamos Scientific Laboratory, Los Alamos, MN.

Ricou R. and Vives, C., 1982, Local velocity and mass transfer measurements in molten metals using an incorporated magnet probe, *Int. J. Heat Mass Transfer*, vol. 25, pp. 1579.

Rist, U. and Fasel, H., 1995, Direct numerical simulation of controlled transient in flat-plate boundary layer, *J. Fluid Mech.*, vol. 298, pp. 211.

Robinson, T. and Larsson, K., 1993, An experimental investigation of a magnetically driven rotating liquid-metal flow, *J. Fluid Mech.*, vol. 60(4), pp. 641.

Rosenblat, S., 1982, Thermal convection in a vertical cylinder, *J. Fluid Mech.*, vol. 122, pp. 395.

Rubinov, A., Erenburg, V., Gelfgat, A.Yu., Kit, E., Bar-Yoseph, P.Z. and Sloan, A., 2004, Three-dimensional instabilities of natural convection flow in a vertical cylinder with partially heated sidewall, *ASME J. Heat Transfer*, vol. 126, pp.586.

Sab, V., Kuhlmann, H.C. and Rath, H.J., 1996, Investigation of three-dimensional thermocapillary convection in a cubic container by multi-grid method, *Int. J. Heat Mass Transfer*, vol. 39, pp. 603.

Sabau, A.S. and Raad, P.E., 1999, Oscillations in high-order finite difference solutions of stiff problems on non-uniform grids, *Int. J. Numer. Methods Fluids*, vol. 30, pp. 939.

Saad, Y., 1980, Variation on Arnoldi's method for computing eigenelements of large unsymmetric matrices, *Linear Alge. Appl.*, vol, 34, pp. 269.

Sajben, M., 1965, Hot wire anemometer in liquid mercury, *Review Sci. Intru.*, vol. 36, pp. 945.

Schatz, M.F. and Neitzel, G.P., 2001, Experiments on thermocapillary instabilities, *Annu. Rev. Fluid Mech.*, vol. 33, pp. 93.

Schwabe, D., 1988, Surface-tension-driven flow in crystal growth melts, *Crystals* (Springer-Verlag, Berlin), Vol. 11, pp. 75.

Schwabe, D., Möller, U., Schneider, J. and Scharmann, A., 1992, Instabilities of shallow dynamic thermocapillary liquid layer, *Phys. Fluids*, A vol. 4, pp.2368.

Series, R.W. and Hurle, D.T.J., 1991, The use of magnetic fields in semiconductor crystal-growth, *J. Cryst. Growth*, vol. 113, pp. 305.

Shatrov, V., Galindo, V. and Gerbeth, G., 2001, Stability analysis of the flow inside an electromagnetically levitated drop, *Magnetohydrodynamics*, vol. 37, pp. 45.

Shu, Y., Li, B.Q. and de Groh, H.C. III, 2002, Magnetic damping of g-jitter induced double-diffusion convection, *Num. Heat Transfer, Part A*, vol. 42, pp. 345.

Shu, Y., Li, B.Q. and Lynn, K.G., 2004, Numerical modeling of internal radiation and solidification in semitransparent melts in magnetic field, *Num. Heat Transfer, Part A*, vol. 45, pp. 957.

Siegel, R. and Howell, J.R., 1992, Thermal radiation heat transfer, 3rd Edition, Taylor & Francis.

Stork, K. and Müller, U., 1975, Convection in boxes: an experimental investigation in vertical cylinder and annuli, *J. Fluid Mech.*, vol. 71, pp. 231.

Tan, Z. and Howell, J.R., 1991, Combined radiation and natural convection in a two-dimensional participating square medium, *Int. J. Heat Mass Transfer*, vol. 34(3), pp. 785.

Tiller, W.A., 1991, The science of crystallization: macroscopic phenomena and defect generation, Cambridge University Press.

Touihri, R., BenHadid, H. and Henry, D., 1999, On the onset of convective instabilities in cylindrical cavities heated from below. I. pure thermal case, *Phys. Fluids*, vol. 11, pp. 2078.

Trakas, C., Tabeling, P. and Chabrerie, J.P., 1983, Low-velocity calibration of hot-film sensors in mercury, *J. Phys. E: Sci. Intrum.*, vol. 16, pp. 568.

Tsukada, T., Katsuyuki, K. and Hozawa, M., 1995, Effect of internal radiation within crystal and melt on Czochralski crystal growth of oxide, *Int. J. Heat Mass Transfer*, vol. 38(15), pp. 2707.

Vrentas, J.S., Narayanan, R. and Agrawal, S.S., 1981, Free surface convection in bounded cylindrical geometry, *Int. J. Heat Mass Transfer*, vol. 24(9), pp. 1513.

Wagner, C., Friedrich, R. and Narayanan, R., 1994, Comments on the numerical investigation of Rayleigh and Marangoni convection in a vertical circular cylinder, *Phys. Fluids*, vol. 6(4), pp.1425.

Wanschura, M., Kuhlmann, H.C. and Rath, H.J., 1996, Three-dimensional instability of axisymmetric buoyant convection in cylinder heated from below, *J. Fluid Mech.*, vol. 326, pp. 339.

Webb, B.W. and Viskanta, R., 1987, Radiation-induced buoyancy-driven flow in rectangular enclosures: experiments and analysis, *ASME J. Heat Transfer*, vol. 109, pp. 427.

Xu, J. and Zebib, A., 1998, Oscillatory two- and three-dimensional thermocapillary convection, *J. Fluid Mech.*, vol. 364, pp. 187.

Yang, K.T., 1986, Numerical modeling of natural convection-radiation interactions in enclosures, *Heat Transfer 1986: Proc. Eighth Int. Heat Transfer Conf.*, vol. 1 pp. 131-140, Hemisphere, Washington, DC.

Zhong, X., 1998, High-order finite-difference schemes for numerical simulation of hypersonic boundary layer transitions, *J. Comput. Phys.*, vol. 144, pp. 662.